Microwave and Millimeter-Wave Plasma Formation Within 2D Photonic Crystal Defects

A dissertation submitted by

Stephen Parsons

in partial fulfillment of the requirements for the degree of

Doctor of Philosophy

in

Electrical Engineering

Tufts University

August 20, 2017

Advisor: Jeffrey Hopwood

Abstract

Photonic crystals with integrated plasma elements have received increased attention in recent years due to the variable nature of their dielectric properties. To date, all such devices have included plasma elements that have been controlled using external power sources, most commonly, DC discharge tubes. Recent modeling work by Gregório et al. suggest that an electromagnetic wave incident on a photonic crystal with a central point-defect vacancy enables self-initiated gas breakdown. The vacancy left by the point-defect creates a high-Q resonant cavity which enhances the electric field within the cavity to the point of gas breakdown. Once breakdown occurs, the plasma is also maintained within the vacancy by the incoming wave. In this thesis, I will explore the environmental variables (gas pressure, input power) that allow for a plasma to be formed and sustained, and the effect the plasma has on the incoming and outgoing electromagnetic wave. Design parameters and experimental results of two photonic crystal devices are included, one in the microwave frequency regime (~8.5 GHz) and one in the millimeter-wave regime (~43 GHz). I demonstrate that self-initiation of a plasma within the central vacancy is possible in 10 Torr of argon with as little as 1.4 W for the microwave device and 40 Torr of argon and 1.5 Watts for the millimeter-wave device. Once formed, the plasma filled cavity alters the transmission properties of the photonic crystal device, reducing transmission by up to 30 dB depending on gas pressure and power. Time domain measurements of plasma formation within the microwave

device reveal formation times 100 *ns* at 5 Torr and 9W and up to 3.5 μs at 50 Torr and 4 W. Plasma formation time for the millimeter-wave device is as low as 180 *ns* at 400 Torr and as high as 800 *ns* at 45 Torr. Using transmission of energy through the photonic crystal as a diagnostic tool, electron densities of 10^{16} to 10^{17} m^{-3} are measured for the microwave device and 10^{18} to 10^{20} m^{-3} for the millimeter-wave device.

Table of Contents

List of Tables

List of Figures

Microwave and Millimeter-Wave

Plasma Formation Within 2D

Photonic Crystal Defects

1   Introduction

Photonic crystals (PhC's) are periodic macroscopic crystalline structures consisting of materials with different dielectric constants. Their defining feature is that they have the ability to control electromagnetic waves. The repeated pattern of elements, or lattice, determines the propagation properties of the crystal. In essence, refraction and reflection of light from interfaces within the crystal serve to either block or allow propagation of the light in a single, or multiple directions. The dimensions of the crystal determine at which frequencies the light control is enabled. The combination of frequencies and propagation directions that are not allowed is called the **photonic band gap**. If the dielectric materials are sufficiently low loss and the dielectric constants are sufficiently different, the propagation for a set of frequencies is blocked for all directions, this results in a **complete band gap** for those frequencies.

Typically, photonic crystals are static devices, once constructed, their photonic properties do not change. However, there is interest in controlling, modulating, or tuning the properties of the photonic crystal post manufacture. Current methods of tunability include mechanical [1], thermal [2], and opto-fluidics [3]. Another method to achieve this reconfigurability is by inserting a plasma element within the crystal lattice, either by replacing a lattice element or by filling a defect position within the lattice. To date, plasmas within the crystal lattice have been produced using external power sources, such as using a DC voltage applied to a gas-filled discharge tube [4, 5, 6, 7]. Also, photonic crystal-like behavior has been observed by arrays of microplasmas [8, 9, 10]. The response of the photonic

2

crystal to an oncoming electromagnetic wave is altered by turning on and off plasma elements within the lattice, or by adjusting the voltage or current applied to the discharge, which modifies the electron density and thus the permittivity of the plasma. Recently, modeling suggests that a photonic crystal with a single point defect can self-initiate and self-sustain a plasma within the cavity created by the defect in direct response to the incoming EM wave, with no other external sources [11]. This would have the advantage of being a passive device, only responding and becoming active in response to external stimuli.

In this work, I explore, using 3-D EM simulation tools, the design characteristics of a photonic crystal resonator at 8.5 GHz and 43 GHz. I also investigate, experimentally, the environmental variables that effect gas breakdown, such as microwave/millimeter-wave input power and gas pressure and the effect the plasma has on transmission of energy through the device. Using device transmission, I also estimate the electron density of the resulting plasma element. Finally, I measure the time response of gas breakdown for various environmental conditions.

2 Photonic Crystal Background and Theory

Dielectric materials for the control of light have been studied since 1887 when Lord Rayleigh first described a multilayer dielectric mirror [12]. This mirror consisted of periodic layers of dielectric material with alternating dielectric constants. When light of the appropriate frequency was incident upon it, the multiple reflections from the various interfaces would destructively interfere and the forward propagating wave would be eliminated leaving only a reflected reverse propagating wave. The concept of an electromagnetic bandgap (EBG) emerged from two seminal papers from Eli Yablonovitch [13] and Sajeev John [14] in 1987. The motivation behind these papers was to control spontaneous emission in semiconductor materials and for the localization and control of light. Since these two papers were published, the study of photonic crystal devices and applications has grown rapidly.

There are three main categories of photonic crystals, which are based on the number of dimensions that have periodicity: one, two, and three-dimensional photonic crystals. Shown in Figure 1 is a depiction of periodicity of photonic crystals with differing colors representing materials with different permittivity (dielectric constant, ε_r). The periodic spacing between the differing materials is called the **lattice constant**, a, and can vary across the dimensions.

Construction methods and applications vary among the three types, but all have the common property of preventing electromagnetic radiation from propagating in up to one, two, or three directions depending on the dimensionality

of the crystal. The frequency of the bandgap scales linearly with the lattice constant (distance between periodic elements), leading to fabrication difficulties at higher and higher frequencies. For instance, at microwave frequencies, lattice constants are on the order of 1 cm, where at optical frequencies, lattice constants are on the order of 1 micron or less [15].
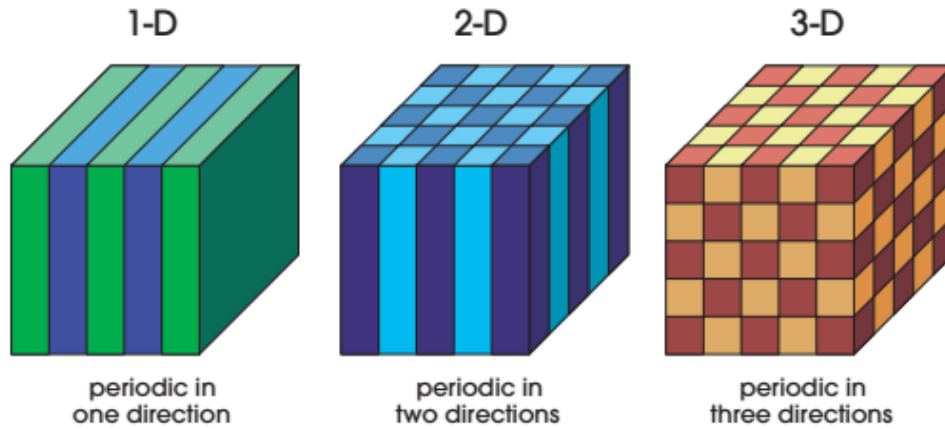
Figure 1 Depiction of one, two, and three-dimensional photonic crystals. Different colors represent materials with differing permittivity [12].

2.1 Photonic Crystal Categories

2.1.1 One Dimensional Photonic Crystals

One dimensional photonic crystals are the simplest form of PhC devices and also the first to be developed. They are characterized by a periodic structure in one dimension and are homogeneous in the other dimensions. Construction of a one-dimensional PhC is accomplished by alternating high and low permittivity dielectrics along a single dimension with spacing according to the lattice constant, *a*. An example of a one-dimensional PhC is shown in Figure 2.

The example shown in Figure 2 is also known as a Multilayer Film, and was first studied in 1887 by Lord Rayleigh. The traditional method of analyzing this structure, as first explained by Lord Rayleigh, is to imagine a propagating plane wave in the material. At each dielectric interface, transmissions and reflections would occur due to the mismatch in dielectric constants. These transmission and reflections would sum constructively and deconstructivity, and at frequencies within the bandgap, would sum to perfect reflection. However, complete reflection only occurs for on-axis wave propagation. When considering all propagation directions, no complete bandgap exists. While this method is intuitive for a one-dimensional structure, it does not lend itself easily to higher dimensions. An analysis using band structures will be shown in section 2.2 that can be generalized for one, two and three-dimensional PhC's.
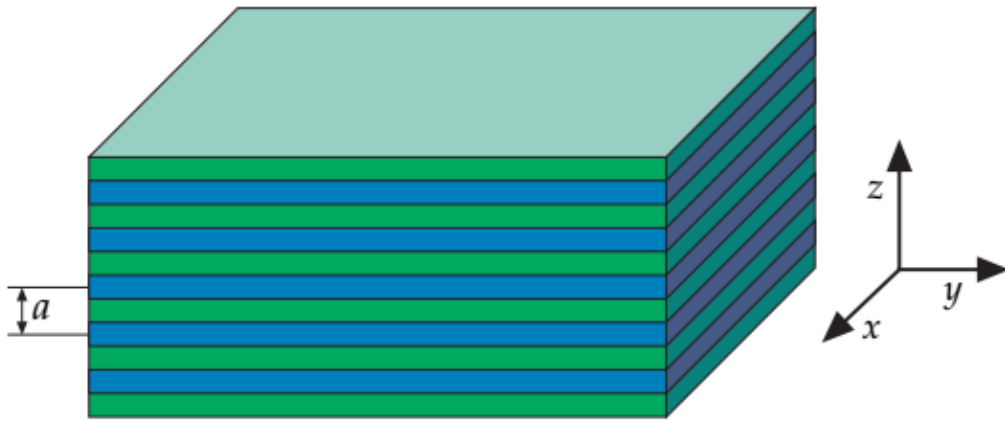
Figure 2 One dimensional photonic crystal consisting of alternating layers of two separate dielectric material [12].

2.1.2   Two Dimensional Photonic Crystals

Two dimensional PhC's are characterized by periodicity in two dimensions and are homogeneous in the third. Unlike the multilayer film shown in Figure 2, two-dimensional photonic crystals allow complete bandgaps for propagation directions within the plane of periodicity. An example of a two-dimensional square lattice of dielectric rods in air is seen in Figure 3. For an ideal PhC, the dielectric rod length would extend infinitely in the **z** direction and the pattern would extend infinitely in the **x** and **y** directions, but this is not realizable in practice. While the example shown in Figure 3 is common, other configurations are also possible, such as diamond pattern lattice and air holes in a dielectric slab.
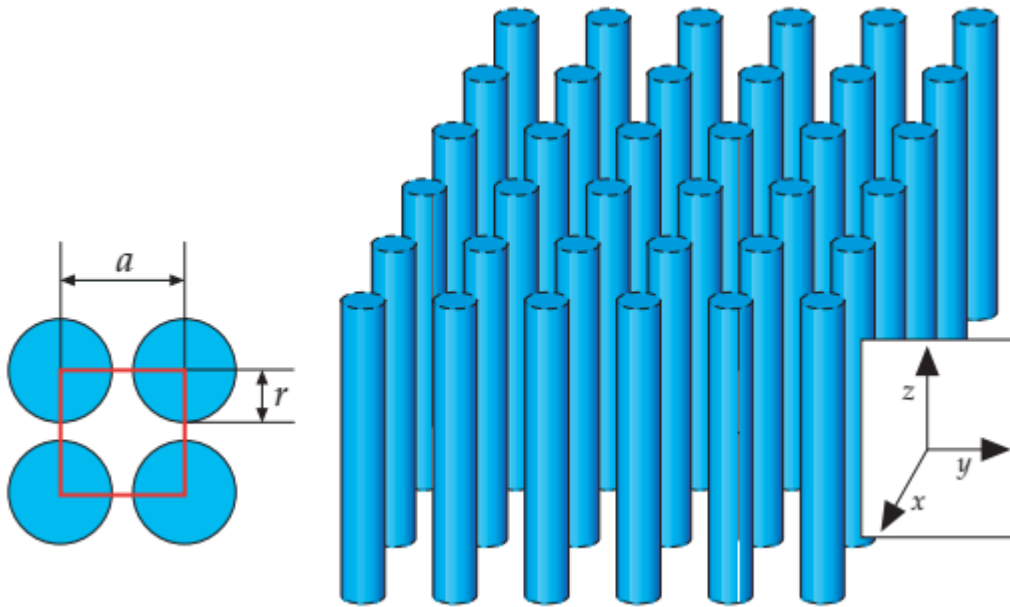
*Figure 3 Two-dimensional PhC structure with dielectric rods in air. Rods have a radius of **r**, and are spaced on center by the lattice constant **a** [12].*

The construction of two dimensional PhC's is highly dependent of the frequency regime of interest. For microwave PhC's (< 30 GHz), construction is

accomplished using standard machining tools and commercially available dielectric materials. However, at millimeter wave frequencies and into optical frequencies, micromachining and microlithography are required [16].

2.1.3 Three Dimensional Photonic Crystals

As the name implies, a three-dimensional photonic crystal is periodic in all three dimensions. There are an infinite number of geometries that a 3-D crystal can take, however, not all of them will have a complete band gap. Examples of typical geometries that do have a complete bandgap are a diamond lattice of air holes [17, 18, 19, 20], a drilled dielectric called a Yablonovite [21, 22, 23, 24, 25, 26], woodpile stack [27, 28, 29, 30], inverse opal [31, 32, 33, 34], and an alternating stack of 2-D crystals [35, 36, 37, 38, 39]. Examples of these geometric structures are shown in Figure 4.

Three-dimensional photonic crystals are the most difficult to fabricate. The first experimental demonstration of a 3-D PhC did not occur until 1991 [21] by Yablonovich. This first 3-D structure was created by drilling holes into a high dielectric material and operated in the microwave regime. Increasing into the optical regime, additional methods are needed. Methods such as stacking 2-D crystals layer by layer [29], micro-fabrication [40, 41], holographic lithography [42], and natural self-organized structures [43] have shown promise.
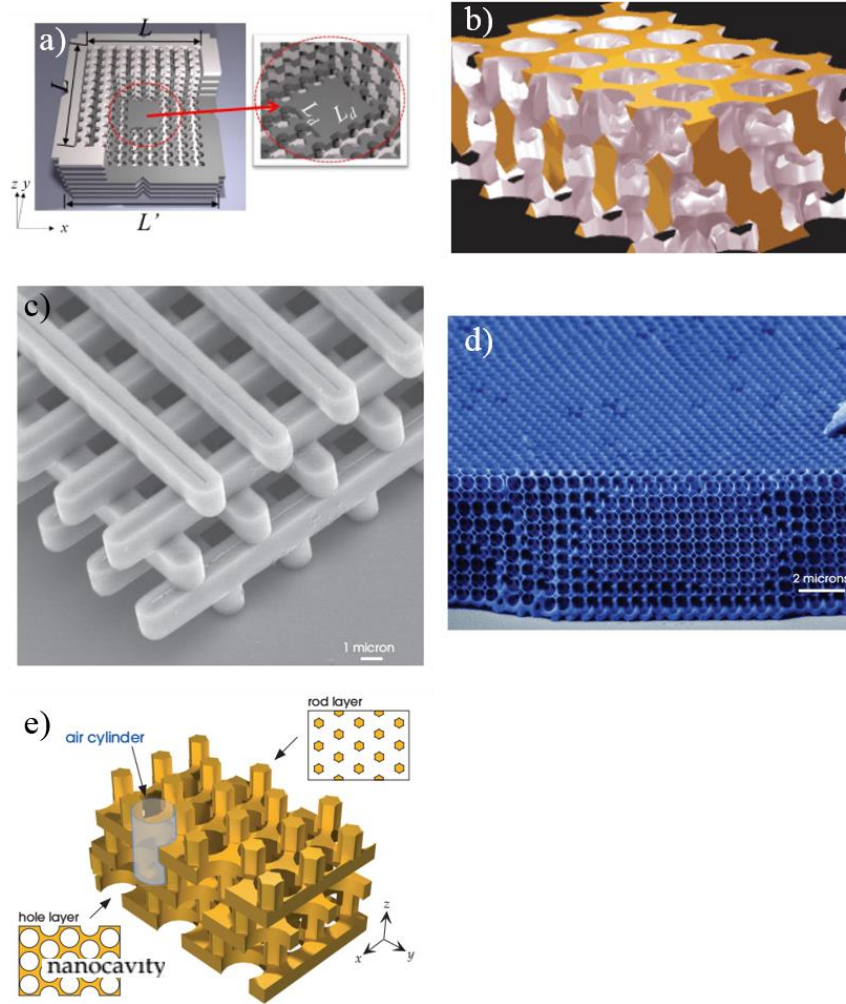
Figure 4 Example 3-D photonic crystal structures: a) Diamond lattice with air holes, b) Yablonovite, c) Woodpile, d) Inverse opal, e) Alternating stack of rods and holes. Adapted from [12] and [20].

2.2 Photonic Crystal Theory

Photonic crystals are a mixed dielectric medium and as such, Maxwell's equations can be employed to study the propagation of electromagnetic waves through them. Maxwell's equations can further be cast as a linear Hermitian eigenvalue problem, which brings them into a close analogy with the Schrödinger equation. This allows us to take advantage of established results from quantum mechanics, such as orthogonality of modes and perturbation theory. However, one

advantage that photonic crystals have over quantum mechanics is the lack of a fundamental scale, which makes photonic crystals scalable. This means that a photonic crystal designed in the microwave regime, can easily be scaled into the millimeter wave regime, it's just a matter of scaling all the dimensions linearly. This advantage will be utilized in the design of our photonic crystal structures in chapters 5 and 6. In the paragraphs that follow, I will summarize the theory behind photonic crystals that is laid out in more detail in Ref. [12].

Maxwell's equations for macroscopic media take the form of

$$\nabla \cdot \mathbf{B} = 0$$

$$\nabla \times \mathbf{E} + \frac{\partial \mathbf{B}}{\partial t} = 0$$

$$\nabla \cdot \mathbf{D} = \rho \qquad (2.1)$$

$$\nabla \times \mathbf{H} - \frac{\partial \mathbf{D}}{\partial t} = \mathbf{J},$$

where $\mathbf{B}$ is the magnetic induction field, $\mathbf{E}$ is the electric field, $\mathbf{D}$ is the displacement field, ρ is the free charge density, and $\mathbf{J}$ is the current density [44, 45]. We can further simplify our analysis by restricting to a mixed dielectric medium that is a composite of regions of homogeneous dielectric materials and is a function of position vector $\mathbf{r}$, and not changing in time. We also assume that there are no free charges or currents within the structure, $\rho = 0$ and $\mathbf{J} = 0$. In addition, we can also assume small field strengths, giving us linear media (no electric susceptibility, $\chi =$ 0), and that the material is macroscopic, isotropic, and dispersionless, making

$\mathbf{E}(\mathbf{r}, t)$ and $\mathbf{D}(\mathbf{r}, t)$ be related by scalar function, $\varepsilon_0 \cdot \varepsilon(\mathbf{r})$. Finally, we assume transparent materials, leading $\varepsilon(\mathbf{r})$ to be real and positive.

Using the above assumptions, and the fact that the vast majority of materials have vacuum permeability ($\mu = \mu_0 = 4\pi \cdot 10^{-7}$ H/m), we can state the above Maxwell's equations as

$$\nabla \cdot \mathbf{H}(\mathbf{r}, t) = 0$$
$$\nabla \times \mathbf{E}(\mathbf{r}, t) + \mu_0 \frac{\partial \mathbf{H}(\mathbf{r}, t)}{\partial t} = 0$$
$$\nabla \cdot [\varepsilon(\mathbf{r}) \mathbf{E}(\mathbf{r}, t)] = 0 \quad (2.2)$$
$$\nabla \times \mathbf{H}(\mathbf{r}, t) - \varepsilon_0 \varepsilon(\mathbf{r}) \frac{\partial \mathbf{E}(\mathbf{r}, t)}{\partial t} = 0.$$

Since the above equations are linear, the time and space elements can be separated into harmonic modes. This allows us to use complex notation,

$$\mathbf{H}(\mathbf{r}, t) = \mathbf{H}(\mathbf{r}) e^{-i\omega t}$$
$$\mathbf{E}(\mathbf{r}, t) = \mathbf{E}(\mathbf{r}) e^{-i\omega t}. \quad (2.3)$$

This reduces the two divergence equations to

$$\nabla \cdot \mathbf{H}(\mathbf{r}) = 0$$
$$\nabla \cdot [\varepsilon(\mathbf{r}) \mathbf{E}(\mathbf{r})] = 0, \quad (2.4)$$

which is interpreted as the structure having no sources or sinks of displacement or magnetic fields. This also means that the fields are made up of transverse waves.

The curl equations relate $\mathbf{E}(\mathbf{r})$ and $\mathbf{H}(\mathbf{r})$ and using the complex notation can be reduced to:

$$\nabla \times \mathbf{E}(\mathbf{r}) - i\omega\mu_0\mathbf{H}(\mathbf{r}) = 0$$

$$\nabla \times \mathbf{H}(\mathbf{r}) + i\omega\varepsilon_0\varepsilon(\mathbf{r})\mathbf{E}(\mathbf{r}) = 0. \tag{2.5}$$

These equations can be decoupled by dividing by $\varepsilon(\mathbf{r})$ and taking the curl. Combining the equations and combining ε_0 and μ_0 into the speed of light, $c = 1/\sqrt{\varepsilon_0\mu_0}$, the above equations become:

$$\nabla \times \left(\frac{1}{\varepsilon(\mathbf{r})}\nabla \times \mathbf{H}(\mathbf{r})\right) = \left(\frac{\omega}{c}\right)^2 \mathbf{H}(\mathbf{r}), \tag{2.6}$$

which is called the **master equation**.

Together with equation (2.4), equation (2.6) is used to solve for $\mathbf{H}(\mathbf{r})$ for any arbitrary $\varepsilon(\mathbf{r})$. Once $\mathbf{H}(\mathbf{r})$ is found, the electric field $\mathbf{E}(\mathbf{r})$ can be solved by re-arranging the second equation of (2.5) as follows:

$$\mathbf{E}(\mathbf{r}) = \frac{i}{\omega\varepsilon_0\varepsilon(\mathbf{r})}\nabla \times \mathbf{H}(\mathbf{r}). \tag{2.7}$$

Solving for H(r) and E(r) via equations (2.6) and (2.7) tells you everything you need to know about the fields within structure defined by $\varepsilon(\mathbf{r})$.

The master equation (2.6) is of the form of an eigenvalue problem and can be re-written as:

$$\widehat{\Theta}\mathbf{H}(\mathbf{r}) = \left(\frac{\omega}{c}\right)^2 \mathbf{H}(\mathbf{r}), \tag{2.8}$$

where $\widehat{\Theta}$ is an eigenfunction operating on the eigenvector $\mathbf{H}(\mathbf{r})$ and $(\omega/c)^2$ is an eigenvalue. The eigenvector $\mathbf{H}(\mathbf{r})$ are the spatial patterns of the harmonic modes and the eigenvalue is proportional to the square of the frequency of those

12

modes. The operator $\widehat{\Theta}$ is also linear, meaning that if $\mathbf{H_1(r)}$ and $\mathbf{H_2(r)}$ are solutions to (2.8) with the same frequency ω, then $\alpha\mathbf{H_1(r)} + \beta\mathbf{H_1(r)}$ is also a solution with the same frequency ω. The $\widehat{\Theta}$ operator is also what's called a Hermitian operator. Hermitian operators are defined such that the inner product of two vector fields $\mathbf{F}$ and $\mathbf{G}$ is the same no matter which vector field the operator is operated on,

$$\left(\mathbf{F}, \widehat{\Theta}\mathbf{G}\right) = \left(\widehat{\Theta}\mathbf{F}, \mathbf{G}\right). \tag{2.9}$$

The use of $\widehat{\Theta}$ in equation (2.8) is similar to quantum mechanics use of the Hamiltonian operator used in the wave function, which has the properties of having real eigenvalues, orthogonality, can be obtained by a variational principal, and can be catalogued by symmetry properties. See Table 1 below for a comparison between the two operators. Both operators are Hermitian, and as such, the $\widehat{\Theta}$ operator has these same properties. For detailed information on the Hamiltonian operator, see Refs [46, 47, 48].

Table 1 Comparison between the Hamiltonian operator in quantum mechanics and the $\widehat{\Theta}$ operator in electrodynamics [12].

	Quantum Mechanics	Electrodynamics
Field	$\Psi(\mathbf{r}, t) = \Psi(\mathbf{r})e^{-iEt/\hbar}$	$\mathbf{H}(\mathbf{r}, t) = \mathbf{H}(\mathbf{r})e^{-i\omega t}$
Eigenvalue problem	$\hat{H}\Psi = E\Psi$	$\widehat{\Theta}\mathbf{H} = \left(\frac{\omega}{c}\right)^2\mathbf{H}$
Hermitian operator	$\hat{H} = -\frac{\hbar^2}{2m}\nabla^2 + V(\mathbf{r})$	$\widehat{\Theta} = \nabla \times \frac{1}{\varepsilon(\mathbf{r})}\nabla \times$

The solutions to the master equation (2.6) are determined by the strength and symmetry properties of the dielectric function of the structure, $\varepsilon(\mathbf{r})$ [49]. In

13

the case of photonic crystals, $\varepsilon(\mathbf{r})$ is perfectly periodic and has discrete translational symmetry, in other words:

$$\varepsilon(\mathbf{r}) = \varepsilon(\mathbf{r} \pm l\mathbf{a}), \qquad (2.10)$$

where $\mathbf{a}$ is the lattice constant and l is an integer. Under these conditions, the solutions are characterized by a wavevector $\mathbf{k}$ and band index n. The **Brillouin** zone is the region of allowed wavevectors and the **band structure** consist of all solutions. A **bandgap** exists if there is a region of frequencies where there are no allowed modes for any $\mathbf{k}$ vector within the Brillouin zone. Additional information on the Brillouin zone can be found in Ref. [50].

For periodic-repeating media, such as photonic crystals, the solution to our master question takes the form of a **Bloch wave** [51], which has the form of

$$\psi(\mathbf{r}) = e^{i\mathbf{k}\cdot\mathbf{r}}. \qquad (2.11)$$

For two dimensional photonic crystals, like that shown in Figure 3, the magnetic field function solution becomes

$$\mathbf{H}_{(n,k_z,\mathbf{k}_\parallel)}(\mathbf{r}) = e^{i\mathbf{k}_\parallel\cdot\rho}e^{ik_z z}\mathbf{u}_{(n,k_z,\mathbf{k}_\parallel)}(\rho) \qquad (2.12)$$

where k_z, $\mathbf{k}_\parallel$, and n are indexing values for the modes of the crystal, ρ is the projection of $\mathbf{r}$ onto the xy plane, $\mathbf{u}(\rho)$ is a periodic function of the lattice. For those familiar with quantum mechanics and semiconductor physics, equation (2.12) is analogous to the Bloch function that gives rise to energy bandgaps, $\Psi_{\mathbf{k}n}(\mathbf{r}) = u_{\mathbf{k}n}(\mathbf{r})e^{i\mathbf{k}\cdot\mathbf{r}}$ [52].

For modes propagating strictly within the *xy* plane ($k_z = 0$) are reflection invariant and have mirror symmetry. This allows the separation of the mode into two polarizations, **Transverse-electric (TE)**, and **Transverse-magnetic (TM)**. TE modes have **H** normal to the plane while **E** is in the plane, $\mathbf{H} = H(\rho)\hat{\mathbf{z}}$ and $\mathbf{E}(\rho) \cdot \hat{\mathbf{z}} = 0$. TM modes are reverse, with **H** in the plane and **E** normal to the plane, $\mathbf{E} = E(\rho)\hat{\mathbf{z}}$ and $\mathbf{H}(\rho) \cdot \hat{\mathbf{z}} = 0$. One important note on nomenclature, normally polarization is given in relation to wave propagation, i.e. a TE wave would have its electric field perpendicular to the direction on propagation only. However, in 2-D photonic crystals, polarization in given in terms of the plane of periodicity.

As was previously discussed, the symmetry and periodicity of the dielectric lattice disallows certain frequencies to propagate through the structure, but in addition to frequency, the direction of propagation is also important. To show this, the equations above are solved for a 2-D photonic crystal with a square lattice of dielectric rods ($\varepsilon = 8.9$, r = 0.2a) and the resulting allowed **k** values are plotted in Figure 5. Both TE and TM polarizations are solved and plotted separately with red and blue lines respectfully. The horizontal axis represents the value of the in-plane $\mathbf{k}_\parallel$ vector. Γ, X, and M represent specific symmetry points within the Brillouin zone and together create the **irreducible Brillouin zone**, or smallest region within the Brillouin zone for which the $\omega_n(\mathbf{k})$ are not related by symmetry. As you move along the horizontal axis from Γ to X to M, $\mathbf{k}_\parallel$ moves along the edge of the of the irreducible Brillouin zone and the value of $\omega_n(\mathbf{k})$ is plotted. In terms of $\mathbf{k}_\parallel$, Γ, X and M are specified as $\mathbf{k}_\parallel = 0$, $\mathbf{k}_\parallel = \pi/a\,\hat{\mathbf{x}}$, $\mathbf{k}_\parallel = \pi/a\,\hat{\mathbf{x}} + \pi/a\,\hat{\mathbf{y}}$ respectfully. A

complete bandgap emerges for the TM mode only, and is shown in the shaded blue area in Figure 5. A complete bandgap is specified for only the region of frequencies in which no propagation can occur irrespective of direction. This only occurs if the maximum of one band is less than the minimum of the next higher band. The band structure shown in Figure 5 is specific to the square lattice of rods in air and for the specified rod radius and material, any deviation from these parameters and a new band diagram will need to be created. This example was chosen as this lattice type will be utilized extensively in the experimental sections.
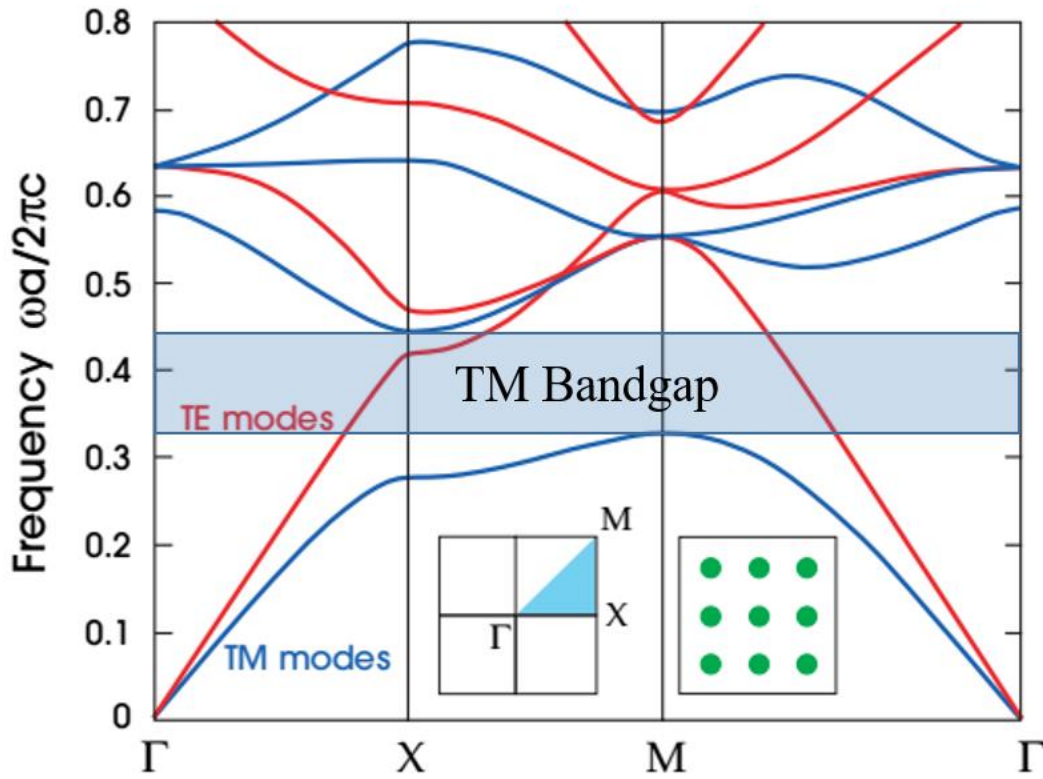
Figure 5 Photonic band structure for a 2-D array of dielectric rods ($\varepsilon = 8.9$, $r = 0.2a$) in air. Left insert shows the Brillouin zone with the irreducible zone shaded in blue, adapted from Ref. [12].

Figure 5 is limited in scope to a very specific set of criteria and is difficult to read given that the key feature of photonic crystals is the size and range of the

complete bandgap. Using the same equations, we can also solve for the band

structure for a range of values of rod size and material and calculate the bandgap

with the results. Shown in the top of Figure 6 is what's called a **gap recipe**. On

the left axis, it shows the bandgap size (TM mode only in this case) normalized by

the center frequency of the gap as a function of the contrast ratio between the high

index of refraction material (rods) and the low index material (usually air). Plotted

on the right axis is the optimal radius of the dielectric rods to achieve the largest

bandgap for the contrast ratio.
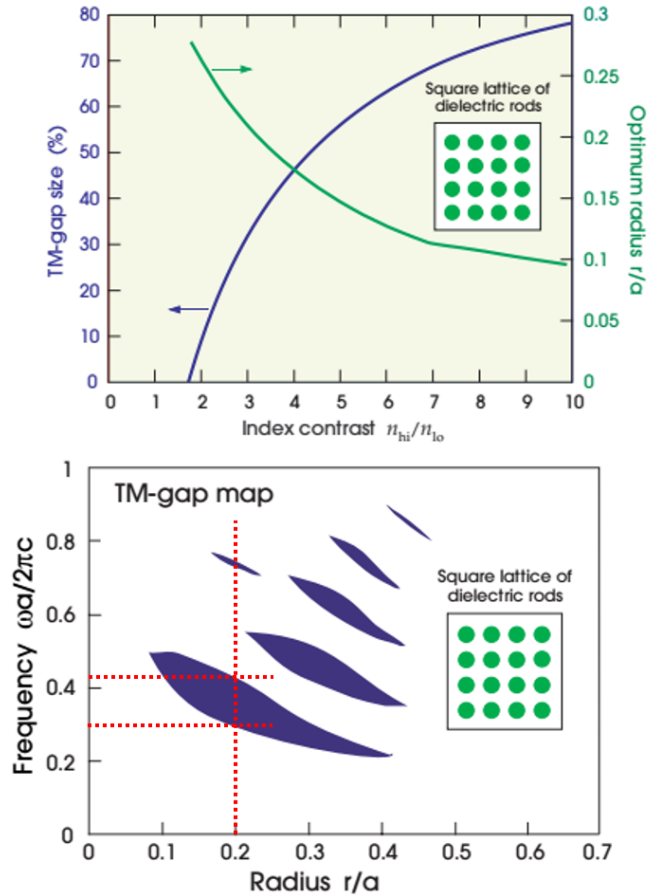
Figure 6 (Top) First TM mode gap recipe for square lattice of dielectric rods in air. (Bottom) Gap map showing TM mode band gap as a function of rod radius for a square lattice of dielectric rods (ε = 11.4). Adapted from Ref. [12].

The bottom of Figure 6 is called the **gap map**, and shows the specific gap frequencies contained within the bandgap for a range of rod radius for dielectric rods with ε = 11.4. As an example of how to interpret this figure, a vertical dotted red line at a radius of 0.2a is included. The bandgap frequencies for this radius are where the red line cross the dark blue shaded area and are indicated with the horizontal red lines at normalized frequencies of 0.35 and 0.44. In general, both TM and TE bandgaps are displayed within the same figure, however, for the specific example of a square lattice with rods of ε = 11.4 there are no TE bandgaps.

Plots like those shown in Figure 5, and more so Figure 6, tell you everything you need to know to achieve the desired bandgap for a photonic crystal. However, pure photonic crystals have limited use in practice. By adding "defects" into the crystal lattice, a wide range of behavior can be achieved. The types and behavior of defects will be discussed next.

2.3   *Photonic Crystal Defects*

As with pure semiconductors, the real power of photonic crystals is not achieved until intentional defects are added into the crystal. There are three types of defects that can occur in photonic crystals; surface, line, and point defects. These defects are illustrated in Figure 7.

18
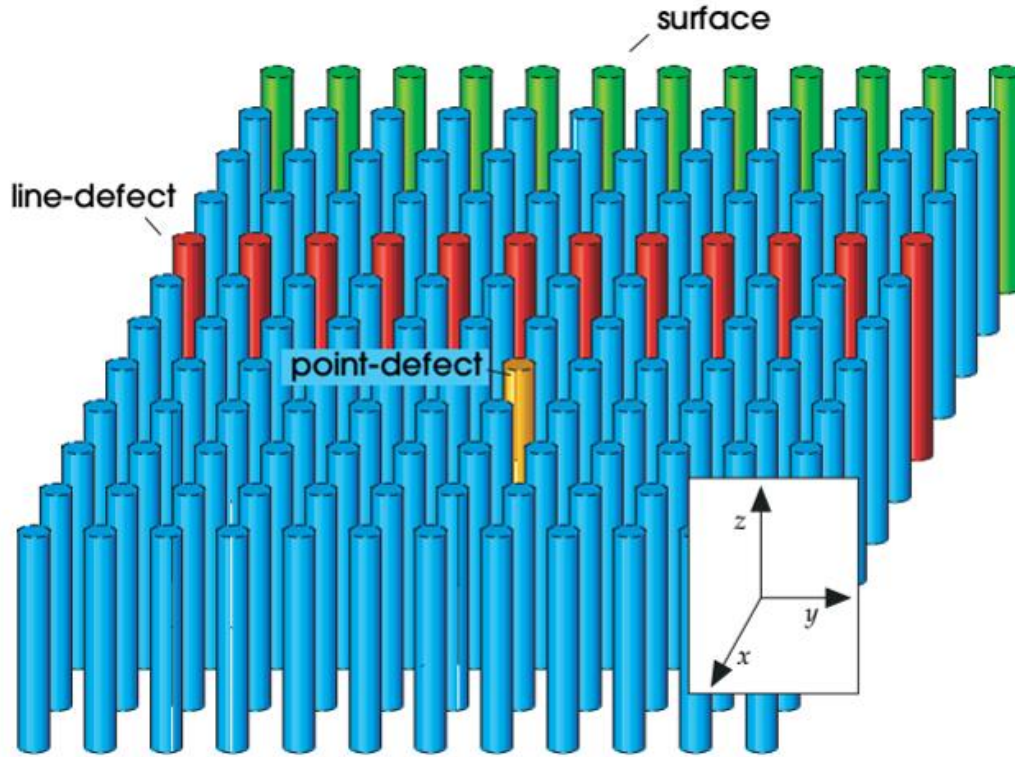
Figure 7 Schematic illustration of surface (green), line (red), and point (yellow) defects in a photonic crystal lattice (blue) [12].

The first type of defect, surface defects, are generally not desired, apart from a mirror. Surface defects occur at the interface between the crystal lattice and the surrounding medium, usually air or another dielectric. Additionally, there are three types of surface modes that can occur at the surface defect: light transmission, internally reflected light, and externally reflected light. Which surface mode occurs depends on the frequency of light in relation to the bandgap of the bulk crystal. For the purposes of the experimental work contained with this work, surface defects are inconsequential and will not be discussed any further. However, a complete and detailed description can be found within Ref. [12].

In contrast to surface defects, line defects are generally intentional and allow for light to be guided. Line defects are created by either removing unit cells (such as dielectric rods) in a linear fashion, or by modifying the unit cells, either by changing the size, shape, or material of the unit cells, or any combination of modifications. The modification of the linear area within the crystal lattice allows energy with a frequency within the bandgap to propagate in the direction of the line. All other wave vectors will see the bulk crystal and exponentially decay and thus be forbidden from propagating due to the bandgap. Shown in Figure 8 is an example of the electric field pattern resulting from the removal of a single column of dielectric rods in a square lattice of dielectric rods in air. The removal of the dielectric rods creates a waveguide by which electromagnetic energy is guided through the crystal.
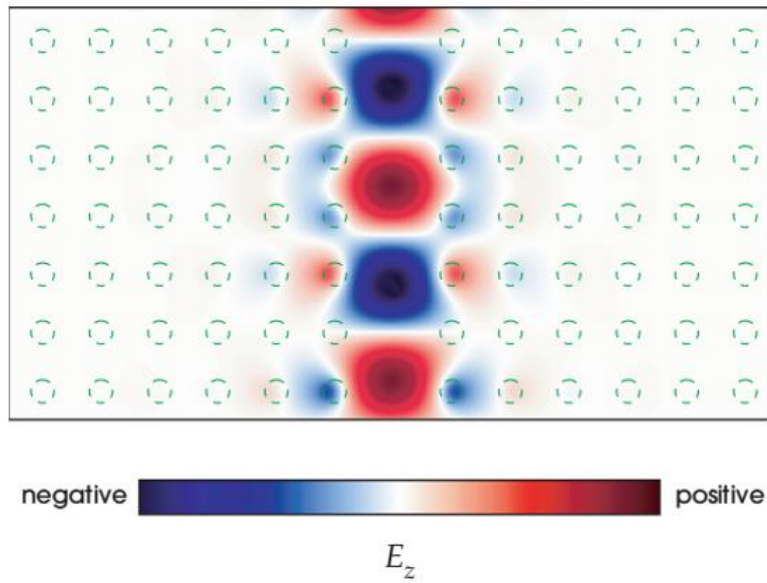
Figure 8 Electric field pattern for a linear defect within a 2-D photonic crystal of a square lattice of dielectric rods in air [12]. The EM wave propagates along the linear defect channel with the electric field oriented out of the page.

20

Similar to the line defect, point defects are created by either removing a single unit cell, or by modifying the cell by altering its size, shape, or material properties. The creation of a point defect creates a cavity by which electromagnetic energy resonates. Energy "leaks" into the cavity by evanescent waves penetrating the crystal. Once in the cavity, the energy resonates due to reflection caused by the bulk crystal and is effectively trapped.

Several modes of the electric and magnetic fields within the cavity are possible depending on the nature of the point defect. Shown in Figure 9 is an example of the different electric field modes that are possible in a square lattice of dielectric rods in air. These modes exist for specific frequencies, outside of those specific frequencies there is no resonance and the field pattern reverts to that of a uniform lattice. Shown in the top left, a monopole electric field (single lobe with radial symmetry in the x-y plane) is formed when the defect consists of a vacancy in the lattice. This is the simplest form of a point defect and will be used for the experimental results shown later in this work. Other modes, such as dipoles, quadrupoles, and hexapoles are created by altering the center defect radius or material.
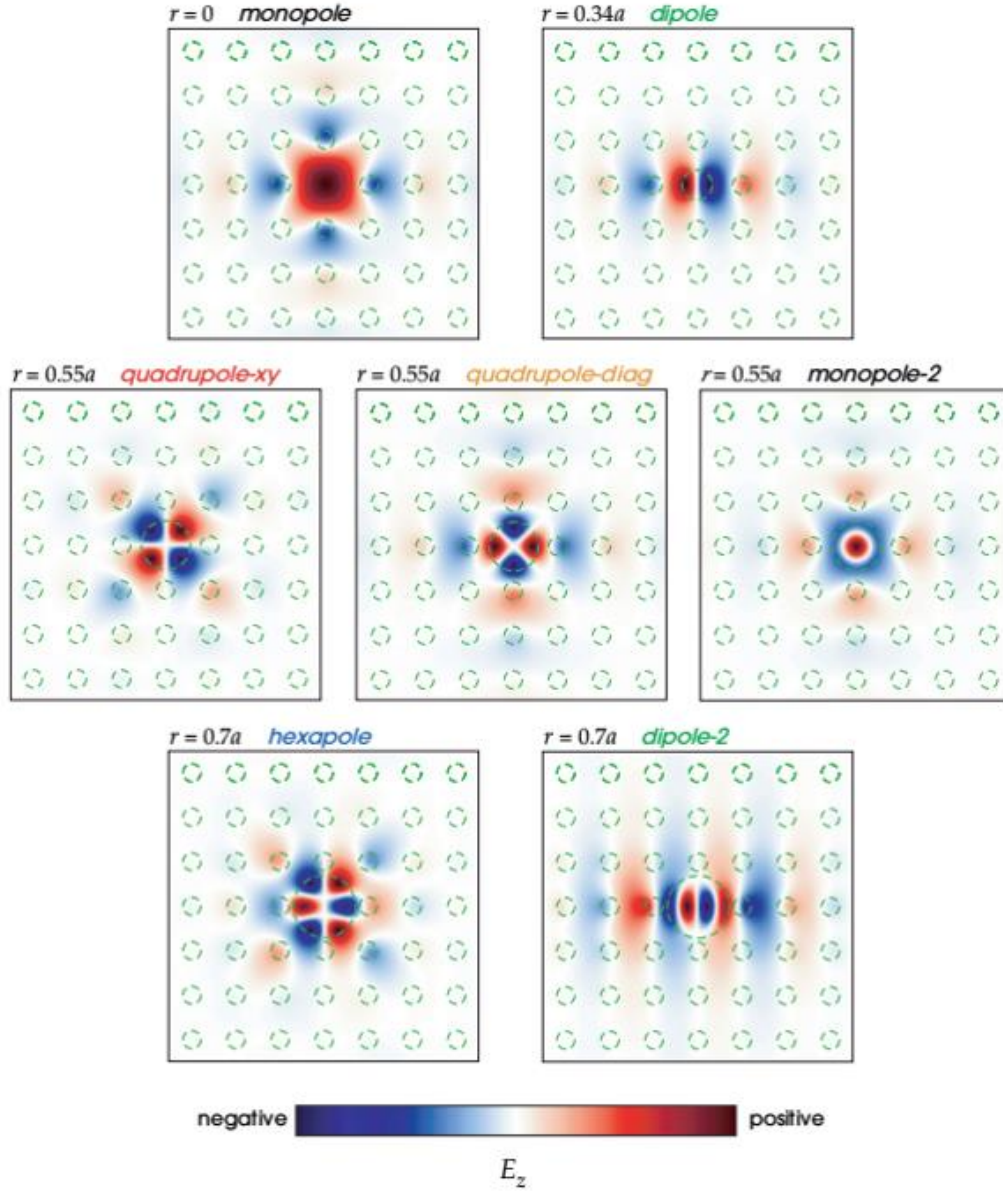
Figure 9 Electric field (E$_z$) patterns for a point defect in a square lattice in air. Various patterns are created by altering the radius of the defect. Starting from top left with a radius of 0 and a monopole pattern, to the bottom right with a radius of 0.7a with a dipole pattern [12].

In addition to altering the electric field pattern within the crystal, a point

defect has the additional effect of allowing energy to propagate through the crystal,

but only for a narrow band of frequencies surrounding the mode frequency [53].

The resulting behavior is that of a narrow band filter with a transmission curve like

22

that shown in the top of Figure 10. For this example, and input and output line defect channels energy into and out of the photonic crystal. A point defect in the center allows for a resonance and transmission at the resonant frequency by way of evanescent waves through the two rods into and out of the cavity. The strength of the resonance is quantified by what is known as the quality factor, Q, and is defined as $Q = f_c/\Delta f_{3dB}$, where f_c is the center or resonant frequency and Δf_{3dB} is the half-power bandwidth of the transmission curve [54].

A comparison of the electric field amplitude for an input at the resonant frequency and for a frequency off-resonance is shown in the bottom of Figure 10. In the off-resonance case, energy is able to propagate down the line defect and into the central cavity. However, the energy is not able to resonate and thus is not able to leak into the output line defect, resulting in the reflection of energy back into the input. When the applied frequency is on-resonance, energy travels through the input line defect and into the cavity. Once in the cavity, the energy resonates and gives up a little bit of energy each cycle into the output line defect. After a time period determined by the quality factor of the cavity, a steady-state condition occurs which results in the near complete transmission of energy through the output line defect.
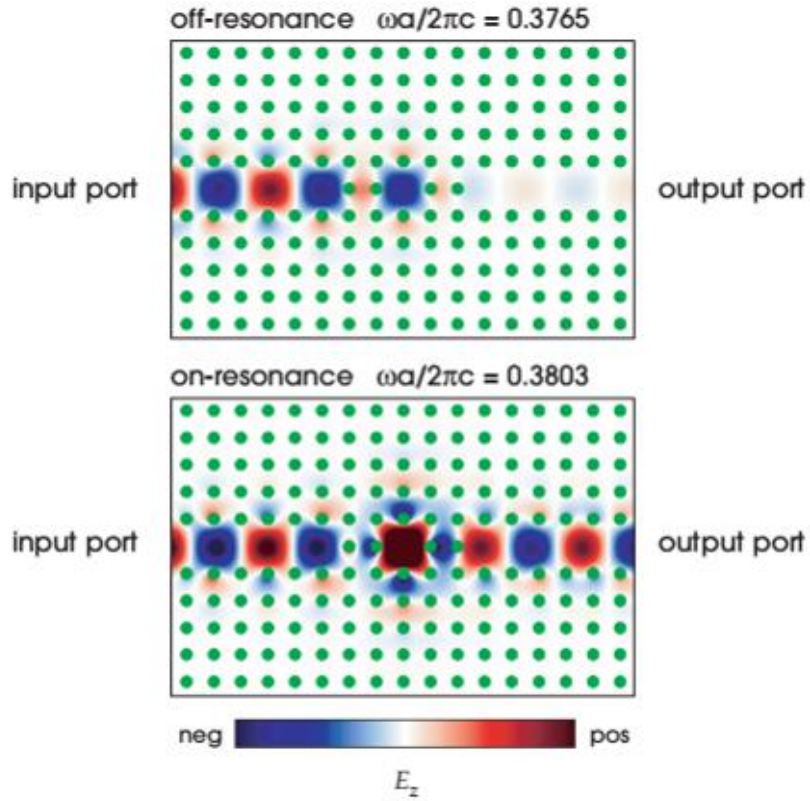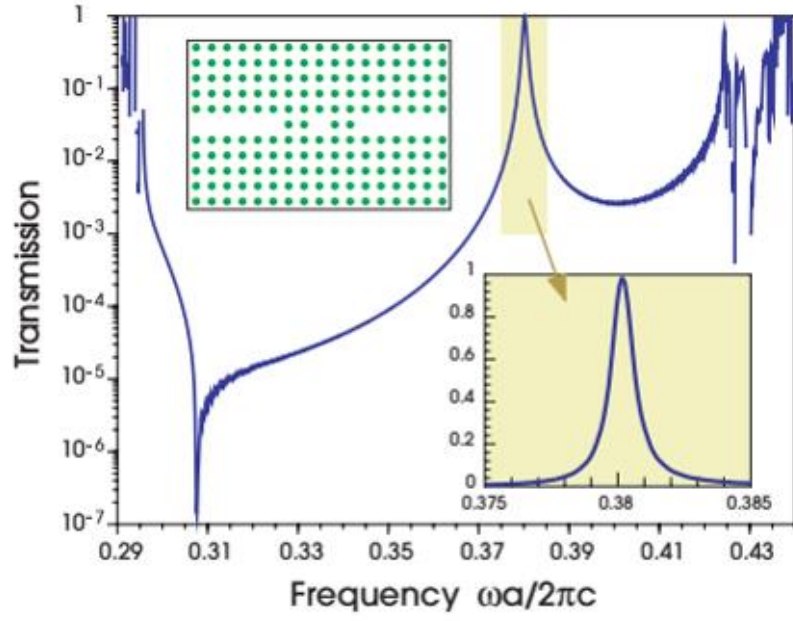
Figure 10 (Top) Transmission spectrum for square lattice of dielectric rods with two waveguide cavities and a point defect. (Bottom) Electric field patterns for off and on-resonance. Adapted from [12].

24

In terms of bandgap, a hole is created in the bandgap and the result is illustrated in Figure 11 for a rod radius of 0.2a. The central defect in the lattice creates a band within the bandgap that propagation is allowed. The remaining blue shaded area (for radius 0.2a) still disallows propagation.
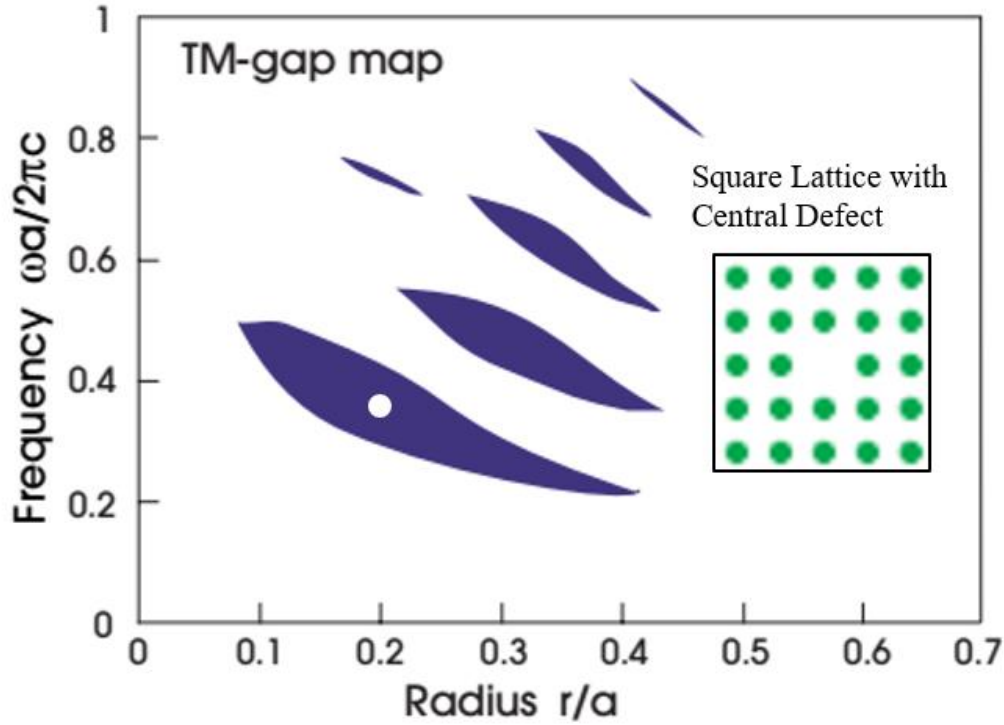
Figure 11 TM gap map for a square lattice of dielectric rods with a single dielectric rod removed creating a resonant cavity. Adapted from Ref. [12].

Defects in photonic the crystal lattice are essential for any application not involving complete reflection of energy (such as a Bragg mirror [55]). Devices such as waveguides [56, 57, 58, 59], filters [60, 61, 62] , resonators [63, 64, 65, 66, 67], couplers [68, 69, 70, 71, 72, 73], and most recently, plasma sources [11, 74] can be created using single or combinations of defects within the crystal lattice.

2.4   Reconfigurable Photonic Crystals

Recent advances in photonic crystal design have led to the ability to tune the optical properties of the device. This is highly desirable, as it allows for minor corrections in device performance and allows for additional functionality. There are three main categories of tunable photonic crystals, based on the method of tuning: mechanical, thermal, and opto-fluidics.

Mechanically tuned photonic crystals achieve tunability by means of mechanical force applied to the lattice structure. The stress on the structure results in a change in the periodicity of the lattice, which modifies the photonic band structure. One such example is shown Figure 12 and discussed in Ref. [75]. Here, mechanical actuators, controlled by a voltage source, squeeze and stretch the photonic crystal structure, which is made from silicon columns embedded in a flexible polymer film. The physical stress causes a physical change in size of the polymer, which alters the lattice constant and thus the band structure. A 10% change in pillar-to-pillar distance was achieved without excessive stress on the structure.
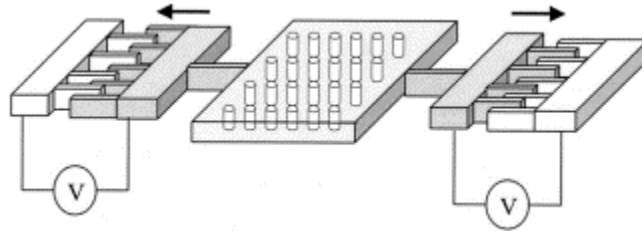
Figure 12 Schematic diagram of a flexible photonic crystal which is mechanically tuned by pressure exerted by NEMS/MEMS actuators [75].

Another means of mechanical tuning is discussed in Ref. [76] and shown in the left of Figure 13. In this example, two grated plates are stacked with tuning achieved by physically sliding the bottom plate. This adjusts the grating dimensions and shifts the center frequency of the filter, achieving a fractional tuning range of 6%. Another example of mechanical tuning is shown on the right of Figure 13. Here, tuning is achieved by adjusting the air gap between the lattice rods and the top metallic plate [1]. In this device, the size of the photonic bandgap is reduced as the air gap between the rods and the top plate increases. When the air gap approaches approximately 2 to 3 times the rod length the bandgap disappears, as the device no longer resembles a photonic crystal to an incoming electromagnetic wave.
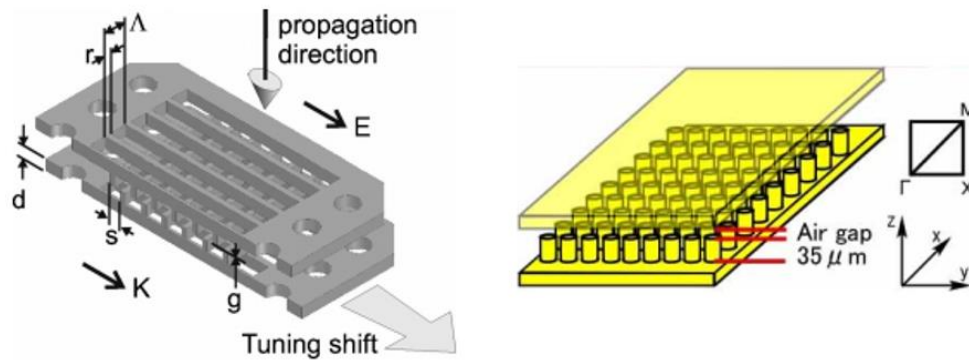
Figure 13 Schematic of mechanically tuned photonic crystal devices (Left)Narrow band-pass filter with tuning achieved by sliding the bottom plate [76]. (Right) Device tuning achieved by adjust the air gap between rods and top metallic plate [1].

Thermally controlled photonic crystals, as the name suggest, are tuned by changing the temperature of the lattice material, or by injecting a thermally controlled material into the lattice. Yoshino et al. [77] demonstrated in 1999 that liquid crystals injected into a 3-D photonic crystal opal structure could vary the

refractive index of the device by changing the temperature. This was again demonstrated in 2000 by Leonard et al. [78] using a 2-D microporous silicon photonic crystal with a liquid crystal injected into the pores. In both cases, the resulting change in refractive index due to temperature alters the transmittance of the device. Figure 14 shows experimental results from Yoshino et al. that confirms a change in refractive index (left) and a change in transmittance (right, inset) with temperature.
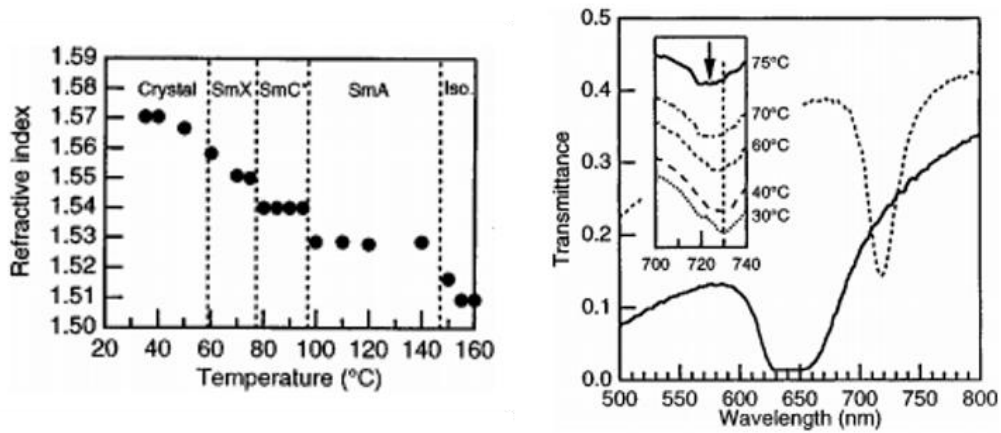
Figure 14 Experimental results of thermally controlled photonic crystals. (Left) Refractive index, n, as a function of temperature. (Right, Inset) Transmittance as a function of temperature. Adapted from Ref. [77].

In 2004, Chong et al. [2] showed that by using a similar method as Yoshino et al. at the change in refractive index can lead to a shift in resonant frequency of a photonic crystal with a central defect microcavity (PhC resonator). In this experiment, they applied a heater to the device to alter the temperature. Shown in Figure 15 (left) is an image of the experimental photonic crystal showing the central microcavity. On the right is the resulting transmission spectra for various current

levels to the heating element. This shows an increase in the resonant wavelength, or decrease in frequency, with increasing heater current (increasing temperature).
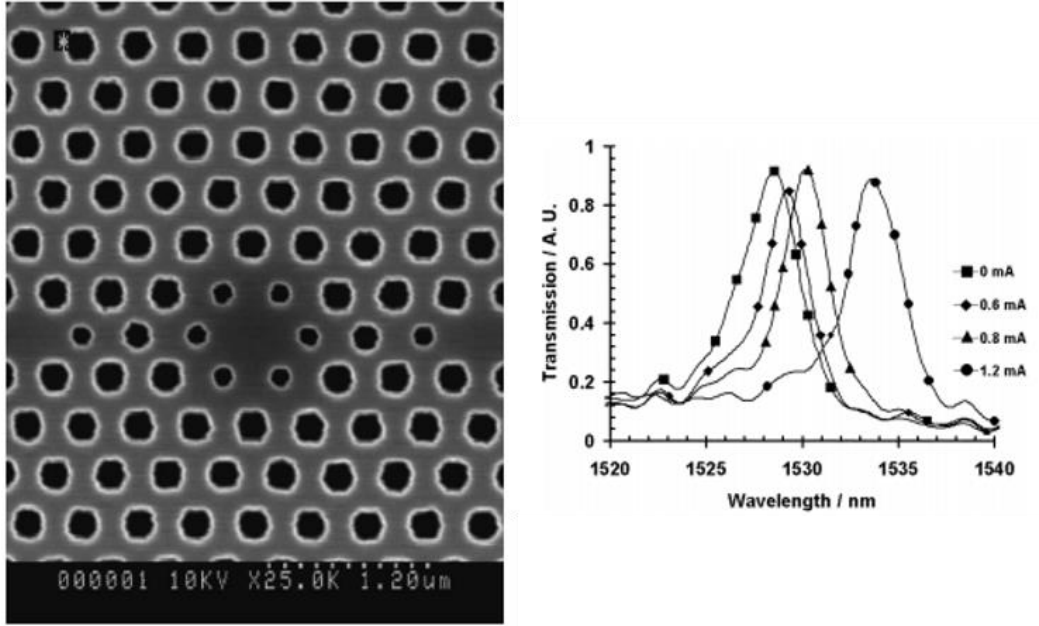
Figure 15 (Left) Photonic crystal with central microcavity. (Right) Transmission as a function of heater current. Adapted from Ref. [2].

More recently, Fegadolli et al. [79] and Fang et al. [80] have demonstrated the use of thermally sensitive material for use as the bulk material of the photonic crystal. Like previously, changing temperature modifies the refractive index of the material. However, it is the bulk material that is modified and not a separate material that has been injected into the lattice.

For tunable opto-fluidic photonic crystals, a high index contrast fluid is injected into the lattice structure in order to modify the optical properties of the device. In contrast with the thermally controlled devices with injected liquid crystals, here the fluid itself is a contrasting dielectric and required to be heated to

29

enact a change in index value. An example of such a device was demonstrated by Erikson et al. [81] in 2006 and is shown on the left in Figure 16. In this example, liquid is injected into the holes in the photonic layer of the structure. Two different liquids are injected depending on the desired optical properties, deionized water (n = 1.33) for when transmission is desired or $CaCl_2$ ($n = 1.44$) for when transmission is not desired. The right side of Figure 16 shows the modulation of energy transmission through the device as the inject fluid is modulation between DI water and $CaCl_2$.
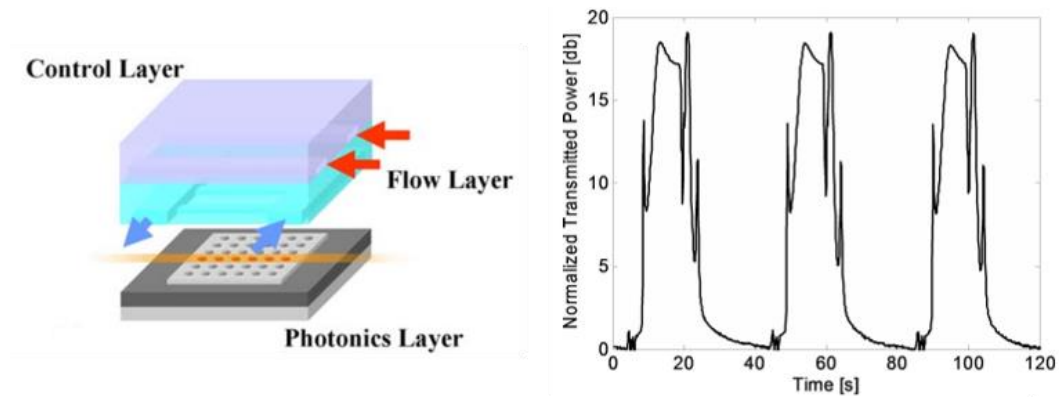
Figure 16 (Left)) Nano-fluidically tunable photonic crystal structure. (Right) Modulation of transmission due to nan-fluid injection. Adapted from Ref. [81].

Using the method described in the previous paragraph, Yang et al. [3] demonstrated the ability to create a tunable sensor using injected fluid. Figure 17(a) shows a schematic of the device, which consist of a waveguide structure with side coupled fluid channels (shown in green and red). Coupling of energy into the channels varies depending on the type of fluid in the channels and which channels contain fluid. Shown in Figure 17(a,b) is the transmission spectra of the device for a single H0 channel filled. With a filled side channel, the transmission spectra

shows a sharp drop in transmission within the larger transmission band and is similar to that of a notch filter. The notch frequency is determined by which channel is filled and with what type of fluid. This example is used for detection of biochemical interactions in aqueous environments.
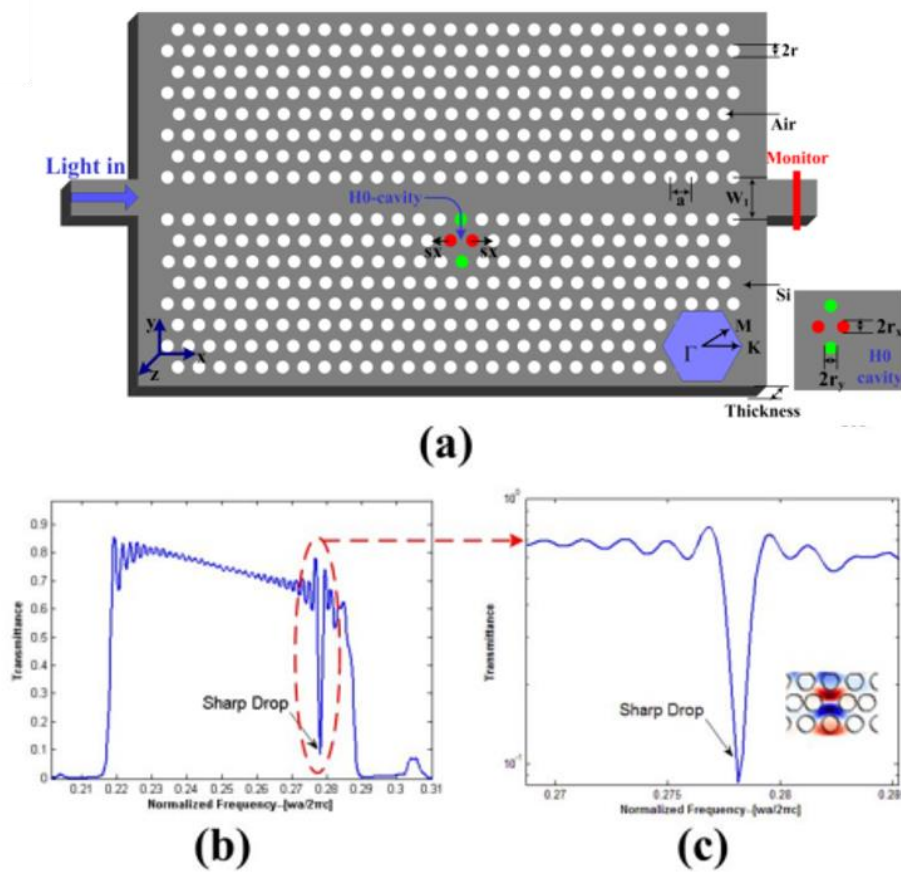
Figure 17 (a) Schematic of photonic crystal sensing device. (b) Output spectra with single H0 cavity filled. (b) Amplified image of area shown in the red circle of (b). Adapted from Ref. [3].

Recently, another method of achieving tunability has emerged, replacing one or more unit cells within the lattice with a plasma element, or by filling a lattice defect with plasma. Tunability is achieved by altering the permittivity of the plasma, thereby affecting wave propagation. This will be discussed in detail in Chapter 4.

31

3 Plasma Theory

As will be shown later, the experimental results included within this work are a combination of plasmas and photonic crystals. Specifically, I will exploit the resonance behavior of a photonic crystal with a central defect cavity in order to generate and sustain a plasma within the cavity formed by the defect. In this chapter, I will go over some basics of plasmas needed to understand the later experimental results.

3.1 Microwave Breakdown

The process of creating a plasma, or gas breakdown, starts with an applied electromagnetic field, by either applying voltage to electrodes or through a propagating wave. In the case of a cavity formed within a photonic crystal, an incoming electromagnetic wave at the resonant frequency "leaks" into the cavity through an evanescent mode and resonates within the cavity, as discussed in section 2.3. The electric field within the cavity increases due to the resonance. Free electrons within the cavity gain energy from the electric field and are accelerated. The energetic electrons collide with gas atoms and cause them to ionize. This process continues as more and more atoms are ionized because of the increasing number of free electrons. This process is called **avalanche breakdown** [82]. During this time period, the increasing electron density causes a change in permittivity, which reduces the electric field and the energy to the electrons. In addition, the rate of diffusion and recombination of electrons increases. The combination of these effects lead to a stabilization of the electron density and a steady-state condition. There are two time components included in the delay from

the application of the microwave/millimeter-wave field to the formation of a steady-state high density plasma: a random time before the appearance of a free electron to seed the avalanche breakdown (**statistical delay**), and the **formation time** of the avalanche [82, 83]. This process was modeled for a photonic crystal with central vacancy defect by Gregório et al. [11] and is shown in the top of Figure 18. Shown in black, the electric field within the cavity increases until the start of the avalanche, at which point the electric field decreases, then stabilizes. Shown in red is the electron density, which quickly increases during the avalanche process until it abruptly levels off to a steady state condition.

The changing permittivity of the plasma also effects the transmission of energy through the cavity. Shown in bottom of Figure 18 is an example from Ref. [11] of transmission spectra for various times during the avalanche process. Point a) represents the transmission just after the start of avalanche, while point e) represents the transmission at the end of the avalanche process. During this time, the transmission coefficient changes from ~0.35 to ~0.01, a 97% decrease (-15 dB). This is a specific example of the formation of a microwave plasma at 10 Torr and 10 GHz, frequency spectra during the avalanche breakdown process for other conditions would show a similar pattern. The timing of the breakdown process and the specific attenuation of the power due to the plasma is dependent on gas pressure and type, frequency, and input power.
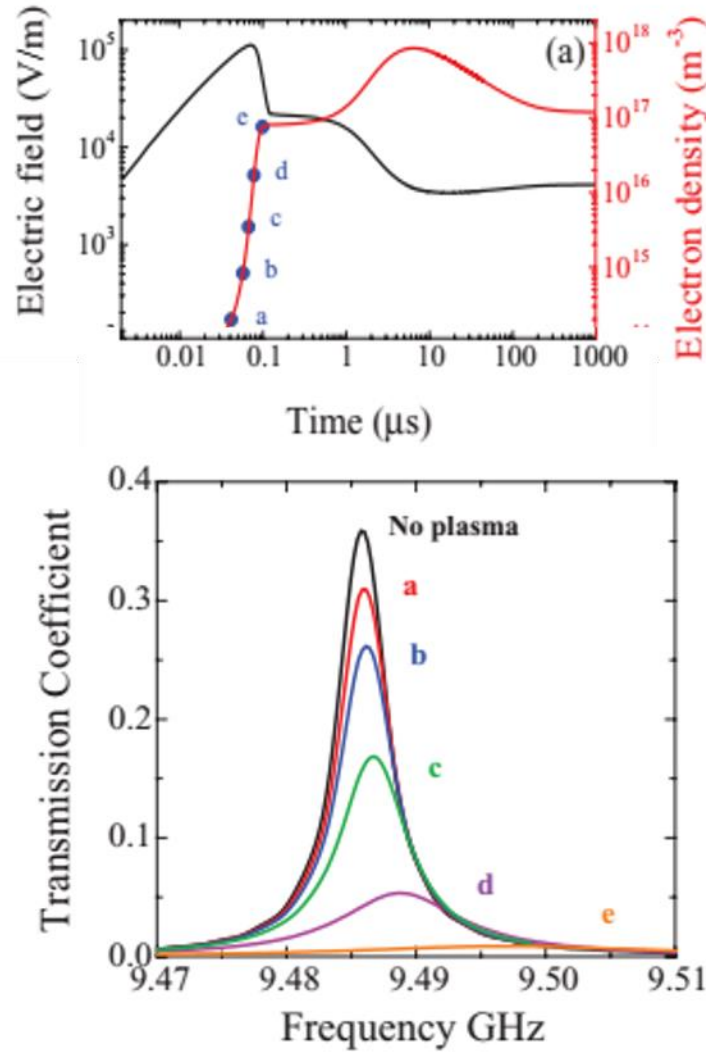
Figure 18 (Top) Electric field (black) and electron density (red) during avalanche breakdown. (Bottom) Resulting transmission during various stages of avalanche breakdown, letters a-e represent times from top figure. Adapted from Ref. [11].

3.2   Plasma Parameters

In general, plasma is a complex medium with dielectric and conductive properties. To determine which end of the spectrum the plasma lies, we need to determine the conductivity and dielectric properties. To do this we start with a plasma that is driven by an electric field of the form

$$E(t) = Re(\tilde{E}e^{j\omega t}). \qquad (3.1)$$

where ω is the angular frequency of the applied field. Next, we can define the complex permittivity of the plasma to ε_p, and place it into Maxwell's equation

$$\nabla \times \tilde{H} = \tilde{J}_c + j\omega\varepsilon_0\tilde{E} \equiv j\omega\varepsilon_p\tilde{E}, \qquad (3.2)$$

where $\tilde{J}_c + j\omega\varepsilon_0\tilde{E}$ is the total current, $\tilde{J}$, and ε_0 is the permittivity of free space.

For most plasmas, and certainly for the experimental plasmas contained within this work, we can assume quasi-neutrality, meaning there are the same number of electrons and ions ($n_e = n_i$). This coupled with the significant mass difference between electron and ions, and consequently there velocities, the conduction current, $\tilde{J}_c$, is mainly due to electrons given by

$$\tilde{J}_c = -en_e\tilde{u}_e \qquad (3.3)$$

where e is the electron charge and $\tilde{u}_e$ is electron velocity. The electron force equation for terms including force from the electric field and drag due to neutrals is

$$j\omega m\tilde{u}_e = -e\tilde{E} - m\nu_m\tilde{u}_e, \qquad (3.4)$$

where ν_m is the electron-neutral collision frequency. The above equations can then be combined to solve for the plasma permittivity,

$$\varepsilon_p = \varepsilon_0\left[1 - \frac{\omega_{pe}^2}{\omega(\omega - j\nu_m)}\right] \qquad (3.5)$$

where ω_{pe}^2, is the electron plasma frequency, and is given by

$$\omega_{pe} = \left(\frac{e^2 n_e}{\varepsilon_0 m_e} \right)^{1/2}. \tag{3.6}$$

The equation for the plasma permittivity has the form of a Drude model where the plasma frequency, ω_{pe}, is a resonance within the plasma and the collision frequency, ν_m, is the loss term [84].

The plasma permittivity equation (3.5) tells you everything you need to know about how the plasma will affect wave propagation through it. There are two general cases to consider based on if the plasma is collisionless ($\omega \gg \nu_m$) or collisional ($\omega \ll \nu_m$) and two subcases for each depending on if the wave is low frequency ($\omega \ll \omega_{pe}$) or high frequency ($\omega \gg \omega_{pe}$). For the collisionless, low wave frequency case, ε_p becomes negative and wave propagation is not supported (unless $\mu < 0$). For the collisionless, high wave frequency case, ε_p is mostly real, approaches ε_0, and is nearly lossless. For the collisional plasmas and low wave frequency, ε_p becomes negative, and acts as a lossy conductor. Once the wave frequency exceeds the plasma frequency, a collisional plasma acts as a lossy dielectric with the real part of ε_p approaching ε_0. These concepts will be discussed further in the next section on wave propagation through plasmas.

To get a more analytical sense of the dielectric properties of the plasma, we can break down ε_p into its real and imaginary parts, where the real part represents the dielectric strength and the imaginary part represents the loss. These equations are given by:

$$Re(\varepsilon_p) = \varepsilon_0 \left[1 - \frac{e^2 n_e}{\varepsilon_0 m_e (\omega^2 + v_m^2)} \right] \; and$$

$$Im(\varepsilon_p) = -\frac{\varepsilon_0 e^2 n_e v_m}{m_e(\omega^3 + \omega v_m{}^2)}$$

(3.7)

where I have substituted in equation (3.6).

To see the conduction properties of the plasma, we can use the Ohm's Law, $\boldsymbol{J} = \sigma \boldsymbol{E}$, in conjunction with equation (3.2) and (3.5), and substituting in σ_p for the plasma conductivity we have

$$\sigma_p = \frac{e^2 n_e}{m_e (v_m + j\omega)}.$$

(3.8)

An alternate form for expressing loss within a dielectric medium is called the loss tangent, $\tan \delta$, and is common in microwave systems. The loss tangent is defined as [85],

$$\tan \delta = \frac{-Im(\varepsilon_p)}{Re(\varepsilon_p)} = \frac{\omega_{pe}{}^2 v_m}{\omega(\omega^2 + v_m{}^2 - \omega_{pe}{}^2)}.$$

(3.9)

It is this form of loss that will be utilized later in the experimental section with regards for input into the 3D simulation software, Ansoft® High Frequency Structure Simulator, or HFSS.

Both the collision frequency and electron density are functions of the gas type and gas pressure, with electron density also being affected by the input power level. In the next section, I will utilize the above equations to show how the collision frequency and the electron density effect wave propagation for various

37

gas pressures and power levels that will be indicative of the experiments conditions discussed later.

3.3 *Wave Propagation in Cold Plasmas*

Depending on the environmental parameters, plasmas can range from nearly lossless dielectrics to near perfect conductors. In this section, I will discuss how the plasma parameters effect the propagation of waves. The experiments that will be shown later make use of cold plasmas, which are plasmas such that the thermal kinetic energy can be neglected for wave propagation, and the equations shown in this section will be reflective of that. For simplicity, the following assumptions will be made:

a) Cold plasma

b) No external magnetic field ($\mathbf{B_0} = 0$)

c) Plane wave propagation

d) Homogeneous and infinite plasma (no boundary effects)

e) Small amplitude waves (no second order effects)

f) Wave frequency greater than the ion plasma frequency (no ion motion)

In cold plasmas, there are two variables to consider, the electron density, n_e, and the average electron velocity, $\mathbf{u}$. These variables need to satisfy the continuity equation

$$\frac{\partial n_e}{\partial t} + \nabla \cdot (n_e \mathbf{u}) = 0 \qquad (3.10)$$

and the Langevin equation of motion for electrons

$$m_e \frac{D\mathbf{u}}{Dt} = q(\mathbf{E} + \mathbf{u} \times \mathbf{B}) - m_e \nu_m \mathbf{u}. \qquad (3.11)$$

Linearized for time harmonic fields, equation (3.11) becomes

$$-j\omega m_e \mathbf{u} = -e(\mathbf{E} + \mathbf{u} \times \mathbf{B_0}) - m_e \nu_m \mathbf{u}, \qquad (3.12)$$

where $\mathbf{B_0}$ is an externally applied magnetic field. However, in the absence of an external magnetic field, equation (3.12) becomes

$$\mathbf{u} = -\frac{e}{m_e(\nu_m - j\omega)}\mathbf{E}. \qquad (3.13)$$

Combined with Maxwell's equations, (2.1), equation (3.13) become

$$\mathbf{k} \times (\mathbf{k} \times \mathbf{E}) = -\frac{j\omega\mu_0 e^2 n_e}{m_e(\nu_m - j\omega)}\mathbf{E} - \frac{\omega^2}{c^2}\mathbf{E}, \qquad (3.14)$$

where $\mathbf{k}$ is the wave vector, which describes the propagation direction and the spatial frequency of the propagating wave.

It is useful to separate equation (3.14) into **transverse** (perpendicular to $\mathbf{k}$) and **longitudinal** (parallel to $\mathbf{k}$) components. The following relations are needed for the separation,

$$\mathbf{E} = \mathbf{E}_l + \mathbf{E}_t, \qquad (3.15)$$

$$\mathbf{k} \times \mathbf{E}_l = 0, \qquad (3.16)$$

$$\mathbf{k} \times (\mathbf{k} \times \mathbf{E}_t) = -k^2 \mathbf{E}_t. \qquad (3.17)$$

where k is the wave number and describes the spatial frequency of the wave. Combining equations (3.14) through (3.17) and separating yields the longitudinal equation

$$\omega^2(1 + j\, \nu_m/\omega) - \omega_{pe}^2 = 0, \qquad (3.18)$$

and the transverse equation

$$(\omega^2 - k^2 c^2)(1 + j\, \nu_m/\omega) - \omega_{pe}^2 = 0, \qquad (3.19)$$

Equations (3.18) and (3.19) are called dispersion relations and they relate the spatial frequency, k, to the temporal frequency, ω.

The dispersion relations are complex equations, however, it is most informative in terms of wave propagation to consider the real parts only, as the imaginary part deals with losses. Looking at longitudinal relation, equation (3.18), solving for the real part gives

$$\omega^2 = \omega_{pe}^2. \qquad (3.20)$$

Equation (3.20) states that longitudinal waves can only occur at the plasma frequency and they consist of electrons oscillations that are electrostatic in nature. For this reason, I will not consider them further as they play no role in wave propagation. Simplifying the real part of the transverse relation, equation (3.19), gives

$$\omega(k) = \frac{1}{\sqrt{2}} \left[c^2 k^2 - v_m^2 + \omega_{pe}^2 \right.$$

$$\left. + \left(4c^2 k^2 v_m^2 + \left(v_m^2 - c^2 k^2 \omega_{pe}^2 \right)^2 \right)^{\frac{1}{2}} \right]^{\frac{1}{2}},$$

(3.21)

which gives the temporal frequency as a function of the spatial frequency. As an example, equation (3.21) is plotted in Figure 19 for a plasma with electron density of $n_e = 10^{21}\ m^{-3}$ and for various values of v_m. Figure 19 and the dispersion relation will be discussed in more detail in the following paragraph.
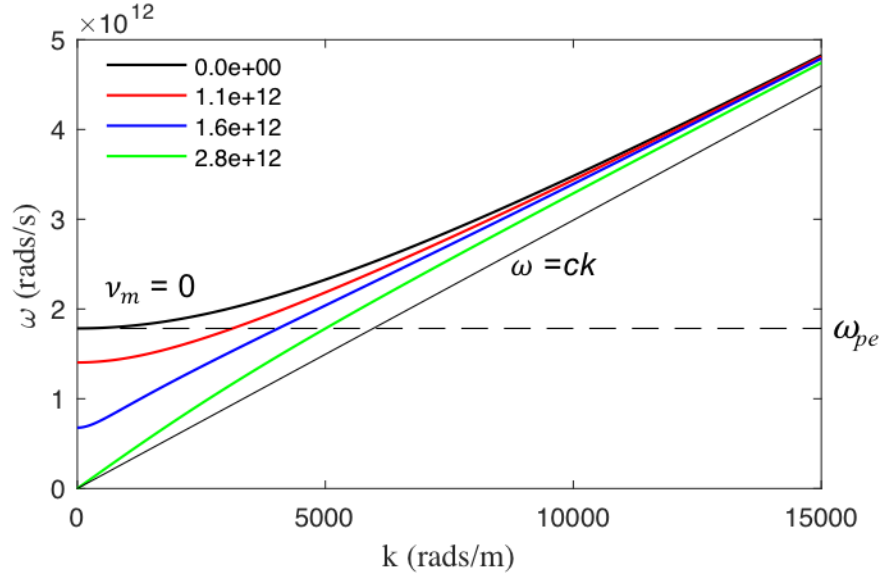
Figure 19 Dispersion relation for a plasma with electron density of $n_e = 10^{21}\ m^{-3}$. Collision frequencies, v_m, between 0 and 2.8 · 10^{12} s^{-1} are included to show the effect that collisions have on dispersion.

As previously discussed, the dispersion relation shows the relationship between the spatial and temporal frequencies. The light black line in Figure 19 shows the light line ($\omega = ck$), which represents propagation in free space. The thicker black line ($v_m = 0$) is wave propagation within a collisionless plasma. In

this case, no propagation occurs unless the wave frequency exceeds the plasma frequency, ω_{pe} (dashed black line). Between these two extremes lies propagation for plasmas with the full range of collisionality. By increasing the number of collisions, propagation for wave frequencies below the plasma frequency is possible. In all cases, the dispersion relation for each value of collision frequency approach's that of free space as the wave frequency is increased.

The above discussion involved infinite plasmas, however, this assumption is only valid when the plasma is much larger than the wavelength of the wave. For many plasma, including the microplasmas discussed later, this assumption is not valid. For waves with frequencies less than the allowed frequency, an evanescent wave penetrates the plasma. For large plasmas (large compared to the wavelength), the wave is attenuated and loses its energy within a few wavelengths. For smaller plasmas, the evanescent wave can propagate through the plasma with enough energy to return to a propagating mode once leaving the plasma.

The electron density of the plasma peaks in the center of the plasma and tapers to zero at the edge. From equation (3.6), ω_{pe} is a function of the electron density, resulting in the plasma frequency within the plasma being non-uniform. The effect of this is that a wave with frequency below that of the plasma frequency corresponding to the peak electron density will cross a point within the plasma with a plasma frequency matching that of the wave frequency. At his point within the plasma, energy from the wave transfers to the plasma in the form of Ohmic heating [86].

4   Plasma as an Element within Photonic Crystals

In recent years, researchers have been able to exploit the dynamic nature of the plasma permittivity as a reconfigurable element within photonic crystals. In this chapter, I will go over some of the recent work of other researchers to give some context to the experiments that will be shown in the remaining chapters.

In a series of experiments between 2004 to 2007 Hojo et al. [87, 88] and Sakai et al. [8, 9, 10] showed that an array of microplasmas had bandgap type properties. For waves with frequency higher than that of the plasma frequency, a plasma presents as a dielectric. An array of plasmas organized in a crystal structure would then behave like a photonic crystal, complete with an electromagnetic band gap. The microplasma array and experimental setup for their experiments is shown in Figure 20 and example transmittance is shown in Figure 21. In this experiment, they show that the microplasma array effects the transmittance of an incoming wave within the bandgap of 60 – 63 GHz, and that the level of attenuation is dependent of the density of the discharges, which is controlled by the applied DC voltage.
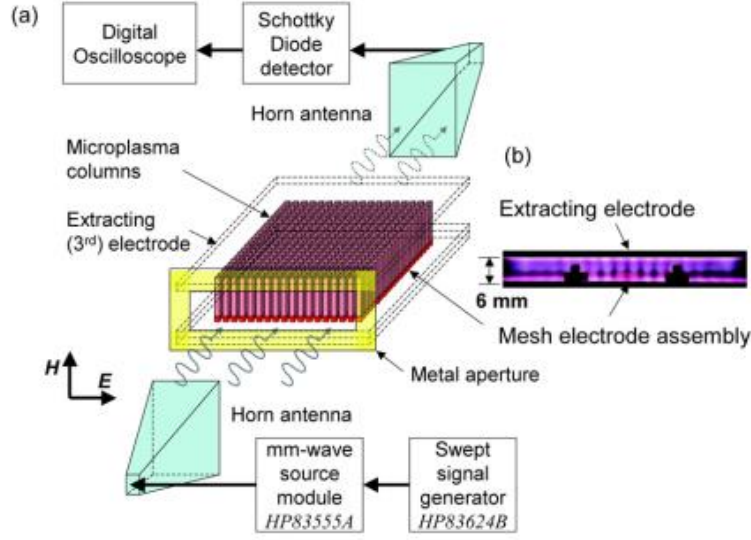
Figure 20 (a) Schematic of 2-D array of microplasma columns with experimental apparatus for transmission measurements. (b) Side view of array of microplasma columns. Adapted from Ref. [9].
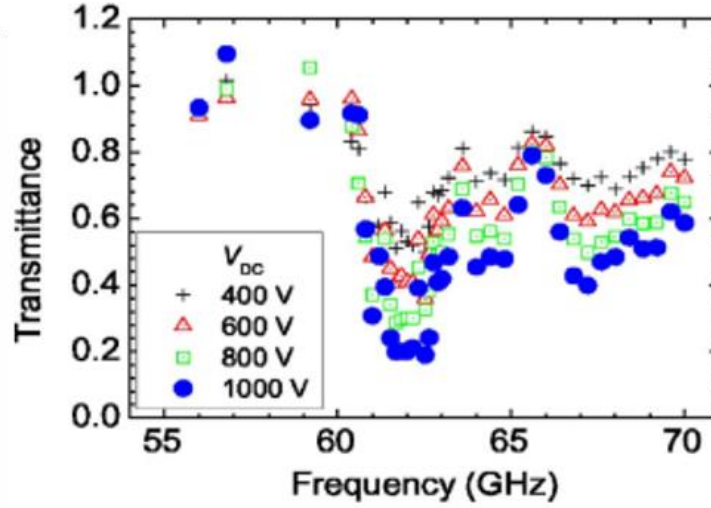
Figure 21 Transmittance of a microplasma array with dependence on discharge voltage. Adapted from Ref. [10].

In 2010, Lo et al. [7] conducted experiments using a single plasma element within a 2-D square metallic lattice. The plasma element is meant to act as a defect within the crystal. A schematic of the device is shown in Figure 22a. It consists of a square metallic lattice in a triangular formation. In this configuration, a wave

44

with frequency in the bandgap is completely reflected. However, if a single rod is removed, a defect is formed that allows for transmission through the crystal. For the experiment, a single metal rod was removed (central rod in figure), which creates a wave splitting effect. Simulation results of the electric field are shown in Figure 22b, which shows that the wave is split in two and travels through the lattice at 45° and -45°. Figure 22c shows the experimental results of the transmission through the lattice as a function of angle. The black line represents the case with no defect and shows no transmission at any angle as expected. The red and blue lines show the cases of the center metallic rod being replaced with a plasma discharge with 30 and 50 mA of discharge current respectfully. In these cases, transmission through the lattice occurs at ~50° as predicted by the model. These results also show that the effect of the plasma column is dependent on the electron density of the plasma, which is a function of the discharge current.

Using the concepts and results from above, researchers have been able to create devices such as coupling switches [89], filters [4], and waveguides with bends [6]. In each case, the device is reconfigurable by either turning on and off plasma elements within the lattice, or by varying the electron density of the plasmas.

In the preceding paragraphs, plasma elements were used to control the propagation of electromagnetic waves as part of a photonic crystal lattice. However, in each of these cases, the plasma elements were created and controlled by separate sources, not the incoming wave itself. Recently, a 2D self-consistent

model developed by Gregório et al. [11] showed that a photonic crystal with a central vacancy defect can self-initiate plasma formation and sustainment with only an incoming electromagnetic wave. The remainder of this work will show the process behind a photonic crystal design for self-initiated plasma formation and show and discuss experimental results of the device. Designs in the microwave and millimeter-wave frequency regime are presented.
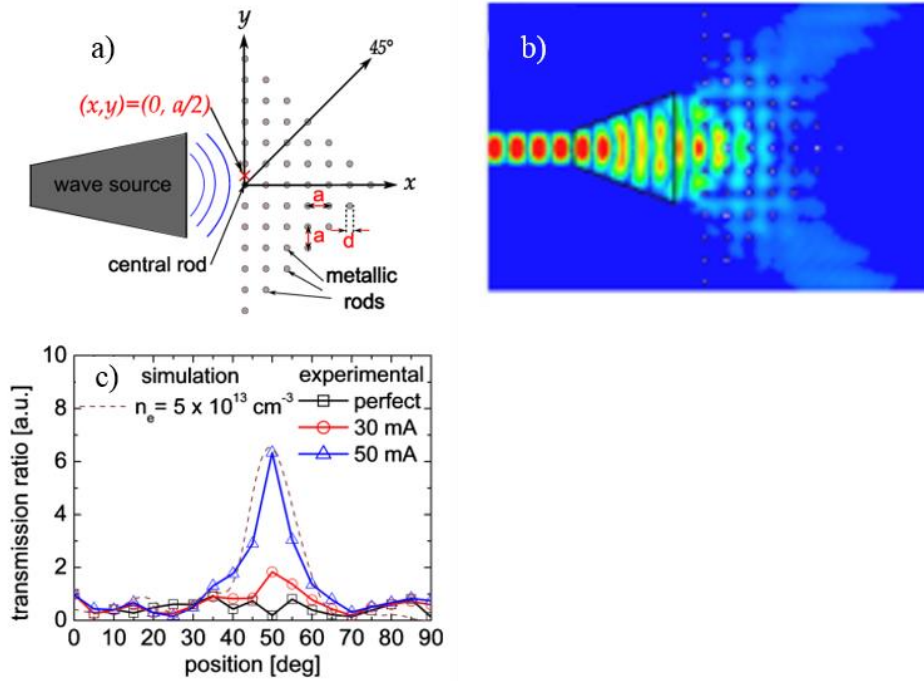
Figure 22 (a) Schematic of metallic PhC array. (b) Electric field with metal rod at (0,0) removed. (c) Transmission as a function of angle. Adapted from Ref. [7].

46

5 Photonic Crystal Plasma formation in the Microwave Regime

A photonic crystal resonator is realized by creating a single point defect in the lattice. Removing a single rod within the lattice creates a resonant cavity that magnifies the electric field within. The large electric field is then able to break down gas into a plasma. A simplified diagram of the device showing the resonant cavity and the two waveguide channels is shown in Figure 23. To excite the cavity, a line defect which serves as a waveguide channel is created by removing a line of rods leading up to the cavity. The number of remaining rods between the waveguide and cavity is a key parameter in determining the quality factor of the resonant cavity and will be discussed further in section 5.1. An additional waveguide is created on the opposite side of the cavity as the first waveguide to measure the transmission of power through the device and plasma.

Additional factors in the design of the photonic crystal are the height of the dielectric rods (in the $\hat{z}$ direction) and the number of rods in both directions of the plane ($\hat{x}$ and $\hat{y}$). A true two-dimensional photonic crystal would have an infinite number of rods in the plane as well as rods of infinite length, however this is not realizable. For real world applications, the number of rods in each direction is determined by the penetration of the electric field into the lattice. Increasing the number of rods increases the confinement, but with diminishing returns. The height of the rods is also required to be finite, and determines the strength of the electric field within the resonant cavity for a given input power. The effect of array size and rod length will be explored in section 5.1.

The final design factor for a finite lattice is in the boundaries. Photonic crystals work due to the permittivity difference between the lattice and its surrounding material. For this reason, conductive metal boundaries were chosen for the top and bottom walls ($\hat{x}$-$\hat{y}$ plane) to contain the electromagnetic fields within the lattice. Additionally, metal boundary walls were placed behind the input and output channels ($\hat{y}$-$\hat{z}$ plane), the reason for which will be discussed in section 5.1. The sides parallel to the waveguide channels ($\hat{x}$-$\hat{z}$ plane) were left open to observe the plasma characteristics within the resonant cavity.
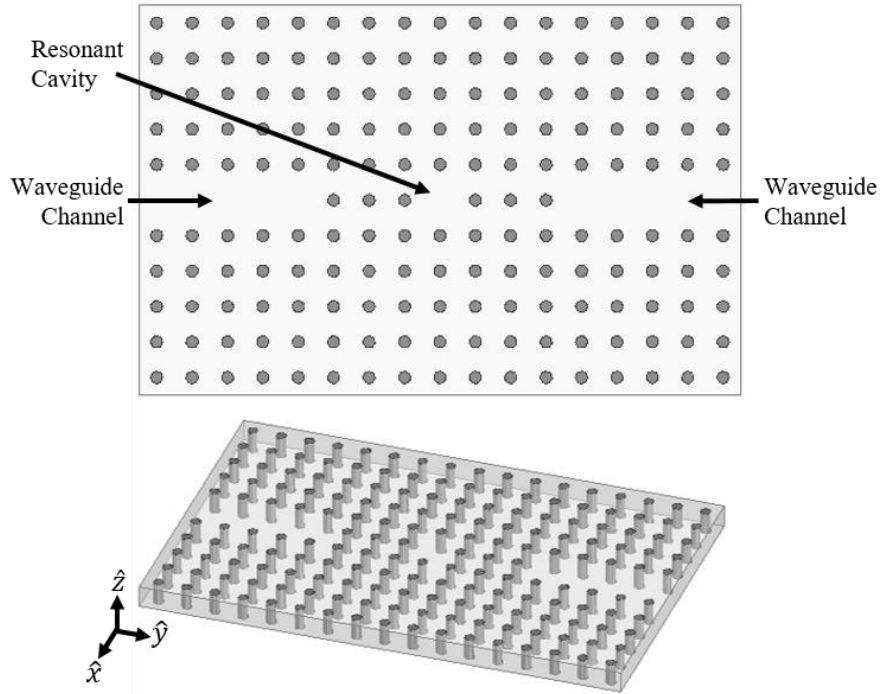
Figure 23 Simplified diagram showing a lattice of dielectric rods in air with a single point defect creating a resonant cavity with two line defects creating waveguide channels for input and output of power to the cavity. (Top) Top view of the array showing the waveguide channels and resonant cavity. (Bottom) Orthographic view of the device showing a finite rod height.

The critical aspect of designing any photonic crystal device is the electromagnetic bandgap, or the range of frequencies at which the electromagnetic

waves will not be permitted to propagate within the crystal lattice [49]. For a two-dimensional lattice with dielectric rods in air, the bandgap is determined by the permittivity, radius, and spacing of the rods. For the first device, a bandgap centered around ~8.5 GHz was chosen as this would produce a photonic crystal device that was large enough to be easily construct by hand, but small enough to fit inside our current vacuum chamber. Construction was additionally constrained by suitable commercially available materials. Alumina rods from CoorsTek® where chosen due to their high permittivity and low dielectric loss (ε_r = 9.8, $\tan \delta$ < .0001). To determine the physical parameters of the photonic crystal device, the freely available MIT Photonic-Bands (MPB) modeling software was utilized, details of which can be found in Ref. [90]. Using MPB, the photonic band structure for a square lattice dielectric rods (ε_r = 9.8) in air was solved and is shown in Figure 24 with axes scaled for a lattice spacing of 14.5 mm. To reduce complexity of the simulation, only the first two complete bandgaps are found as only the first gap is needed for our design purposes. A lattice constant (rod spacing) of 14.5 mm and rod diameter of 4.78 mm (radius = 2.39 mm, commercially available size) were selected to achieve a bandgap centered around the desired frequency of 8.5 GHz.
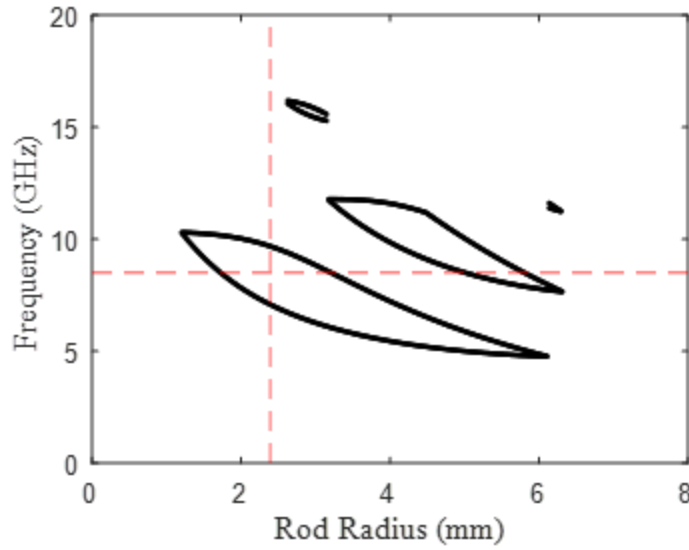
Figure 24 Bandgap structure for a photonic crystal with square lattice of dielectric rods (ε_r = 9.8) in air with a lattice constant of 14.5 mm. Red lines indicate the desired band center frequency of 8.5 GHz and selected radius of 2.39 mm.

5.1   Design Considerations

5.1.1   3-D Modeling Environment

Before the various design parameters can be investigated, a 3-D electromagnetic model must first be implemented. To achieve this, High Frequency Structure Simulator (HFSS) was employed. HFSS will be used extensively through this work and was chosen for its ease of implementation and accuracy. While HFSS is not able to simulate a plasma formation, nevertheless it is essential in understanding the electromagnetic properties and performance of the PhC device.

To begin simulations, the device from Figure 23 is built within HFSS using a custom material for the dielectric rods to conform to the properties of the Coorstek® AD-998 alumina. To create the custom material, the properties of HFSS's built-in alumina material were modified (Relative Permittivity = 9.8,

50

Dielectric Loss Tangent = 0.0001) and saved as a new material. As discussed

earlier, the lattice spacing was set to 14.5 mm on center and the rod diameter is set

to 4.78 mm. A vacuum box, set to the height of the dielectric rods (to be determined

later) surrounds the device, with additional spacing around all sides (except top and

bottom) set to 7.25 mm (half of the lattice spacing) from the center of the dielectric

rods around the edges. The physical dimensions of the PhC device just described

are shown in Figure 25.
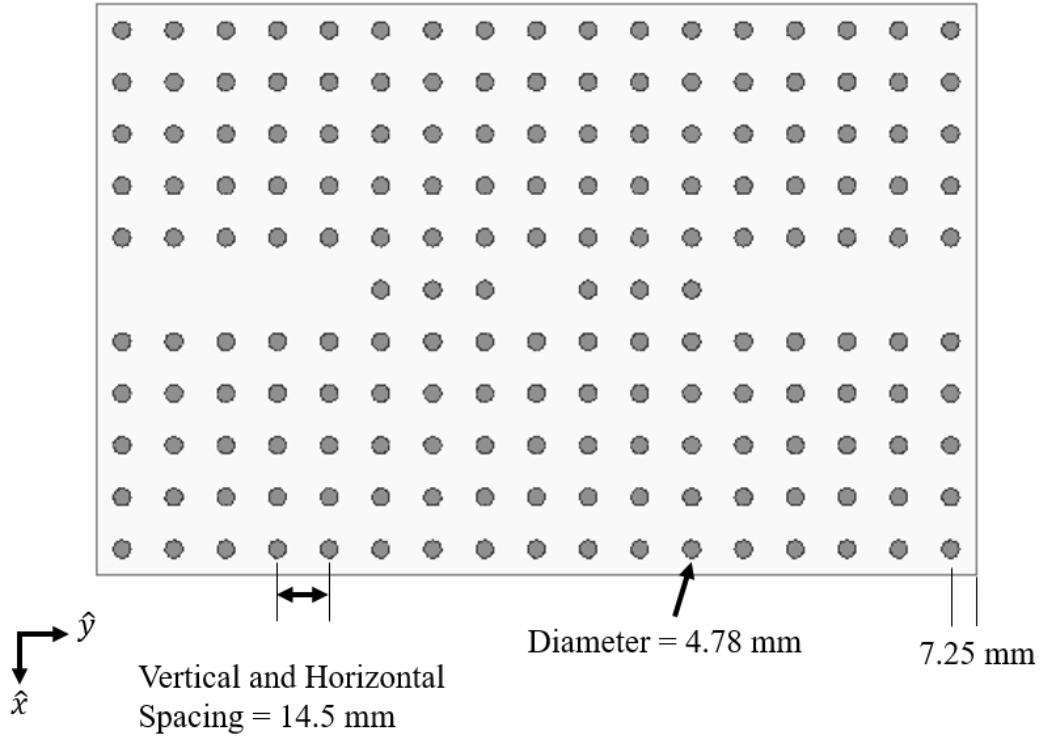
Figure 25 Physical dimensions of the 8.5 GHz PhC device for use in HFSS

To complete the HFSS model, boundary conditions and ports are needed to

set the correct electromagnetic environment and are depicted in Figure 26. To

supply and collect electromagnetic energy, waveguide ports are added to each end

of the device ($\hat{y}$ and $-\hat{y}$ directions). The ports have a fixed width and height corresponding to rectangular waveguide dimensions for the desired frequency band (WR-90, 0.9 inches wide by 0.4 inches tall). The actual device will be sandwiched between two copper plates (top and bottom) and is simulated in HFSS using perfect electric boundaries for simplification. Radiation boundaries are added to the sides ($\hat{x}$ and $-\hat{x}$ directions) to simulated open boundaries of the actual device. Finally, perfect electric boundaries are added to the port sides ($\hat{y}$ and $-\hat{y}$ directions). The perfect electric boundaries act as perfect conductors and reflect all electromagnetic energy back into the device. The radiation boundaries act as free space boundaries allowing electromagnetic energy to pass through with no reflections. These are needed to allow for the actual device to have open boundaries for visual inspection of the plasma.
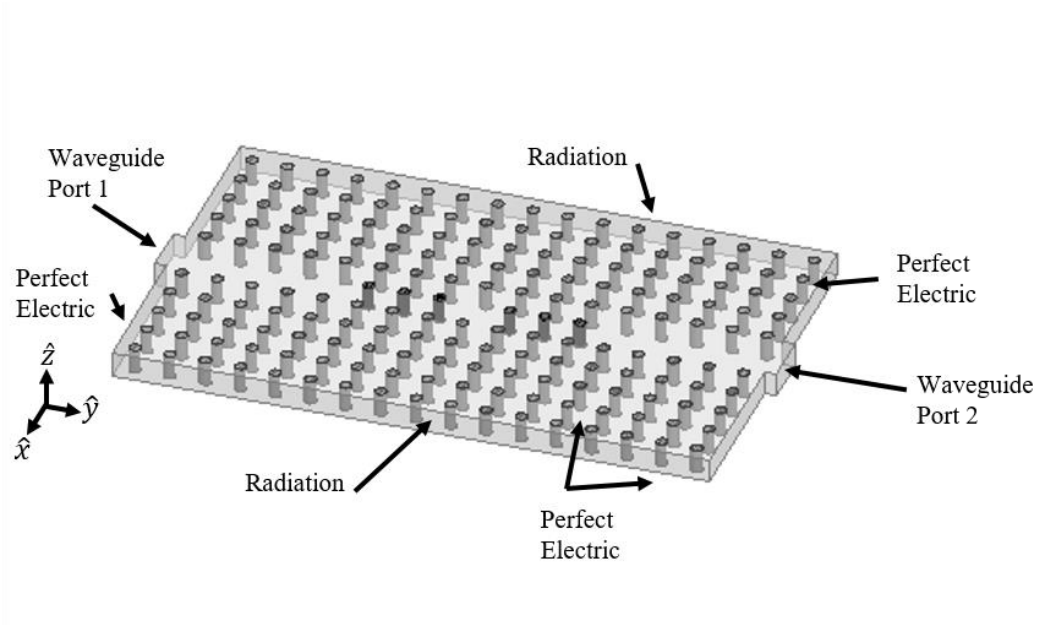
Figure 26 Simplified diagram of the PhC device showing the ports and boundary conditions for use in HFSS.

5.1.2   Number of Resonator Rods

As mentioned earlier, a resonant cavity is formed by creating a point defect within the lattice. However, energy from the input also needs to be able to enter the cavity as well as leave the cavity to the output. The amount of energy transferred in and out of the cavity is determined by the number of dielectric rods between the cavity and the input and output line defects. Given that the purpose of this device is to break down a gas into a plasma, a high quality factor and a strong electric field is the design goal. As a secondary goal, a high transmission rate at the resonant frequency is also desired.

Using HFSS, the device pictured in Figure 23 was simulated with a rod height of 10.16 mm (0.4 in) and the resonant frequency of the device was determined using a frequency sweep. The number of dielectric rods on either side of the cavity was varied from one to four to determine the effect on resonant frequency and transmission coefficient. The simulated transmission (left) and reflection (right) coefficients are shown in Figure 27. The resonant frequency, which occurs at the peak transmission and negative peak reflection, increases slightly as the number of dielectric rods is increased. The increase in resonator rods serves to constrict the effective cavity length by increasing the containment of electromagnetic energy. This reduction in effective cavity length leads to the small increase in resonant frequency as the number of resonant rods increase. This effect

is relatively small as the resonant frequency only increases from 8.356 GHz with one rod to 8.389 GHz using four rods, a 33 MHz increase (0.4%).
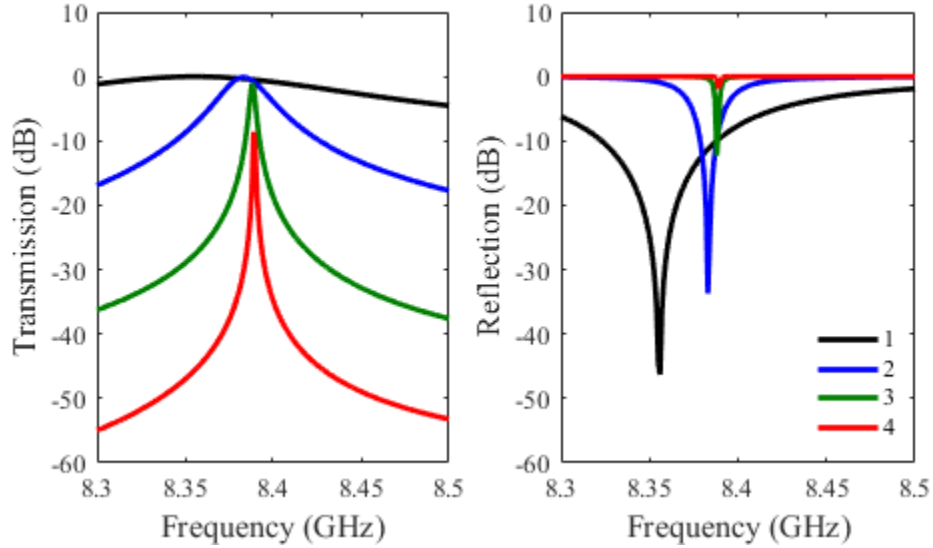
Figure 27 Simulated transmission (left) and reflection (right) of the PhC device for various number dielectric rods on each side of the resonant cavity.

To be an effective device, a significant amount of the input power should be transmitted through the device to the output, this requires a high transmission coefficient. From Figure 27, the number of resonator rods has a significant effect on the transmission rate of the device, as well as its bandwidth and quality factor. For the single rod case, a very high transmission coefficient of -0.01 dB is found with a bandwidth of 205 MHz (2.5 %). This relatively broad bandwidth leads to a quality factor of only 40. For the four rod case, a low transmission coefficient of -8.6 dB is found, but with a very narrow bandwidth of only 1.4 MHz which gives a quality factor of ~6100. While the four rod case has the desirable quality factor, the low transmission rate is not acceptable in many applications. A compromise

case of three rods is found to have an acceptable transmission coefficient of -1.1 dB, a narrow bandwidth of 3.2 MHz, and a high quality factor of ~2600.

In each configuration, the peak electric field intensity occurs at the same frequency as the peak in the transmission coefficient and is shown for the three rod case in Figure 28. The electric field within the cavity is uniform in the $\hat{z}$ direction (out of page). It is maximum in the center of the cavity and decreases rapidly towards the surrounding rods. A similar electric field pattern occurs for all cases, but with varying field intensity.
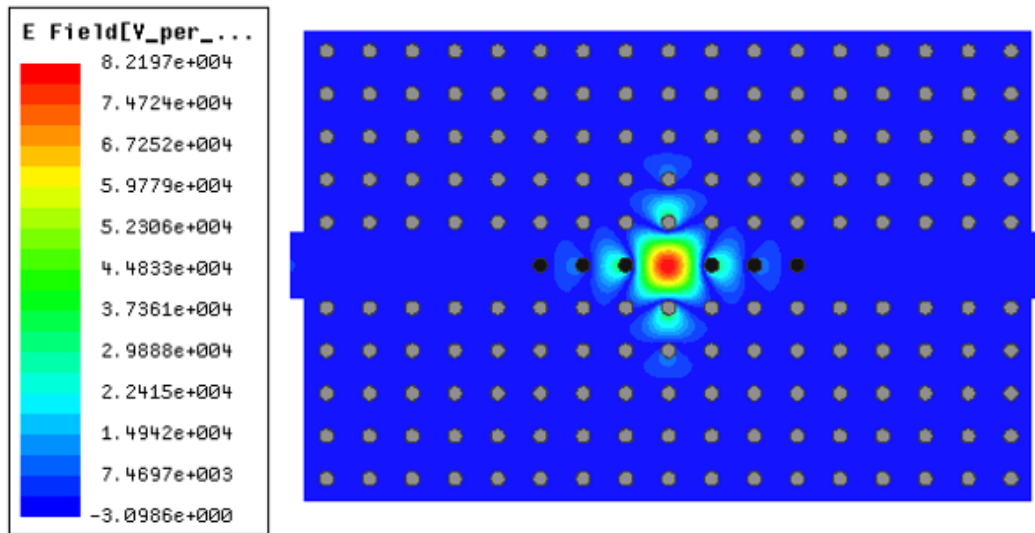
Figure 28 HFSS simulation of the complex electric field amplitude for a 1 W input and for three resonator rods on each side of the resonant cavity.

As with the quality factor and transmission coefficient, the number of resonator rods has a large impact of the electric field intensity. Shown in Figure 29 is the peak electric field intensity for 1 to 4 resonator rods on each side of the cavity. For the single rod case, a peak electric field magnitude of 10.9 kV/m was achieved

using 1 W of input power, which is in stark contrast to the four rod case of 93.1 kV/m, a greater than 8X increase in electric field intensity.
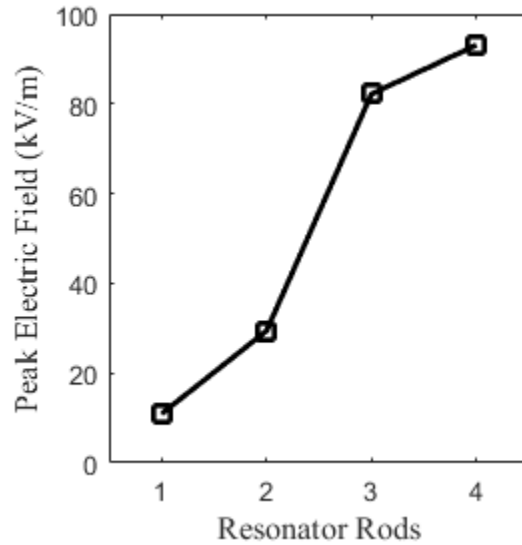
Figure 29 Peak electric field amplitude for 1 W of input power at the resonant frequency as a function of the number of resonator rods on each side of the cavity.

A summary of the performance characteristics of the PhC device in relation to the number of resonator rods is found in Table 2. While the four resonator rod case has the highest quality factor and electric field intensity, which is the primary goal, the transmission coefficient is unacceptably low at -8.6 dB (13.8 %). A more reasonable configuration is shown to be the three resonator rods case. The quality factor (Q ~2600) and electric field (82.2 kV/m) are acceptably high enough to cause gas breakdown, while also maintaining a reasonably high transmission coefficient of -1.1 dB (77.6 %). For these reasons, three resonator rods on each side of the

resonant cavity was chosen to give the best tradeoff between electric field intensity and output power transmission and will be used for the remainder of this work.

Table 2 Summary of the effect of the number of resonator rods has on performance characteristics. All values obtained using HFSS with 1 W of input power.

Resonator Rods	f_0 (GHz)	Transmission (dB)	Reflection (dB)	BW (MHz)	Q	E (kV/m)
1	8.356	-0.02	-46.3	205.6	41	10.9
2	8.383	-0.1	-33.7	27.7	303	29.4
3	8.388	-1.1	-12.3	3.2	2634	82.2
4	8.389	-8.6	-1.9	1.4	6097	93.1

5.1.3 Array Size

The size of the photonic crystal array determines the containment of the electromagnetic field within device, the larger the array, the more containment is achieved. However, for practical purposes, the array size can be reduced to achieve a reasonable level of containment. In HFSS, the vertical array size ($\hat{x}$ direction) was varied from 3 to 17 rods (odd numbers only) and the complex electric field amplitude was observed within the PhC device. Shown in Figure 30 are electric field plots for vertical array sizes of 3 (bottom), 7, 11, and 17 (top). For the vertical array size of 3, the electric field containment is poor and as a result, energy is predominantly radiated out the sides of the device. In addition, the electric field within the center vacancy and the output line defect is quite low. Increasing the vertical array size to 7 (second from bottom) increases the electric field containment considerably, however, a significant amount of energy is still leaked outside of the device. At the top of Figure 30, a vertical array size of 17 has almost complete containment of the electric field within the device. As a result, very little energy is

57

leaked and a significant electric field is able to build within the center vacancy. Additionally, the electric field in both the input and output channels achieve parity. Reducing the vertical array size to 11 (second from top) still shows significant electric field containment, a high electric field within the center vacancy, and equal electric field within the input and output channels.

While Figure 30 shows the electric field within the PhC device, plotting the electric field in this matter is too subjective of a comparison. Shown in Figure 31 is the simulated results of the transmission coefficient (black circle) at the resonant frequency for each vertical array size. Also shown is the peak electric field within the central vacancy at the resonance frequency (blue square). These two performance parameters give an objective performance comparison. As seen from Figure 31, at a vertical array size of 3, both the transmission through the device and the electric field within the central vacancy is quite poor, which is expected from Figure 30. The performance of the device begins to increase significantly when the vertical array size is increased, however, at a vertical array size of 11, diminishing returns are seen for both transmission and electric field strength. To reduce material costs and production time, a vertical array size of 11 is chosen without a significant loss in performance.
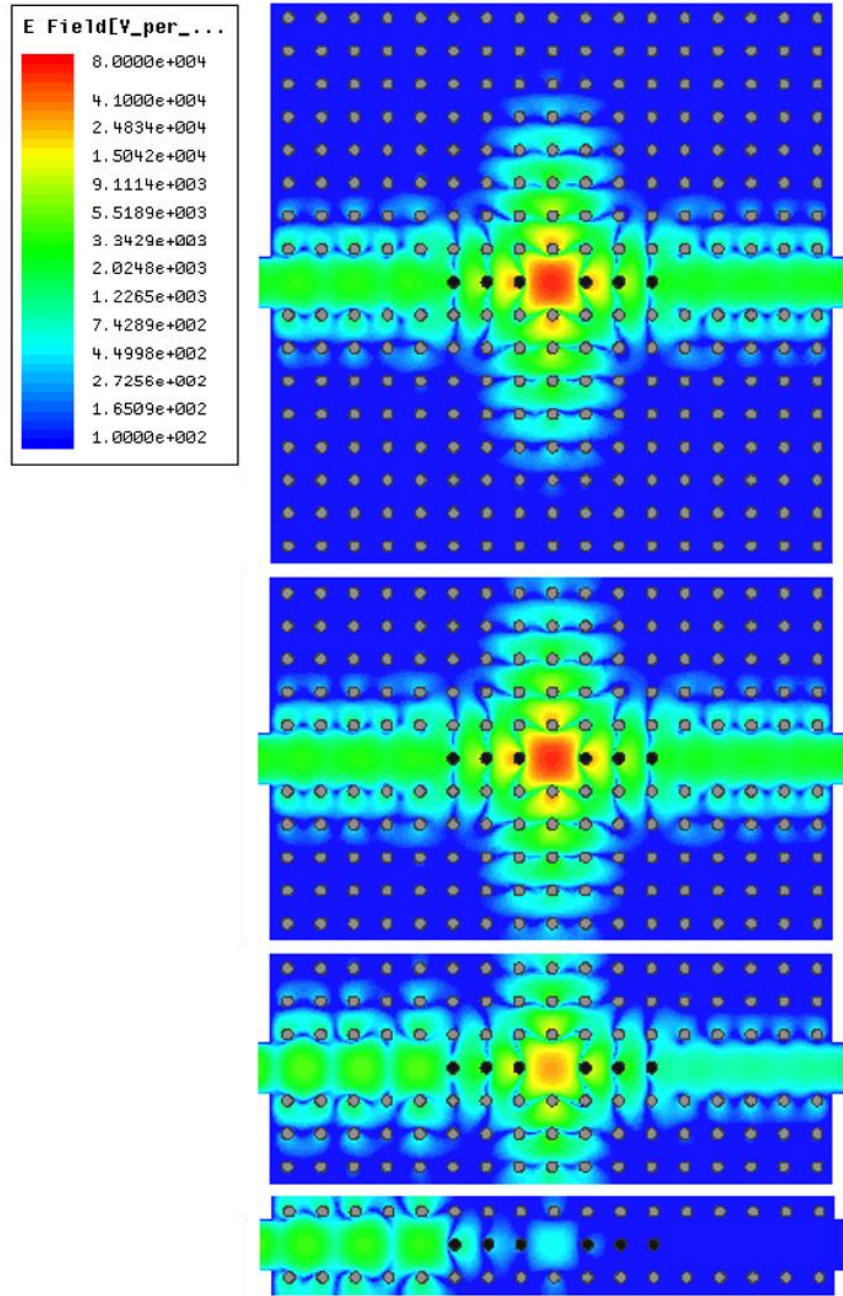
Figure 30 Simulated complex electric field amplitude within the PhC device at the resonant frequency for vertical array sizes of 17 (top), 11, 7, and 3 (bottom).
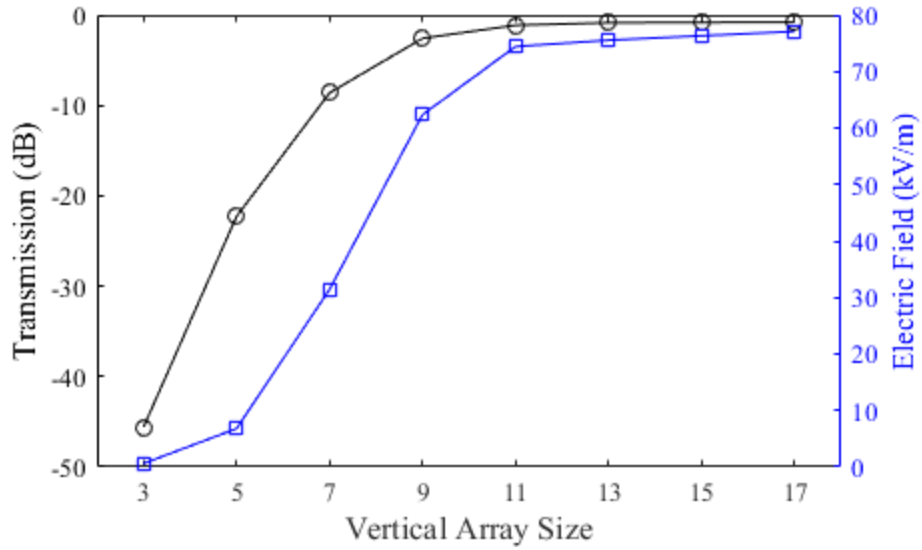
Figure 31 Simulated transmission and complex electric field magnitude at the resonance frequency for vertical array sizes of 3 to 17 rods.

An analysis of the horizontal array size was not performed due to the need for a larger channel to support the input and output method that will be discussed shortly. While the analysis was not performed for this iteration of the design, it will be performed for the 45 GHz design shown in Chapter 6.

5.1.4 Cavity Height

As mentioned earlier, a true photonic crystal array would have dielectric rods of infinite height. Since this is not realizable, a finite dielectric rod height needs to be determined. To determine the rod height, HFSS was again utilized to study the effect that the rod height has on the electric field within the resonant cavity as well as the transmission and reflection coefficients. Using the design shown in Figure 23, the rod height ($\hat{z}$ direction) was varied from 10.16 to 30 mm and resulting transmission and reflection coefficients at the resonant frequency are shown in Figure 32. The transmission coefficient is not a strong function of the dielectric

60

rod height, only varying from -0.88 dB (81.7%) at 10.16 mm to -0.3 dB (93.3) at a

rod height of 30 mm. Similarly, the reflection coefficient ranges from -20.5 dB

(0.9%) to -30 dB (0.1%). For this initial PhC device, the transmission and reflection

coefficients for any of these rod heights is acceptable and is not critically important

to the design.
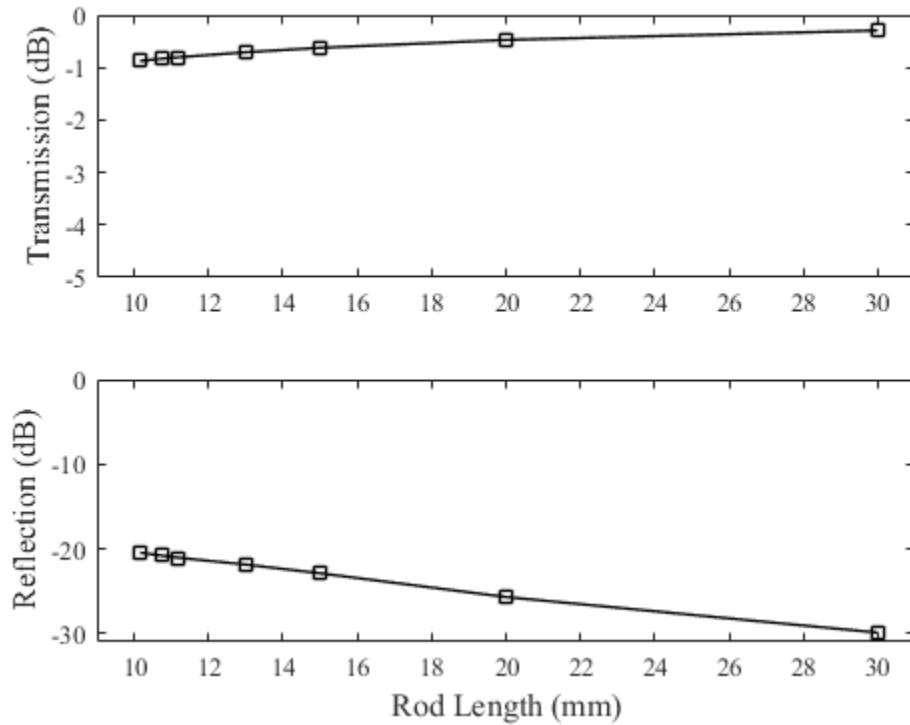
Figure 32 Transmission (top) and Reflection (bottom) coefficients at the resonant frequency as a function of the dielectric rod height.

While the transmission coefficient is not greatly affected by the dielectric

rod height, the electric field within the cavity is and is shown in Figure 33.

Lowering the dielectric rod height has the effect of concentrating the electric field

due to the existence of the conducting boundaries above and below the rods. The

61

electric field within the cavity is a strong function of the rod height and ranges from 84.4 kV/m at a rod height of 10.16 mm down to 29.3 kV/m at a rod of 30 mm.
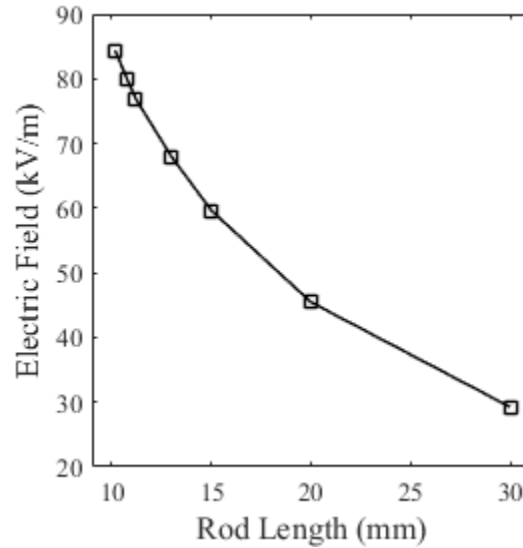
Figure 33 Peak electric field amplitude for 1 W of input power at the resonant frequency as a function of the dielectric rod height.

Given the strong dependence of the electric field on the dielectric rod height, the shortest feasible rod height should be selected if optimizing gas breakdown is desired. A rod height of 11.2 mm was chosen as a compromise between electric field strength, transmission, and construction ease. At a rod height of 11.2 mm, an electric field value of 76.9 kV/m, a transmission coefficient of -0.8 dB (83.2 %), and a reflection coefficient of -21.1 dB (0.8%) was achieved using the simplified HFSS model.

5.1.5 Input and Output Design

In the preceding sections, the input and output of electromagnetic energy to the device was accomplished using waveguide ports within HFSS, however for the

actual device, the use of waveguide ports poses two complications. First, the size of rectangular waveguide at these frequencies would require specialized vacuum feedthroughs for use with a vacuum chamber. Second, additional waveguide components would need to be purchased, which is prohibitively expensive. Another traditional method is the use of a coaxial probe placed within the waveguide channel, which is commonly employed for conventional coax to rectangular waveguide transitions. For this design, a coaxial probe is inserted into the leftmost waveguide channel approximately a half wavelength from the border of the device, with only the center conductor extending into the waveguide channel as shown in Figure 34. Applying microwave power to the coaxial input launches a vertically polarized electromagnetic wave into the waveguide channel. The wave travels in both directions of the channel, whereby the wave traveling towards the wall is reflected from the wall and constructively interferes with the forward traveling wave to produce a coherent traveling wave towards the resonant cavity. An identical coaxial probe is placed within the output waveguide cavity in exactly the same manner. When power at the resonant frequency is applied via the coaxial input, the wave travels the length of the waveguide channel is coupled into the resonant cavity, which enhances the electric field to the point of gas breakdown. Additionally, energy from the resonant cavity is coupled into the output waveguide channel whereby the output coaxial probe collects and delivers the transmitted power for quantitative measurements.
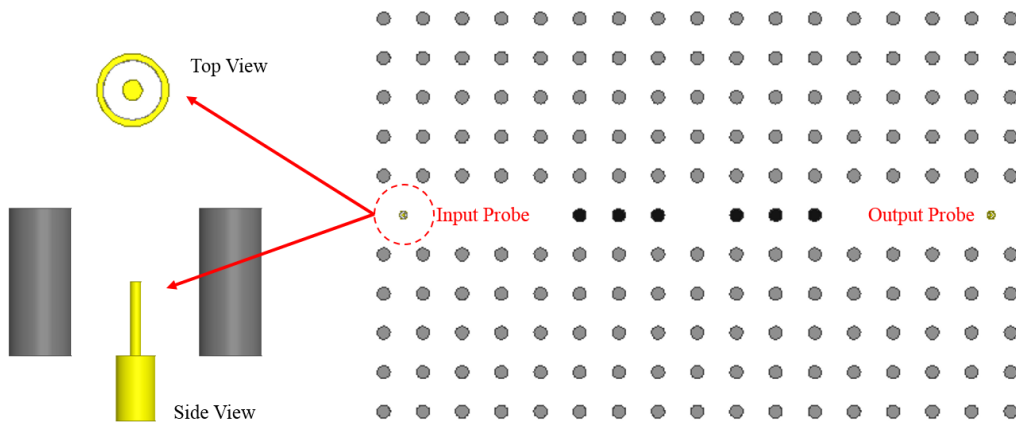
Figure 34 Coaxial input and output probes.

The decision to use coaxial inputs instead of waveguide ports did come with a small performance degradation. Figure 35 shows the resulting simulated reflection (left) and transmission (right) coefficients for waveguide ports (black dashed) and coaxial ports (blue solid). At the resonant frequency, the reflection coefficient increased from -21 dB to -8.4 dB while the transmission decreased from -0.9 dB to -2.3 dB. The 1 MHz shift in resonance frequency is likely due to simulation differences. While the performance degradation is not ideal, the performance difference was deemed acceptable given the extra cost involved in purchasing the additional test equipment needed for waveguide inputs. The increased reflection caused by the mismatch with the input coaxial probe was easily overcome by increasing the input power level.
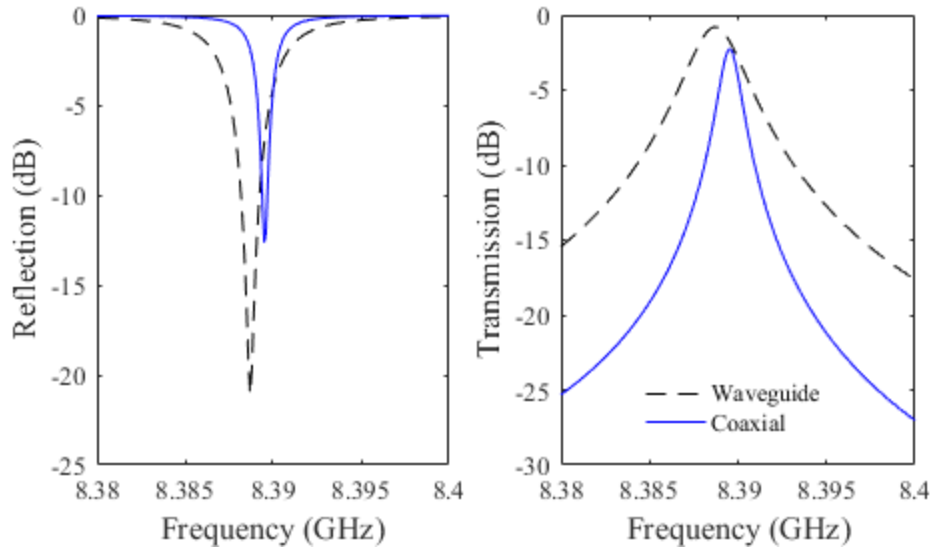
Figure 35 HFSS simulated reflection (left) and transmission (right) coefficient comparison between using a waveguide (black dashed) input/output and using coaxial probes (blue solid).

5.1.6   Final Design

The final design of the PhC device will need to implement all parameters and physical dimensions already discussed, as well as considerations for construction.   Additional construction considerations include adding perforated copper plates in order to guide and hold the dielectric rods, using enlarged holes in those plates to allow for ease of placement of the rods, and copper bars at the input and output sides of the device to set the height of the inner chamber. Additionally, a DC ignition system was originally included into the design to facilitate plasma starting, but was later deemed not necessary after the purchase of an additional high power RF amplifier. However, the hole intended for the DC ignitor in the top plate remains as part of the final constructed device.

In the simulations conducted up to this point, the dielectric rods were suspended in vacuum, however this is not physically realizable. To physically

maintain the dielectric lattice, two perforated copper guide plates (top and bottom) were employed to hold the dielectric rods in place in the lattice dimensions. The guide plates are held the proper distance apart using copper bars with a thickness of the desired resonant cavity height (dielectric rod height from above). The holes in the plates have a diameter slightly larger than that of the dielectric rods to facilitate placement of the rods. Two non-perforated copper plates then sandwich the dielectric rods and perforated copper plates to keep the rods in place in the non-lattice dimension. Finally, holes in the upper two copper plates where added for the coaxial input and output, as well as the DC starter. Figure 36 is a partial exploded view of the device showing the addition of the four copper plates as well as the two copper bars.
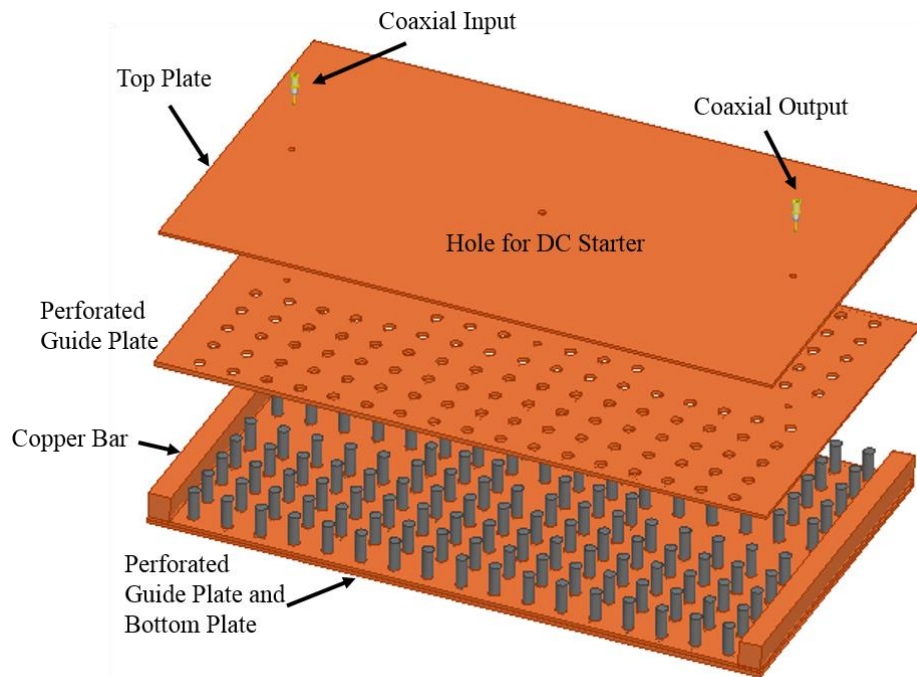
Figure 36 Final design of the PhC device including perforated guide plates, solid plates, coaxial input and outputs. Partially exploded view for clarity.

The addition of the perforated guide plates leads to a reduction in the exposed length of the dielectric rods within the device. To compensate, the dielectric rods were increased in length by 0.04 inches (copper plates are 0.02 inches each). The additional length of the rods, as well as a small vacuum between the rods and the guide plates are enough of a change to warrant additional simulations to verify performance. In addition, conductive losses are now included in the model due to the inclusion of copper material for the boundaries instead of perfect conductors. Shown in Figure 37 is the simulated transmission coefficient using the simplified design (black dashed, also shown in Figure 35 blue line) and the final design to be constructed (blue solid). Due to the added structure complexity, there is a frequency shift of ~1 % to a new resonant frequency of 8.467 GHz. The transmission coefficient dropped from -2.3 dB to -5.3 dB, this is primarily due to the added conduction losses within the copper.
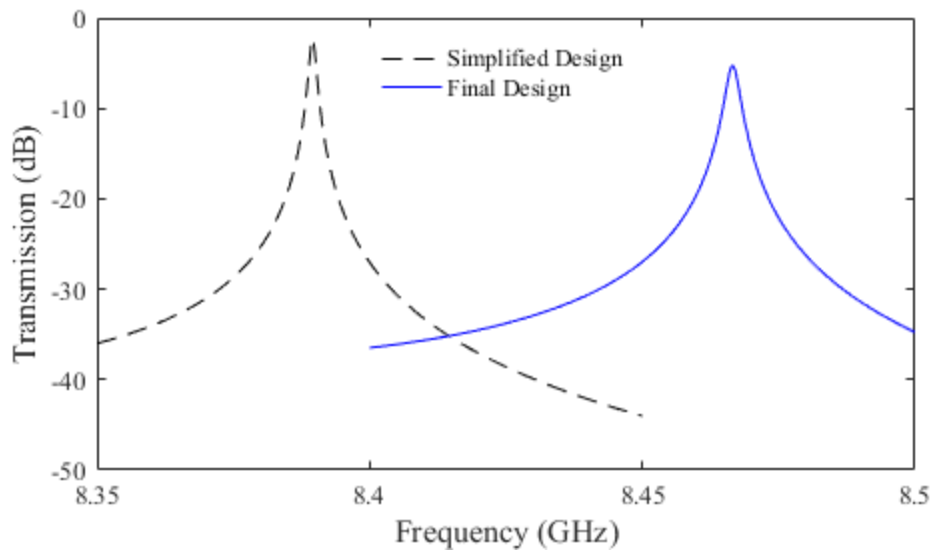
Figure 37 Comparison of the transmission coefficient between the simplified (black dashed) HFSS model and the final (blue solid) HFSS model for construction.

67

In addition to changes in the transmission coefficient of the device, the increase in conductive losses and structure complexity leads to a drop of the electric field within the resonant cavity. Shown in Figure 38 is the electric field amplitude of the simulated final design. For 1 W of input power, the simulated electric field within the central vacancy reaches a value of ~65 kW/m, down from 76.9 kV/m prior to the final design additions. While lower, an electric field magnitude of 65 kV/m per Watt will be sufficient for plasma ignition.
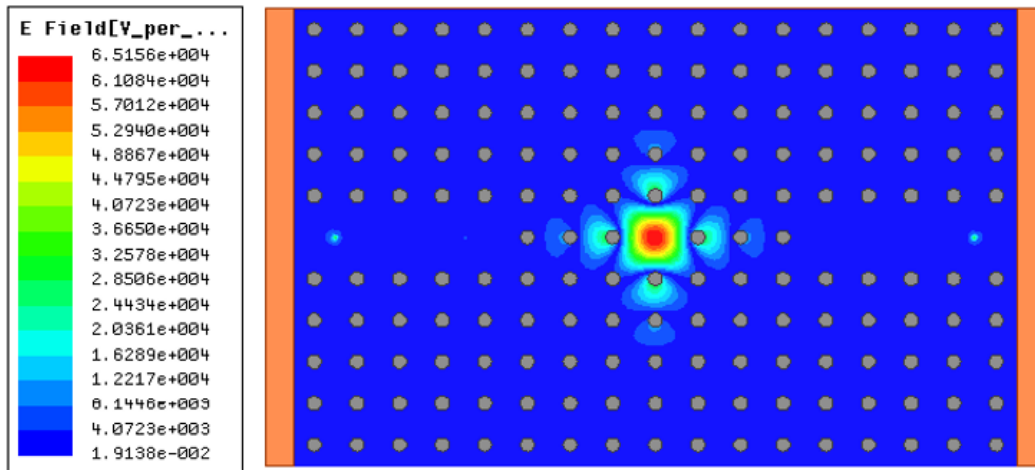
Figure 38 Simulated electric field amplitude of the final design of the PhC device showing a peak electric field magnitude within the resonant cavity of ~65 kV/m for a 1 W input.

The fully constructed device is shown in Figure 39. For assembly, six screws on the top and six screws on the bottom are added to secure the copper plates to the copper bars. Additionally, copper blocks were soldered to the top plate to hold the coax input and output securely in place. The addition of these elements should have no effect on the performance of the system and were not included in the HFSS model.
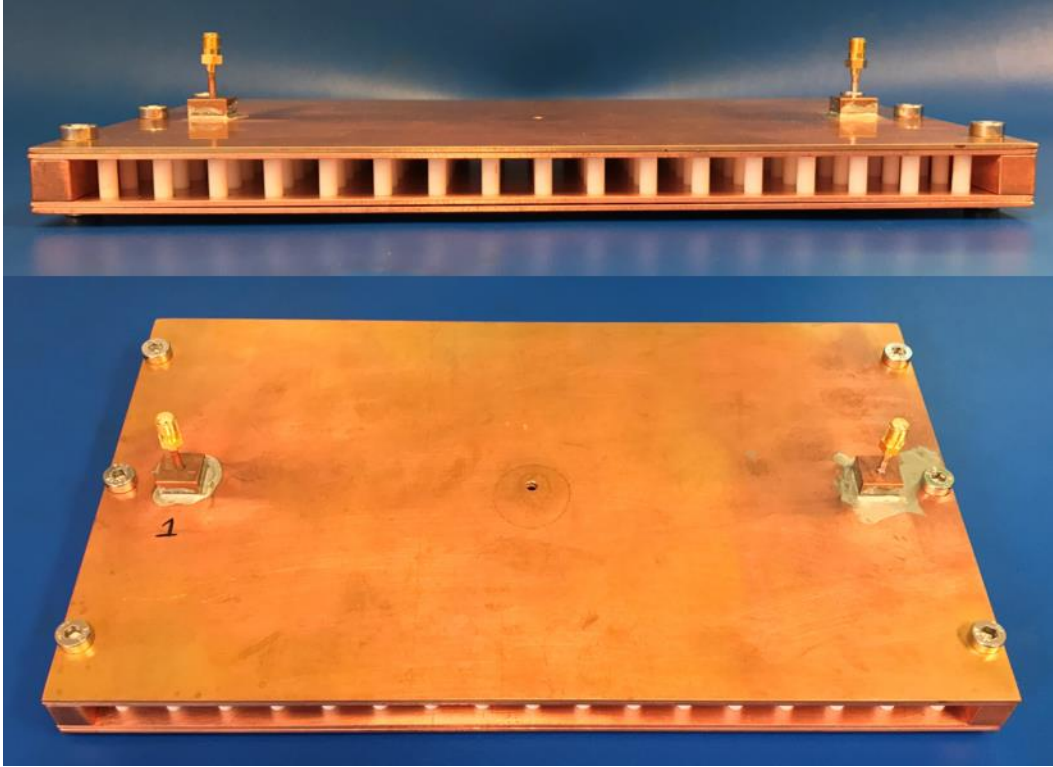
Figure 39 Side (top) and top (bottom) view of the fully constructed device.

5.2   Experimental Setup

As illustrated in Figure 40, the photonic crystal device is placed inside a vacuum chamber for experimentation. The chamber is initially pumped to a base pressure of 10 mTorr and then backfilled with argon to the desired pressure, which was measured using a Granville-Phillips 475 Convectron gauge which was calibrated for argon. Microwave power is delivered to the device through a coaxial vacuum feedthrough with SMA connection. Inside the vacuum chamber, a SMA cable connects the feedthrough to the device input while a second SMA cable connects the PhC device output to a second vacuum feedthrough.
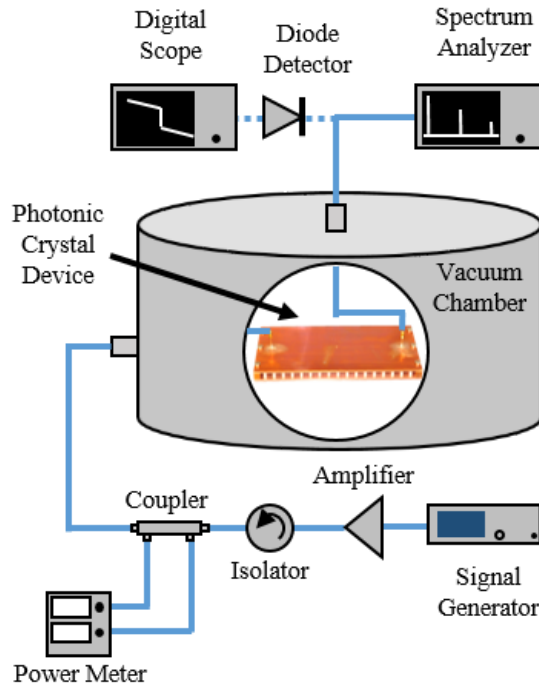
Figure 40 Experimental setup for determining transmission loss of the device both with and without plasma present. The dashed line represents the alternate connections made for measurement of plasma transient effects.

Microwave power is supplied at the desired frequency by a Keysight N5183A Analog Signal Generator with amplification provided by a TriQuint RM022020 benchtop power amplifier (2-20 GHz, 20 W). A Pasternack PE83IR1010 (8-18 GHz, 50 W) isolator is connected to the output of the amplifier for protection from potentially damaging reflections from the plasma-filled defect. A Pasternack PE2223-20 dual directional coupler (8-16 GHz, 50 Watts) is connected inline between the isolator and the vacuum chamber in order to sample the forward and reflected power to the device. Power is sensed from the ports of the directional coupler using two Keysight N8487A power sensors connected to a Keysight E4417A power meter. Losses for all cables, coaxial feedthroughs, and

directional coupler ports were measured, and corrections were applied to all reported power measurements.

Output power from the PhC device is channeled through SMA cables to a SMA vacuum feedthrough and is measured for steady state power and for transient behavior. For experiments involving the measurement of steady state power, a Keysight E4407B spectrum analyzer is connected to the vacuum feedthrough via an SMA cable and measures both power and frequency content of the PhC output. A spectrum analyzer was chosen instead of a power meter in order to measure any harmonic content being produced by the plasma. As with the input power, the output power measurements were corrected for cable and feedthrough losses and all reported power measurements have corrections applied.

To measure the transient behavior of the PhC device and the plasma development, an alternate measurement method was needed. For these measurements, the spectrum analyzer is replaced with a diode detector (Fairview Microwave, Model SMD0208, C_o=20 pF) that converts the output power of the PhC device into a voltage. The detected voltage represents the transient power transmission through the PhC and is recorded using a Tektronix TDS 2022B digital oscilloscope with a 50Ω termination. Calibration of the diode voltage was accomplished by connecting the diode detector to the output of the PhC device and measuring the resulting voltage for a wide range of input powers. Next, the diode detector was replaced with the spectrum analyzer and the output power of the device was directly measured for the same range of the input powers. Voltage

versus input power and output power versus input power curves where then compared to produce an appropriate voltage to power conversion.

In order to ensure that the diode detector did not affect the measurement of the plasma transient, the diode detector response time was measured. This was accomplished by connecting a pulsed signal generator to the input of the photonic crystal and measuring the rise time of the output pulse using the diode detector. The response time of diode detector was determined to be ~65 ns, which is faster than the expected transient time of the plasma (> 100 ns).

5.3   *Experimental Results*

In this section I report the steady state and breakdown characteristics of the plasma within the PhC device. All experiments were conducted using argon gas, so the primary experimental parameters affecting the plasma characteristics are input power and gas pressure. The first experiment conducted was a survey of harmonic power production. Next, experiments measuring the plasma ignition power and minimum power to sustain a plasma serve to establish the operating boundaries of the PhC device. The next experiments will measure the output power and transmission rate of the PhC while a steady state plasma is maintained. Finally, time domain measurements were conducted to measure the transient response of the output power of the device as a plasma forms as well as a measurement of the plasma formation time.

Before experiments can be conducted, a verification of device operation was first conducted. Figure 41 compares the measured experimental transmission

72

coefficient with the 3D electromagnetic solution using HFSS. The experimental transmission coefficient shows a resonant frequency of 8.614 GHz, which is a +1.7% shift from the simulated design. In addition, the experimental transmission coefficient at the resonant frequency is lower than that of the simulation, -7.3 dB versus the simulated value of -5.3 dB. Differences in resonant frequency and transmission coefficient are due primarily to uncertainty in the permittivity of the dielectric rods, dimensional tolerances, and additional material losses not accounted for in the HFSS model.
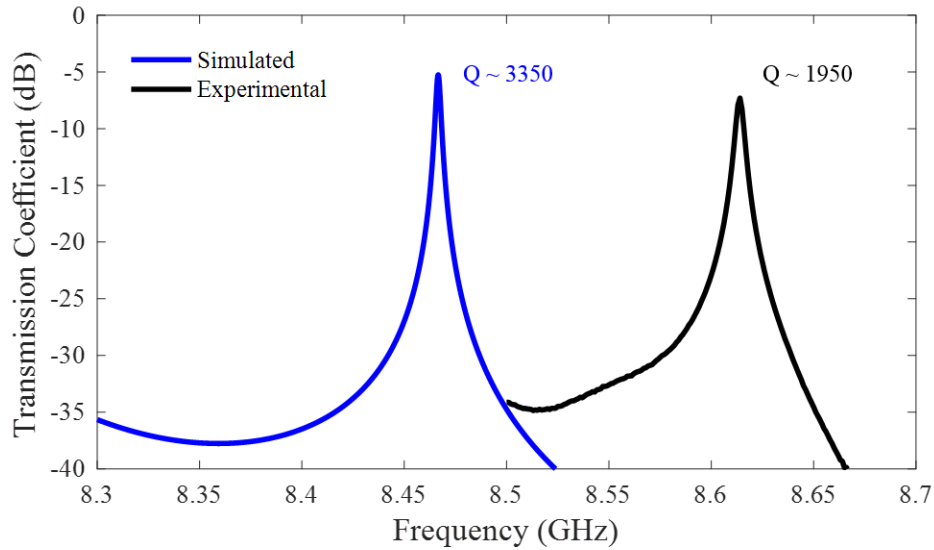
Figure 41 Transmission coefficient (S_{21}) of the PhC device without plasma. Simulation using HFSS (blue); Experimental (black).

To verify a plasma is able to be produced by the PhC device, RF power at the resonant frequency of 8.614 GHz was applied to the device input. Figure 42 shows a side view of the PhC device without (top) and with (bottom) plasma. When sufficient power is applied at the resonant frequency, a plasma forms in free space within the cavity and does not contact the dielectric lattice.

73
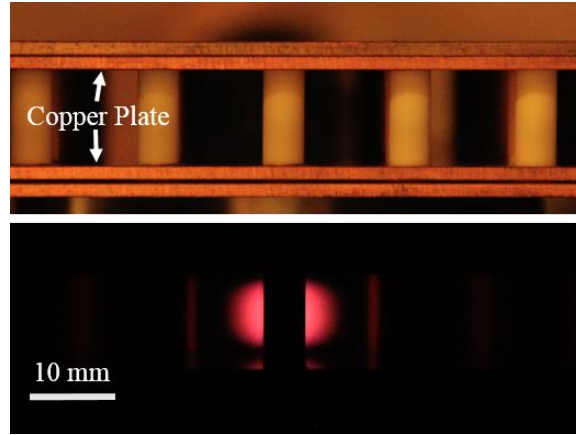
Figure 42 (Top) Side view of photonic crystal device prior to gas breakdown. (Bottom) Side view of photonic crystal with 10 Torr argon plasma with 0.78 Watts input power. The plasma image is partially obscured due to the presence of dielectric rods

The formation and sustainment of a plasma within the central cavity alters the transmission properties of the PhC device. Shown in Figure 43 is the transmission coefficient of the PhC device prior to plasma formation (black line) and with a 10 Torr, 780 mW input power plasma present within the central cavity of the device (blue dots). At the resonant frequency of 8.614 GHz, the transmission coefficient is reduced from -7.3 dB to -17.3 dB, a 10 dB reduction. To measure the transmission coefficient with a sustained plasma, the plasma was first ignited at the resonant frequency and the frequency was increased while measuring both the input and output powers of the device. Subsequently, the frequency was then lowered, again measuring input and output power. At frequencies lower than the resonant frequency, the plasma begins to fade resulting in a small increase in the transmission coefficient as compared to frequencies above resonance. At frequencies below 8.61 GHz, the plasma is extinguished which results in the transmission coefficient following the no plasma case.
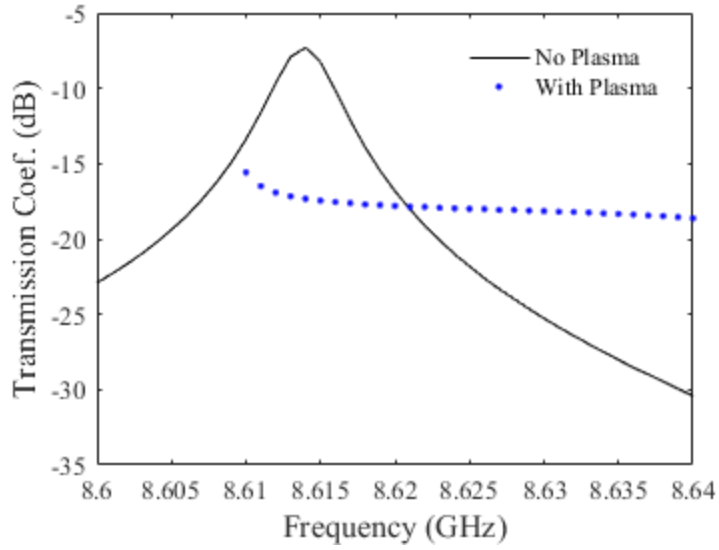
Figure 43 Transmission coefficient of the PhC device with no plasma present (black) and with a plasma sustained at 10 Torr and 780 mW of input power (blue dot). For the with plasma case, the plasma is maintained for frequencies greater than 8.609 GHz.

5.3.1 Harmonic Production

Plasmas have well established non-linear electrical properties and the production of harmonic frequencies are expected. In the pressure range of interest (5 – 60 Torr), and for a symmetric electrodeless discharge at low power (< 10 W), harmonic generation by the plasma is expected to be small [91]. Prior to the measurement of harmonics produced by the plasma, the harmonic content of the measurement apparatus system must first be characterized. RF power at the resonant frequency (8.614 GHz) of the PhC device was applied and the frequency spectrum of the output power was measured using the spectrum analyzer. Input power of 9 W was applied at atmospheric pressure to prevent plasma formation and the frequency spectrum was measured and the results are shown in the top left of Figure 44 (black). Output power was measured to be 21.4 dBm at the fundamental (top right), -31.7 dBm and the second harmonic frequency (bottom left), and -33.5

75

dBm at the third harmonic frequency (bottom right). The power measured at the third harmonic is at the noise floor of the spectrum analyzer and is not an actual measurement of harmonic power. Without a plasma present within the device, the second harmonic power measured was solely produced by the power amplifier and not by the PhC device.
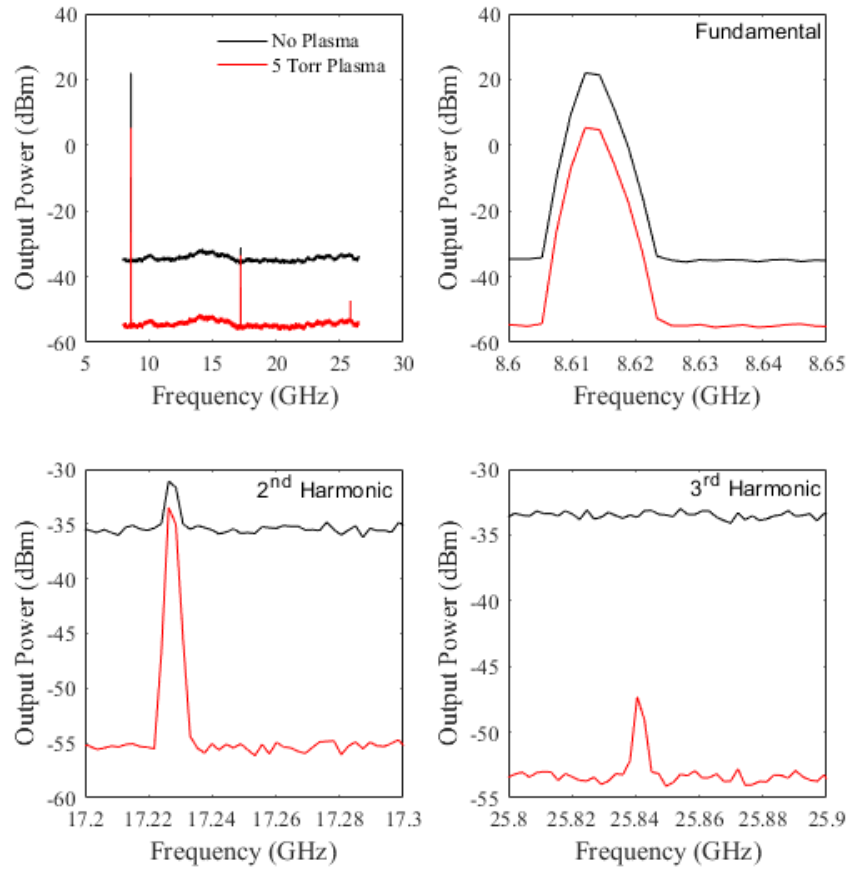
Figure 44 Output power frequency spectrum of the PhC device with 9 W of input power and no plasma present (black) and after plasma ignition in 5 Torr of argon. Top left shows full spectrum while remaining plots show zoomed in view of the fundamental, 2nd harmonic, and 3rd harmonic frequencies.

Now that the baseline harmonic production of the measurement apparatus has been established, the effect of plasma on harmonic production can be measured.

Applying 9W of input power to the device in 5 Torr of argon now ignites a plasma. Using the spectrum analyzer, output power at the fundamental frequency was found to be 4.7 dBm, which is 16.7 dB lower (~98%) than the baseline no plasma measurement. A significant reduction of output power at the fundamental is expected due to the presence of the plasma and will be explained in detail in a subsequent section. Second harmonic power was measured to be -33.5 dBm, 2.4 dB lower than the no plasma case, and -38.2 dBc (dB relative to power at the fundamental frequency, 0.015%). Second harmonic power of the amplifier for the no plasma case was -54.9 dBc (0.0003%). Third harmonic power was found to be -47.3 dBm, or 52 dBc (0.0006%). A comparison of third harmonic power production is not possible due to the high noise floor of the no plasma condition. While there is a significant increase in the second harmonic power relative to the fundamental, harmonic production is still very small under the most favorable conditions of low pressure and high power. Harmonic production from a plasma tends to decrease at higher pressures and with lower power. Given the relatively low amount of harmonic production, the remainder of this work will focus solely on the fundamental frequency.

5.3.2   Minimum Ignition Power

Prior to plasma formation, the PhC device operates as a high Q resonator with output characteristics similar to that of a narrow bandpass filter. However, once breakdown occurs within the resonant cavity, the characteristics of the PhC device are altered. The minimum input power required to begin gas breakdown is

a function of gas pressure and the experimental results are shown in Figure 45. While operating at the device resonant frequency of 8.614 GHz, the input power to the device was gradually increased until such a time as a plasma was visually observed to ignite. This was repeated ten times at each pressure value with the error bars in Figure 45 representing the range of observed ignition powers. At gas pressures below 5 Torr and above 60 Torr, a plasma could not be ignited given the limited amplifier power available and measurement system losses. Microwave breakdown in this device resembles that of a Paschen curve with a minimum occurring at 10 Torr of argon with an input power of 1.4 W. However, unlike a Paschen curve, this minimum coincides with the condition that the electron collision frequency is equal to that of the applied microwave frequency in radians, $\nu_m \sim \omega = 5.4 \cdot 10^{10}$ rad/sec [11].
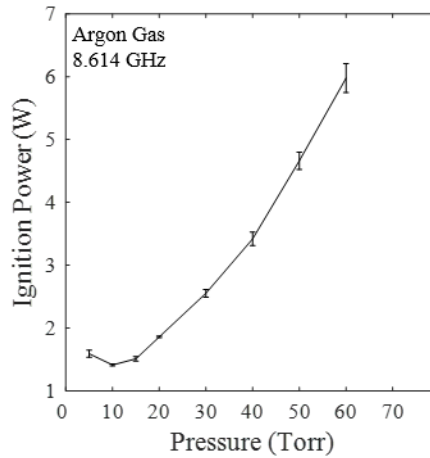
Figure 45 Minimum input power at the resonant frequency required to ignite a plasma in argon within the PhC device as a function of gas pressure.

5.3.3 Minimum Sustainment Power

During steady-state plasma operation, the PhC device is able to sustain the plasma at power levels well below that of the required power for ignition. The minimum input power level required to sustain the plasma is a function of gas pressure and is shown in Figure 46. For this experiment, the plasma was first ignited at the resonant frequency and subsequently the input power was reduced until the plasma was observed to be extinguished. This was repeated ten times at each pressure and error bars in Figure 46 represent the range of observed values. A broad minimum in the sustaining power occurs at 20 Torr, with only 87 mW of input power required for plasma sustainment. Also shown in Figure 46 is the minimum power absorbed by the plasma under the same conditions. Absorbed power is defined as the input power to the device minus the reflected and output powers, $P_{abs} = P_{in} - P_r - P_{out}$. While this does not account for losses within the device itself, such as conduction and dielectric losses, it is a good first order approximation for the power being absorbed by the plasma. At 10 Torr, 44 mW of absorbed power is required to sustain the plasma while at 20 Torr, 40 mW is required. Since the required power to sustain the plasma is much lower than that of plasma ignition, the device is able to operate in the presence of a wide range of post-breakdown input power variations.
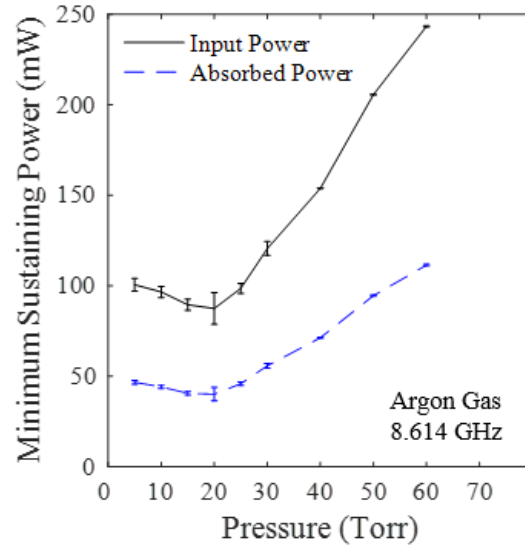
Figure 46 Minimum input power (black) and absorbed power (blue dashed) required at the resonant frequency to sustain a plasma in argon within the PhC device as a function of gas pressure.

5.3.4 Effect of Plasma Ignition on Output Power

Without a plasma present, the output power of the PhC device is linear with input power, which gives the device a constant transmission coefficient as expected. However, once the input power to the device crosses the threshold for plasma ignition, the reflected power from the input port of the device is significantly increased due the perturbation of the PhC defect by the plasma. Additionally, input power to the device is also absorbed by the plasma. The emergence of these two power divergence paths results in a severely dampened output power. Figure 47 shows the relationship between input and output power of the PhC device for the 10 and 50 Torr cases. Input power at the resonant frequency is swept from ~50 mW to ~9 W and the output power is recorded. Prior to plasma ignition, the output power linearly increases with input power. Once the plasma ignites, the output power is significantly reduced. Increasing the input power beyond the point of

80

plasma ignition (arrows in figure) further decreases the output power, which gives the input/output power relationship a slightly negative slope when a plasma is present. Post plasma ignition, the power limiting function of the device is also maintained for input powers down to the minimum sustaining power (see Figure 46). The curves in Figure 47 would show hysteresis, but data going below ignition power were omitted to improve clarity of the figure.
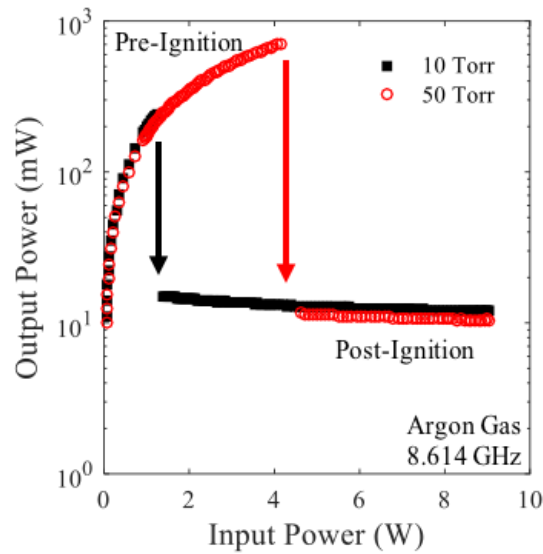
Figure 47 Output power versus input power at the resonant frequency for the PhC device in 10 (black) and 50 Torr (red) of argon. Arrows are located at the point of plasma ignition.

5.3.5 Effect of Plasma on Transmission Coefficient

Under steady-state no plasma conditions, the device operates as a narrowband filter with a constant transmission coefficient at the resonant frequency of approximately -7 dB. With a plasma present within the device, the transmission characteristics are altered by the plasma and becomes a function of input power and

gas pressure. The transmission coefficient for the no plasma case, as well as for a plasma operating in 10 Torr and 50 Torr of argon is shown in Figure 48 (left) and as a function of pressure and power (right). For this experiment, the transmission coefficient was measured at the resonant frequency of 8.614 GHz for various input power levels and pressures. Without the presence of a plasma, the transmission characteristics of the PhC device is not altered by either the input power level or gas pressure. With a plasma, the transmission characteristics of the device are a weak function of gas pressure, only varying about 2 dB between the low pressure case of 10 Torr and the high pressure case of 50 Torr. Transmission is, however, a strong function of input power to the device, ranging from ~ -17 dB at low power to ~ -27 dB at higher power. The increase in input power increases the plasma density and this in turn, increases the attenuation of the device due to the plasma. With the plasma present, the increasing attenuation with increasing input power allows the device to maintain a nearly constant output power regardless of the input power as shown in Figure 47. The function of a power limiter is not unique to this PhC design, commercial gas discharge tubes placed in conventional cavities have also been shown to perform an equivalent function [92].
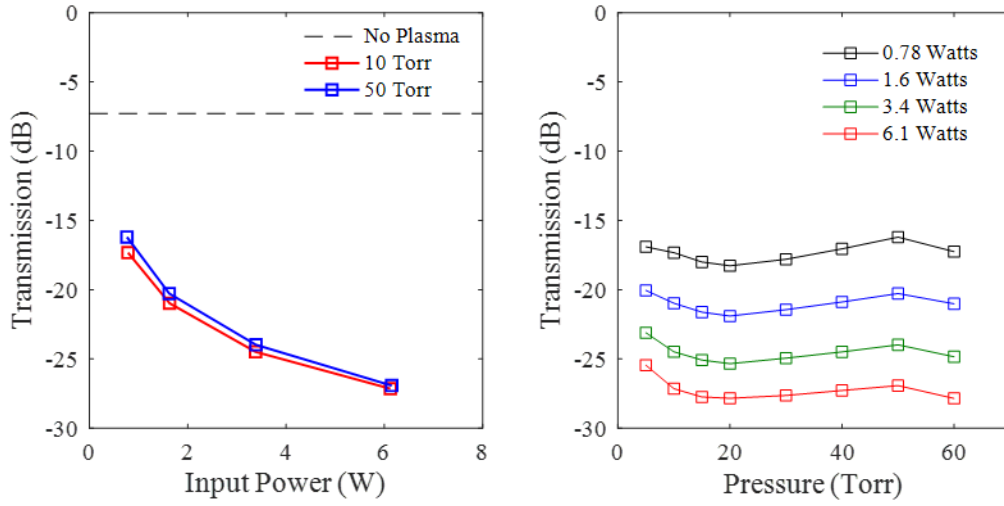
Figure 48 (Left) Steady-state transmission through the PhC device at the resonant frequency as a function of input power with no plasma present (black dashed), with plasma present at 10 Torr (red square) and 50 Torr (blue diamond). (Right) Steady-state transmission versus pressure for input powers between 0.78 and 6.1 Watts.

5.3.6   Effect of Plasma on Power Distribution

As mentioned previously, once the plasma is ignited, the distribution of power is altered. Figure 49 shows the partitioning of power of the PhC device due to the presence of a plasma within the resonant cavity for an input power of 9 W and for argon pressures ranging from 5 Torr to 60 Torr. While a plasma is maintained, the input power is primarily reflected to the input port of the device with a smaller portion being absorbed by the plasma itself and is not greatly affected by the change in argon gas pressure. For a 9 W input power, approximately 7 W are reflected to the input port, ~ 2 W are absorbed by the plasma, and only 12 mW are transmitted through to the output port.
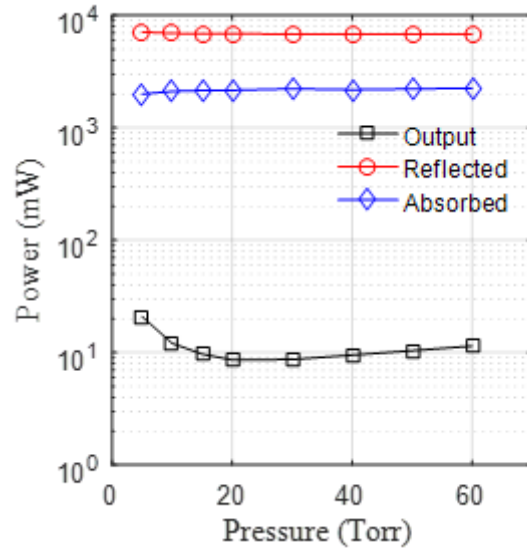
Figure 49 Partitioning of input power post-plasma ignition. Output (black), reflected (red), and absorbed (blue) power by the device for 9W of input power at the resonant frequency as a function of gas pressure.

5.3.7   Transient Response

The transient response of the PhC device during the interval when the plasma forms within the cavity vacancy is an important metric in determining the device's performance and is investigated next. The plasma formation time is not instantaneous and depends on the input power to the device and the gas pressure within the cavity. As described in Ref. [93], there are two components that effect the time delay between the first application of microwave power to the formation of the plasma discharge. First, the statistical delay time until the avalanche inducing seed electron first appears, and second, the formation time of the avalanche itself. For a PhC cavity, as well as other resonant cavities, there is also a third delay time during which the electric field rings-up from the incoming wave energy. For an instantaneous incident pulse, the field builds within the cavity on a time scale of $\tau_{\text{cavity}} \sim Q/f_c = 1950/8.614$ GHz $= 230$ *ns* [11]. Experimentally, the signal generator

produces a ramped output power with a rise time of ~20 μs. Therefore, the cavity ring-up time reported in the model is too short to be observed in this experiment.

The plasma formation time is measured via the indirect method of observing the time evolution of the PhC device output power. Once microwave power is applied, the output power of the device is observed until a steady state plasma is formed. Observations of the plasma formation time for a 10 Torr argon plasma for various input power levels are shown in Figure 50. For these measurements, t = 0 represents the point at which the output power begins to be attenuated, which occurs at the onset of plasma formation. At t < 0, the output power is ramped up according to the ramp-up time of the signal generator (20 μs) with a small effect from the ring-up of the resonant cavity (0.2 μs). At t > 0, the output power is quickly attenuated to near the steady-state value, at which point the output power slowly decreases until the steady-state power level is reached. It should be noted that the onset of plasma ignition occurs at the same input power level per the minimum ignition data shown in Figure 45. The output power shown in Figure 50 differs due to the increasing input power level of the ramped input.
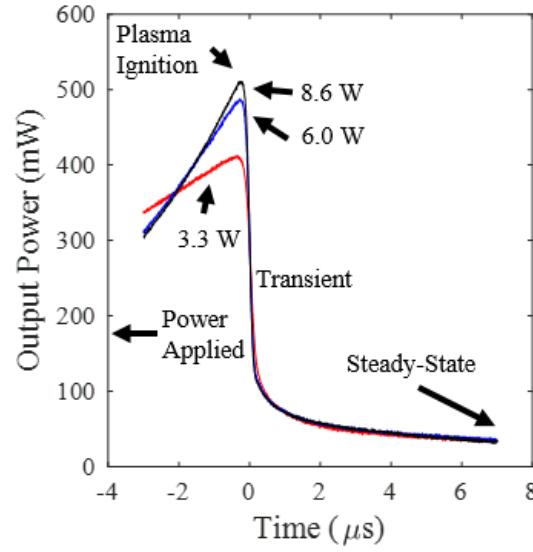
Figure 50 Transient output power during plasma formation for a 10 Torr argon plasma at the resonant frequency and for 3.3 W (red), 6.0 W (blue), and 8.6 W (black) of input power.

At the onset of avalanche breakdown within the PhC cavity the electron density within the cavity increases rapidly, both absorbing incoming wave energy and increasingly reflecting the incident wave energy as suggested by Figure 49. At the highest input power shown in Figure 50 of 8.6 W, approximately 500 mW of output power is reached before avalanche breakdown begins and rapid attenuation of the output power begins. Using the no plasma transmission coefficient of -7 dB and the observed output power, the input power at the cavity is approximated to be only 2.1 W, 2.4 W, and 2.5 W at the onset of breakdown for the steady-state input power conditions of 3.3 W, 6.0 W, and 8.6 W. The difference in input power required for the onset of breakdown is due to the statistical delay competing with the ramp-up times of the cavity and the signal generator, given enough time, plasma ignition should begin at a consistent input power level as shown in Figure 45.

At approximately 10 µs after the onset of breakdown, the output power of the PhC device is reduced to ~10 mW as shown in both Figure 47 and Figure 49. The output power during the transient plasma formation period (Figure 50) shows two distinct phases as predicted by the 2-D model from Ref. [11]. The first phase is characterized by an exponential increase in electron density of the cavity and a rapid decrease in the transmission of power through to the output of the device and occurs during the initial plasma formation period ($t < 0.2$ µs). The 2-D model suggest that the initial plasma is centered with the cavity and has a size which is much smaller than the lattice constant of the PhC device [11]. The second, much slower phase is the result of plasma expansion ($0.2 < t < 10$ µs) as the plasma discharge volume grows to occupy a significant portion of the cavity. A depiction of the plasma volume for the two growth phases from the 2-D model is shown in Figure 51 and a photo of the experimental steady state volume is shown in Figure 42 (bottom).
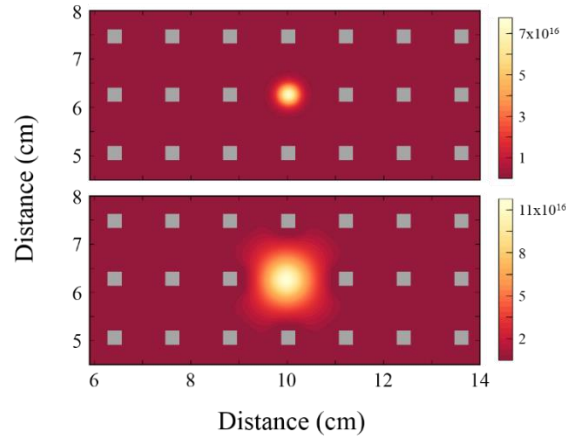
Figure 51 Spatial profiles of the electron density (m^{-3}) for t = 0.1 µs (top), and t = 1 ms corresponding to steady state (bottom) [11].

To quantify the formation time of the plasma for various conditions a new parameter is needed. From Figure 50, the plasma formation time is approximately exponential, we can define a time constant that is the time required for the output power to be reduced to $1/e$ (~37%) of the difference between the output power at the onset of plasma ignition and the steady-state output power level. A summary of the calculated time constants for a wide range of argon pressures and input power levels is shown in Figure 52. For these calculations, the output time response was first de-convolved from the time response of the diode detector. From Figure 52, the plasma formation time constant is dependent on both gas pressure and the input power level. At the lowest pressure of 5 Torr, the time constant ranges from ~200 ns at low input power to ~ 100 ns at the highest power examined. At the highest pressure tested of 60 Torr, the time constant ranges from ~ 3 μs at the lowest input power down to ~ 1.5 μs at the highest power examined.
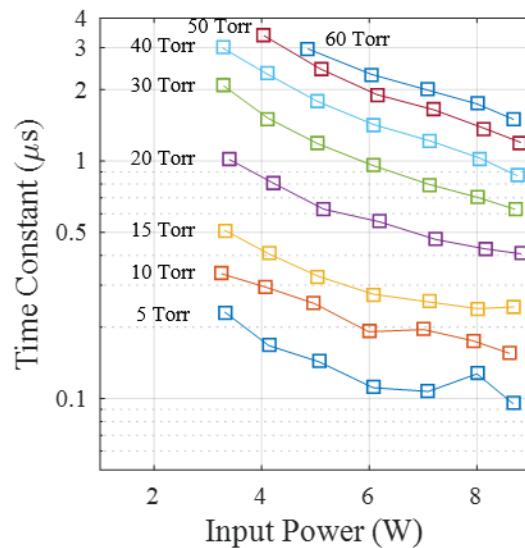
Figure 52 Transient plasma formation time for argon plasma ignition at the resonant frequency and for various argon pressures and input power levels.

88

5.4 Steady-State Electron Density Measurements

The electron density of the plasma is an important parameter in understanding the plasmas behavior. However, diagnostic techniques for determining electron density within the PhC cavity are limited. Conventional methods for measuring the electron density include Langmuir probes, Stark broadening, and the cavity perturbation method [94, 95, 96]. Collisional ion transport to a Langmuir probe in high pressure argon causes uncertainty in the interpretation of Langmuir probe data [96]. In addition, we find that inserting a probe into the PhC cavity would disturb the resonance of the cavity to an extent that makes the measurement unreliable. Typically, Stark broadening requires electron densities greater than 10^{20} m^{-3} [95], but modeling in Figure 51 suggests this device produces electron densities on the order of 10^{17} m^{-3}, so the electron density cannot be measured spectroscopically with sufficient accuracy. Finally, the perturbation method requires that the plasma volume be only a small fraction of the cavity volume [94]. Experiments show that the plasma volume for this PhC device is on the order of 50% of the cavity volume, which violates the requirement for the perturbation method. Given constraints of the typical electron density measurements, an alternate method involving both experimental measurements of the transmission coefficient and 3D electromagnetic simulations was developed to estimate the electron density and is outlined in the following paragraphs. In essence, we seek to compare experimental results of the change in attenuation of

electromagnetic energy through the device due to the presence of the plasma with the simulated change in attenuation due to a plasma volume modeled within HFSS.

The transmission coefficient of the plasma-loaded PhC is easily measured, and is a function of both the physical size and effective complex permittivity of the plasma [97]. If the electron collision frequency is known, the complex permittivity yields the electron density. Experimentally, the size of the plasma is determined by taking a photograph of the plasma at each pressure and input power of interest. However, from Figure 42, the dielectric rods of the PhC lattice obscure the view of the center of the plasma, and therefore the peak emission intensity must be determined using a fitting method. From the 2-D model of Ref. [11] and as shown in Figure 53, the spatial profile of the electron density was determined to be well-approximated by a Gaussian curve. Assuming that the emission intensity of the plasma is proportional to the electron density, a spatial profile of the plasma size can be estimated using a Gaussian fit of light intensity of the plasma and will be discussed further in the following paragraphs.
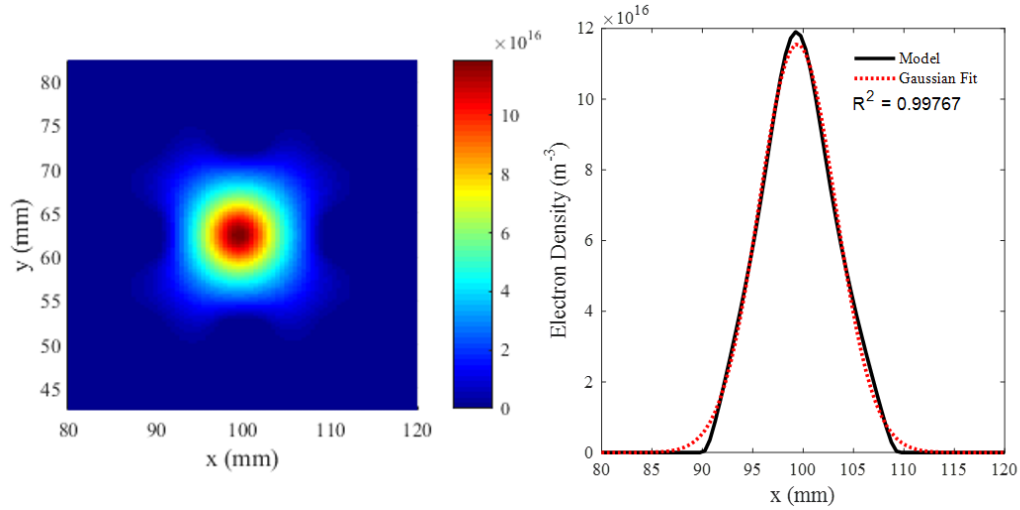
Figure 53 (Left) Spatial profile of the electron density from 2-D model [11]. (Right) Gaussian fit of the electron density along center of plasma (y=62 mm) in x direction.

To estimate the size of the plasma, a photograph is taken of the device with a plasma present and imported into Matlab. The image is then converted into grayscale so that the image is represented as an array with each pixel having a value from 0 to 255. Figure 54(a) shows the resulting image for a 10 Torr argon plasma with 0.78 W of input power applied at the resonant frequency. For averaging purposes, the array is reduced such that only a small vertical section centered at the center of the plasma remains and is depicted by the red box in Figure 54(a). The array is further reduced into one dimension by summing the pixel values vertically. The resulting one-dimensional array is plotted with the blue line in Figure 54(b). As you can see from the figure, the light intensity at the center is obscured, and results in a zero sum in the center with two light peaks at the edges of the dielectric rod. The leading edge of the left peak, and trailing edge of the right peak (shown in black) are then utilized for the Gaussian fit. The selected data is then fitted using a Gaussian model and normalized, the resulting fit is the red line Figure 54(c). The

91

measured data is then normalized and plotted in black to ensure a proper fit was done. This method yields the hidden peak emission intensity and the mean value of the light intensity. An average plasma size was determined using the length of the emission between the mean value of the Gaussian on the leading and trailing side of the plasma emission as shown in purple in Figure 54(c). This procedure is repeated for all pressure and power levels of interest.
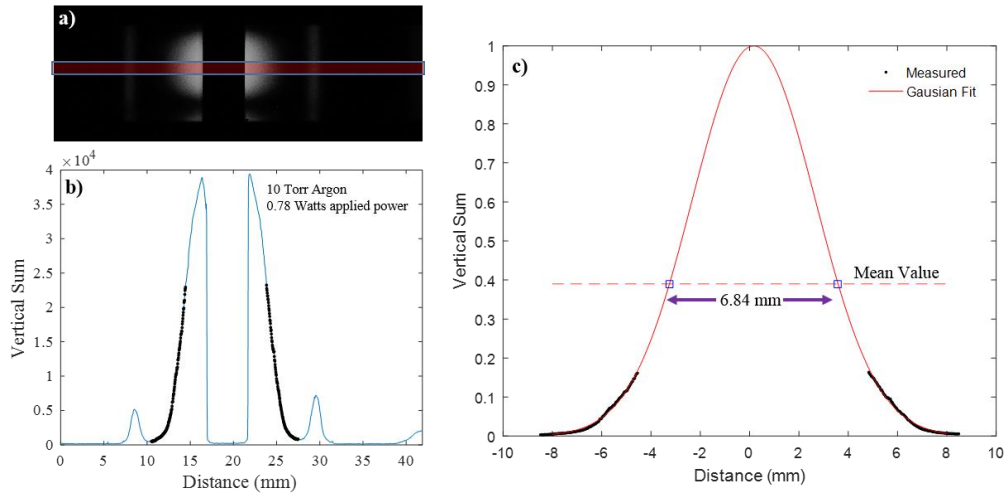
Figure 54 (a) Photo of PhC device with a 10 Torr argon plasma with 0.78 W of input power applied, red box indicates pixels to be summed. (b) Vertical sum of the pixel values from the area represented by the red box in a), data selected to perform Gaussian fit shown in black (c) resulting normalized Gaussian fit of the summed light intensity in red, data selected for the fit is shown in black, distance between the two mean values is shown in purple.

Simulation of the plasma's effect on transmission is accomplished using a uniform plasma model within HFSS. Using the average size of the plasma found experimentally, a dielectric volume in the shape of an ellipsoid is placed at the center of the cavity as seen in Figure 55. The ellipsoids major diameter (in plane) is set to the experimentally derived average plasma size for the pressure and input power condition of interest, while the minor diameter is given by the height of the cavity. To mimic the dielectric properties of the plasma, a custom material is

92

created within HFSS using frequency dependent parameters of electron density (n_e), real permittivity (ε_p), and dielectric loss tangent $(tan\ \delta)$. These properties were given section 3.2 and repeated here;

$$Re(\varepsilon_p) = \varepsilon_0\left[1 - \frac{e^2 n_e}{\varepsilon_0 m_e(\omega^2 + \nu_m{}^2)}\right]$$

$$\tan\delta = \frac{\nu_m e^2 n_e}{\omega\varepsilon_0 m_e}\left(\frac{1}{\omega^2 + \nu_m{}^2 - \omega_{pe}{}^2}\right),$$

where ω and ω_{pe} are the microwave operating frequency and electron plasma frequency in rad-s^{-1}, ν_m is the collision frequency for momentum transfer (s^{-1}), e is the charge of an electron, ε_o is the permittivity of free space, m_e is the mass of an electron, and n_e is the electron density of the plasma. The operating frequency, ω, is taken directly from the simulation while the electron plasma frequency is given by,

$$\omega_{pe} = \left(\frac{e^2 n_e}{\varepsilon_0 m_e}\right)^{1/2}.$$

At 10 Torr, a value of $\nu_m = 5.5\cdot10^{10}$ s^{-1} is taken from the 2-D model described in Ref. [11]. For all additional gas pressures, we treat the electron temperature as approximately constant and assume that the collision frequency scales linearly with pressure and is given by,

$$\nu_m = 5.5\cdot10^{10}s^{-1}\cdot\frac{P[Torr]}{10\ Torr},$$

where P is the pressure in Torr.
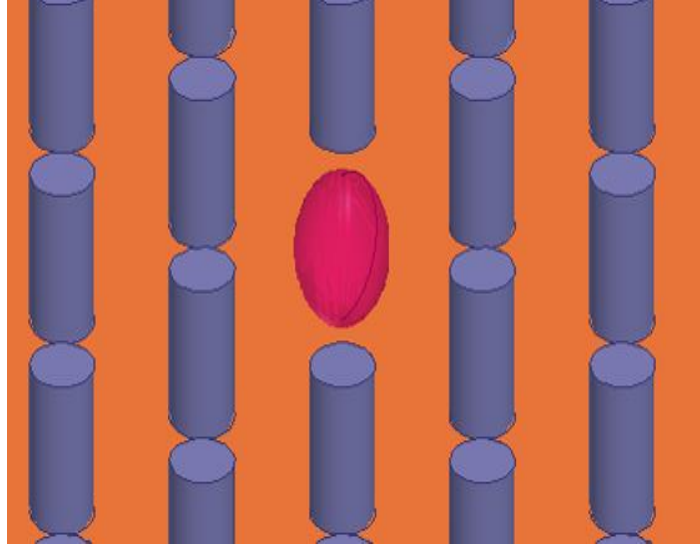
Figure 55 Ellipsoid dielectric volume used to simulate plasma volume within HFSS.

To complete the simulated electron density, the appropriate plasma size and collision frequency are entered into HFSS for the power level and pressure of interest. The PhC device was then simulated by sweeping the electron density between 10^{15} m^{-3} and 10^{18} m^{-3}. Upon completion of the simulations, the transmission coefficient for each electron density is normalized by,

$$\overline{S_{21}}(f_0, n_0) = \frac{S_{21}(f_0, n_0)}{S_{21}(f_0, 0)},$$

where f_0 is the resonant frequency of the no plasma case, $S_{21}(f_0, 0)$ is the transmission coefficient at f_0 *with zero electron density*, and $S_{21}(f_0, n_0)$ is the transmission coefficient at f_0 with an electron density n_0. The normalized transmission coefficient is shown in Figure 56. Normalization was required in order to compensate for differences between the simulated performance and experimental performance shown in Figure 41. It should be noted that the resonant frequency of the device shifts slightly with the changing electron density of the

94

plasma dielectric model, however, the transmission coefficient at the resonant frequency of the no plasma case is still used for normalization. This is done to be consistent with the experimental transmission data, which was always taken at the resonant frequency of the no plasma case.
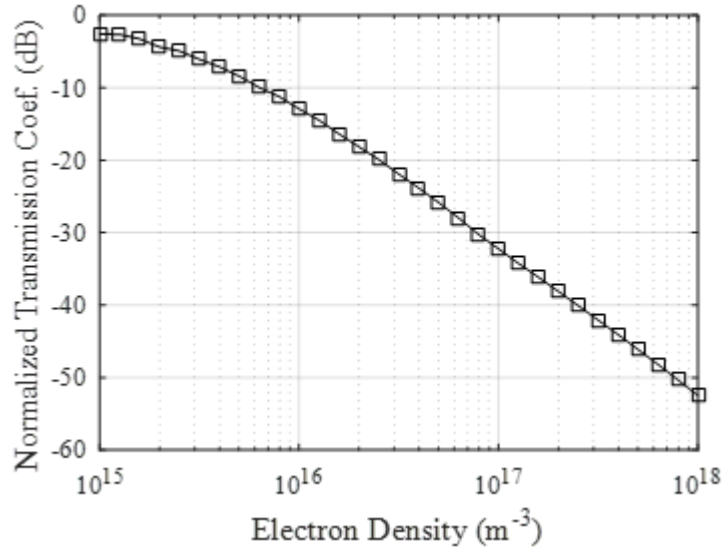
Figure 56 Example simulated normalized transmission coefficient as a function of electron density at the resonant frequency. HFSS parameters (plasma size and pressure) derived from experimental results of a 10 Torr argon plasma with a plasma size corresponding to an input power level of 780 mW.

To estimate the average electron density of the plasma, the simulated normalized transmission coefficient is compared to that of experiments. The comparison here gives the average electron density due to using the mean value of the Gaussian fit of the light intensity in determining size of the plasma for the HFSS model. As discussed previously, the transmission coefficient needs to be normalized to account for discrepancies between simulation and experiment. From Figure 43 and repeated in Figure 57 (left) is the experimental transmission coefficient of the no plasma case (black) and for a 10 Torr argon plasma with 780

mW of input power (blue). The experimental transmission coefficient is then normalized by

$$\overline{S_{21}}(f, Pin) = \frac{S_{21}(f, P_{in})}{S_{21}(f_0)},$$

where f is frequency, $S_{21}(f, P_{in})$ is the measured experimental transmission coefficient with a plasma present with P_{in} of input power, and $S_{21}(f_0)$ is the experimental transmission coefficient at the resonant frequency with no plasma present (-7 dB). The normalized experimental transmission coefficient is shown in red (blue line shifted by 7 dB) with a red diamond indicating the normalized transmission coefficient to be compared to simulation (no plasma resonant frequency), which for these conditions is ~ -10 dB. Figure 57 (right) shows the simulated normalized transmission from Figure 56, with the addition of red lines indicating the comparison with experiment. The average electron density is found at the point where the simulated transmission is equal to the experimental (both normalized), for which in this case is -10 dB, which corresponds to an average electron density of ~$6 \cdot 10^{15}$ m^{-3}.
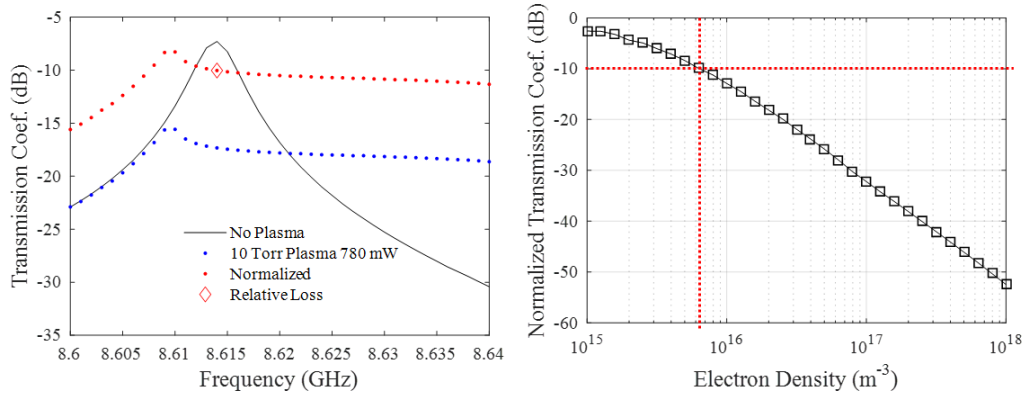
Figure 57 (Left) Experimental transmission of a 10 Torr argon plasma with 780 mW of input power shown in blue, normalized transmission shown in red, no plasma transmission shown in black. Red diamond indicates normalized transmission to be compared with simulation. (Right) Simulated normalized transmission with red lines indicating comparison with experimental normalized transmission.

To get an overall sense of the achievable electron densities with this PhC device, this process was repeated for several input power levels and for argon plasmas at 10 and 50 Torr. Shown in Figure 58 is the average electron densities (dashed lines) found by comparing the HFSS simulation results with experimental data. Additionally, the peak electron densities were calculated by scaling the average densities by the ratio of the peak light intensity to the mean light intensity of the Gaussian fit (Figure 54c). The solid lines in Figure 58 show the calculated peak electron densities. As expected, the average and peak electron densities of the plasma increase with input power and pressure. For the 10 Torr case, the electron density ranges from $1.6 \cdot 10^{16}$ at the lowest power level of 0.78 W and up to $5.3 \cdot 10^{16}$ at the highest power tested of 6.12 W. At 50 Torr, electron densities range from $4.6 \cdot 10^{16}$ at low power and up to $4.4 \cdot 10^{17}$ at the highest power.
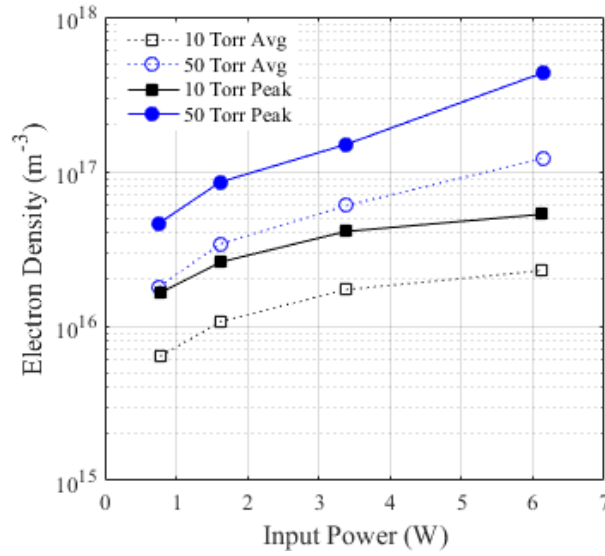
Figure 58 Average (dotted) and Peak (solid) electron densities for a 10 Torr (black) and 50 Torr (blue) argon plasma.

By altering the gas pressure and/or input power to the device, configurability of the transmission characteristics of the PhC device is achievable. Alteration of these variables leads to varying plasma electron density which causes a change in complex permittivity of the plasma. Listed in Table 3 are the plasma properties measured and calculated for a 10 and 50 Torr plasma within the PhC device. From Table 3 we note that the real part of the permittivity remains close to unity for all the conditions examined; this corresponds to operating above the electron plasma frequency ($\omega > \omega_{pe}$). Therefore, the changes in the PhC device behavior are mainly due to the modulation of the plasma conductivity (σ), which alters the dielectric loss tangent ($\tan \delta$) of the plasma within the PhC device cavity. The increase in loss tangent increases the electromagnetic energy absorption. In addition, the changing permittivity alters the impedance of the plasma-filled cavity

which leads to the increased power reflection due to mismatch in impedance with the waveguide channel, which is reflected in Figure 49.

Table 3 Measured and calculated plasma properties for a 10 and 50 Torr plasma within the PhC device.

Pressure	Input Power	Absorbed Power	Electron Density	ε_{rp}	tan δ	σ
(Torr)	(W)	(W)	(m^{-3})			(S/m)
10	0.78	0.2	1.64E+16	0.991	0.009	4.3E-3
10	1.63	0.37	2.60E+16	0.986	0.014	6.8E-3
10	3.38	0.72	4.09E+16	0.978	0.023	10.6E-3
10	6.12	1.33	5.28E+16	0.972	0.030	13.7E-3
50	0.76	0.26	4.63E+16	0.998	0.010	4.6E-3
50	1.62	0.45	8.55E+16	0.997	0.018	8.4E-3
50	3.39	0.85	1.50E+17	0.994	0.031	14.8E-3
50	6.15	1.47	4.37E+17	0.982	0.092	43.1E-3

5.5 Summary

From the preceding experimental results and electron density measurements, a resonant cavity within a photonic crystal is an effective means of creating a dense plasma. What is also evident, is that the plasma becomes highly conductive with increasing pressure and power, and as a result, effectively dampens the output power of the device. Combined with the fast transient turn on time of the plasma, this device makes an effective power limiter at the resonant frequency of the cavity. In the next chapter, a similar photonic crystal design will be explored, this time at 43 GHz. At this frequency, the dimensions of the crystal shrinks to accommodate the smaller wavelength, including the height of the cavity. With a smaller cavity, the power density is increased leading to a higher electric field and the effects of this is explored next.

6   Photonic Crystal Plasma formation in the Millimeter-Wave Regime

In this section, I will explore the frequency scaling of 2-D photonic crystal arrays by reducing the dimensions of the 8.5 GHz PhC device by a factor of ~5. While many of the design aspects of the device design at 43 GHz are the same as the 8.5 GHz version, several modifications of the device design will need to be modified to physically realize a device at this frequency. The most significant change at this frequency is with the input and output of electromagnetic energy to the device. Coaxial connections have significantly more loss at 43 GHz, and lack of available amplifier power at this frequency further underscores the need to reduce losses where possible. With the change in energy delivery method, other modifications are also made, including the array size and cavity height. These changes and their effects will be explored in Section 6.1.

With the increase in operating frequency comes a decrease in the physical size of the device. Careful attention needs to be paid` to available materials and construction methods in order to achieve a functioning device. To that end, CoorsTek® alumina is again used for a design at 43 GHz, primarily due to its known performance at 8.5 GHz, but also due to a large selection of rod diameters commercially available. Using the scaling properties of photonic crystals, the same band gap map used previously for the 8.5 GHz device can be used here, but with scaled axes. Figure 59 shows the band gap map for a square lattice of dielectric rods ($\varepsilon_r = 9.8$) in air. The axes have been scaled for the new lattice constant of 2.794 mm (0.11 inches). Red lines indicate the desired frequency of 43 GHz and

corresponding commercially available rod radius of 0.508 mm (0.2 inches). The

operating frequency of 43 GHz was chosen to be in the higher gain region of the 42

– 47 GHz waveguide amplifier that will be utilized for experiments. The dielectric

rod radius was chosen to be the closest commercially available size while being

centered within the bandgap at a frequency of 43 GHz.
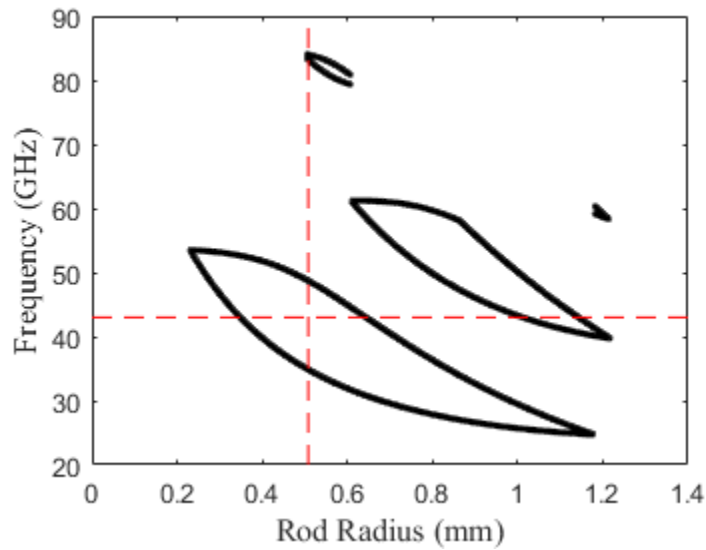
Figure 59 Band gap map for a photonic crystal with square lattice of rods (permittivity = 9.8) in air. Axes scaled for a lattice contant of 2.794 mm. Red dashed lines indicate design parameters

6.1   Design Considerations

6.1.1   3-D Modeling Environment

As with the 8.5 GHz device, and discussed in the 3-D Modeling

Environment subsection of Chapter 5.1, HFSS will again be used to simulate all the

desired design parameters. Starting with the simplified design shown in Figure 23,

the lattice spacing was changed to 0.11 inches (2.794 mm) and the rod diameter

was changed to 0.04 inches (1.016 mm) and is shown in Figure 60. The cavity

height (rod length) was set to 0.112 inches (2.845 mm), which is the same height

as a standard WR-22 waveguide (0.112 inches by 0.224 inches), which is used for the dimensions of the waveguide ports within HFSS. Boundary conditions for the 43 GHz device are the same as the 8.5 GHz device and are shown in Figure 26. The same alumina material will also be used for this device as with the 8.5 GHz device. While the performance of the Coorstek® AD-998 alumina was excellent at 8.5 GHz, the dielectric properties are an unknown factor at 43 GHz. Since the properties are unknown, the same values will be used here (Relative Permittivity = 9.8, Dielectric Loss Tangent = 0.0001).
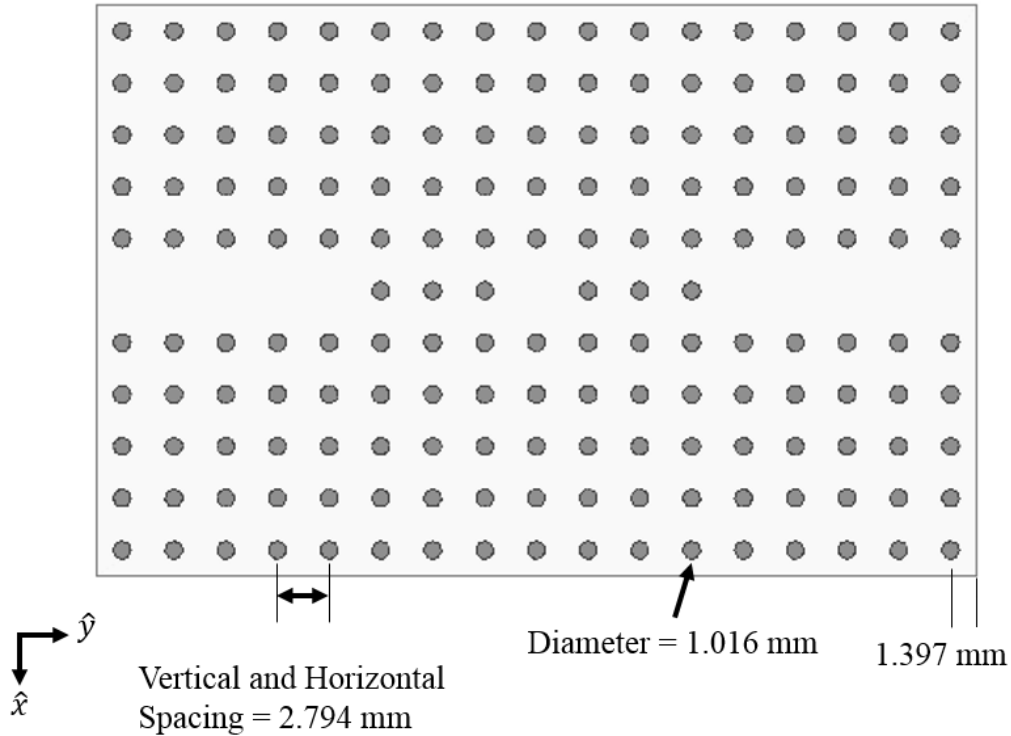
Figure 60 Physical dimensions of the 43 GHz PhC device for use in HFSS

6.1.2 Number of Resonator Rods

As with the 8.5 GHz device, the number of dielectric rods on either side of the cavity affects the transmission and resonant properties of the device. Using HFSS these properties where simulated for one to four dielectric rods on either side of the cavity. Shown in Figure 61 is the transmission (left) and reflection (right) coefficients of the device. As expected from the previous results, the transmission through the device reduces and reflection increases for each new pair of rods is introduced. However, as with the 8.5 GHz device, three resonant rod pairs give high transmission and low reflection while having a sufficiently high quality factor (Q ~ 2300).
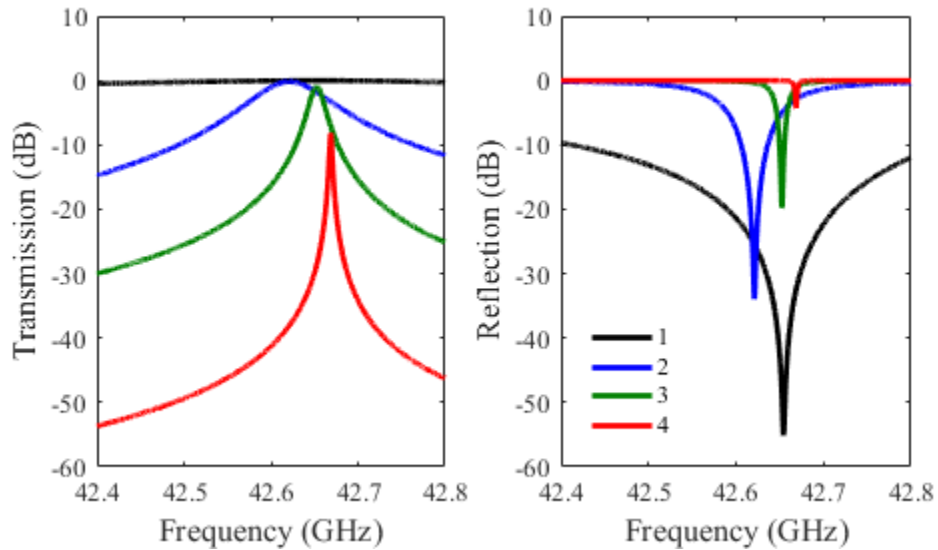
Figure 61 Simulated transmission (left) and reflection (right) of the 43 GHz PhC device for various number of dielectric rods on either side of the resonant cavity.

For the 43 GHz device, the height of the dielectric rods, and thus the cavity height is much smaller than the 8.5 GHz device and as such, the electric field within the cavity is expected to be greatly increased. Shown in Figure 62 is the electric

103

field amplitude within the cavity for one to four dielectric resonator rod pairs and a cavity height of 2.845 mm. Again, the electric field increases with number of rod pairs and thus the confinement of the fields as expected. Of note is the increase in the electric field amplitude as compared to the 8.5 GHz device and shown in Figure 29. There is a reduction of ~ 3.5 in cavity height as compared to 8.5 GHz design and an increase by a factor of ~ 4.1 in electric field amplitude for three resonator pairs case.
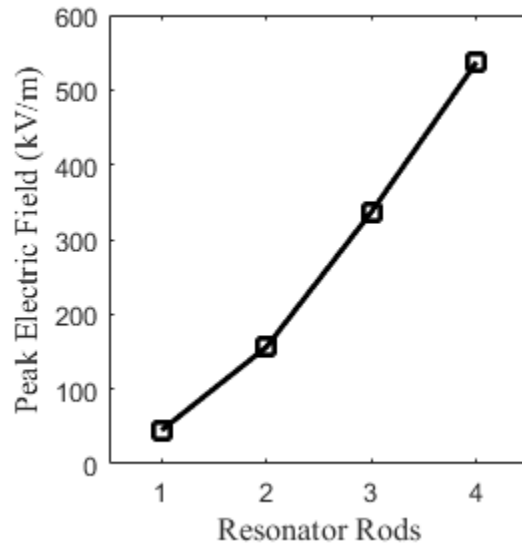
Figure 62 Peak electric field amplitude for 1 W of input power at the resonant frequency as a function of the number of resonator rod pairs and for a cavity height of 2.845 mm.

A summary of the performance characteristics of the 43 GHz PhC device in relation to the number of resonator rod pairs is found in Table 4. As expected, the four resonator rod pairs have the highest quality (Q ~ 13747) factor and electric field (537.2 kV/m) within the cavity. Again, however, the transmission and reflection characteristics are unacceptable (-8.2 dB and -4.3 dB respectfully). As with the 8.5 GHz device, a good compromise between transmission performance

104

and electric field intensity is found in the three resonator rod pairs case. For three

resonator rod pairs, a quality factor of 2344 and an electric field amplitude of 336.9

kV/m is achieved while having a transmission coefficient of only -0.9 dB. Based

on the performance, the remainder of the design will focus only on the three

resonator rod pairs configuration.

Table 4 Summary of the effect of the number of resonator rod pairs has on performance characteristics. All values obtained using HFSS with 1 Watt of input power at a cavity height of 2.845 mm.

Resonator Rods	f_0 (GHz)	Transmission (dB)	Reflection (dB)	BW (MHz)	Q	E (kV/m)
1	42.6538	-0.02	-55.1	N/A	N/A	44.8
2	42.6211	-0.2	-33.9	91.3	467	156.2
3	42.6525	-0.9	-19.8	18.2	2344	336.9
4	42.6687	-8.2	-4.3	3.1	13747	537.2

6.1.3   Input and Output Design

At 43 GHz, high losses in coaxial cables preclude their use with this system,

however, rectangular waveguide has very little loss and is the ideal option for this

frequency. Without the need for coaxial probes as our energy delivery method, the

removal of the input and output waveguide channels from the 8.5 GHz is feasible

and the effect of this modification will be examined here.

The removal of the input and output waveguides alters the horizontal array

size, and as with the modification of the vertical array size in chapter 5.1, the

confinement of the electric field is affected. Shown in Figure 63 is the electric field

amplitude for horizontal array sizes of 17 (top) and 7 (bottom).   In both

configurations, the bulk of the electric field is confined to the center defect and the

surrounding dielectric rods and the magnitude of the field is unchanged.

105
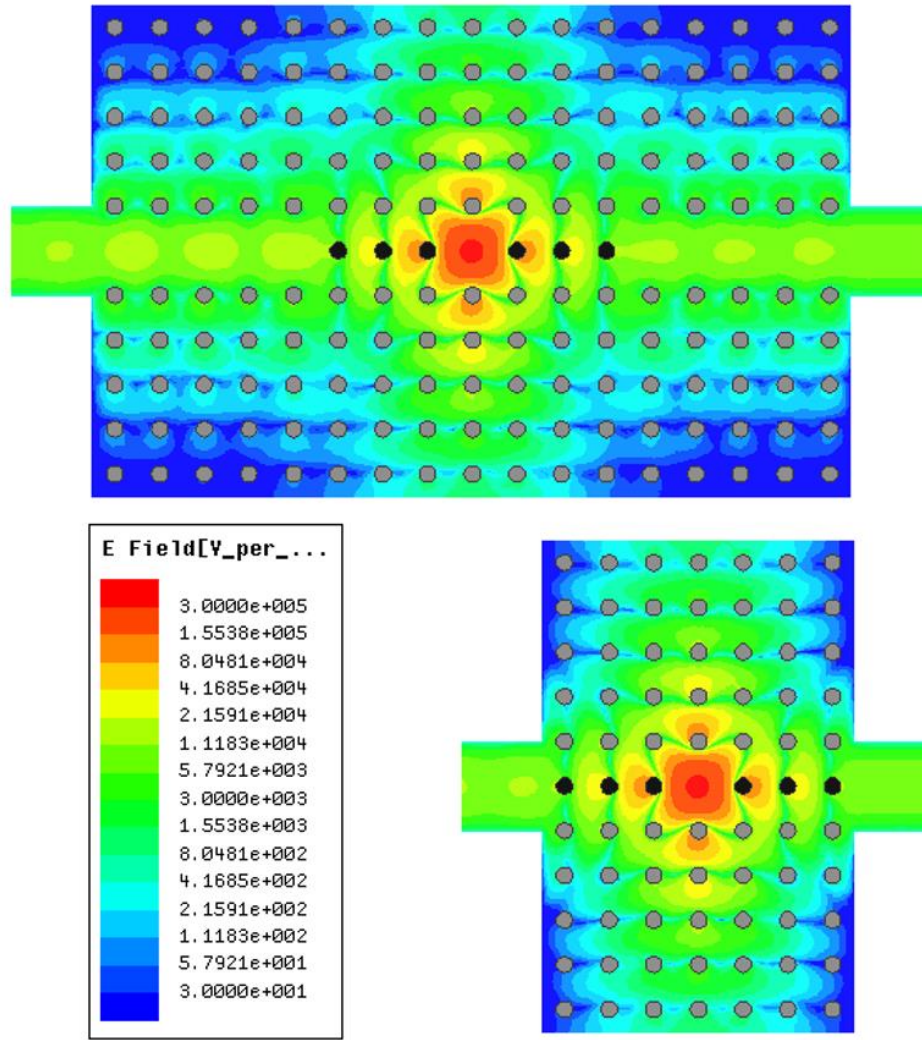
Figure 63 Electric field amplitude (log scale) for a horizontal array size of 17(top) and 7 (bottom) for a 1 W input.

To show the full effect of modifying the horizontal array size has on the operating characteristics, the array size was varied from 7 to 17 (in steps of 2) in HFSS. Shown in Figure 64 is the transmission and reflection coefficients, and the peak electric field within the center defect as a function of horizontal array size. The black squares represent the results from using the simplified model, which has perfectly conducting boundaries (no conductive losses). Since the horizontal array

size greatly effects the travel length of the electromagnetic wave within the device, also included are results which add copper boundaries to the HFSS model, which greatly increases the conductive losses and are shown with blue circles. Both configurations show a similar pattern with respect to the horizontal array size with the best transmission and reflection occurring with an array sizes of 7, 13, and 17. For the electric field however, the best performance occurs at array sizes of 11 and 15, which is not expected from the transmission and reflection data. The differences in electric field amplitude are not significant enough to necessitate the use of additional dielectric rods and thus an array size of 7 was selected.
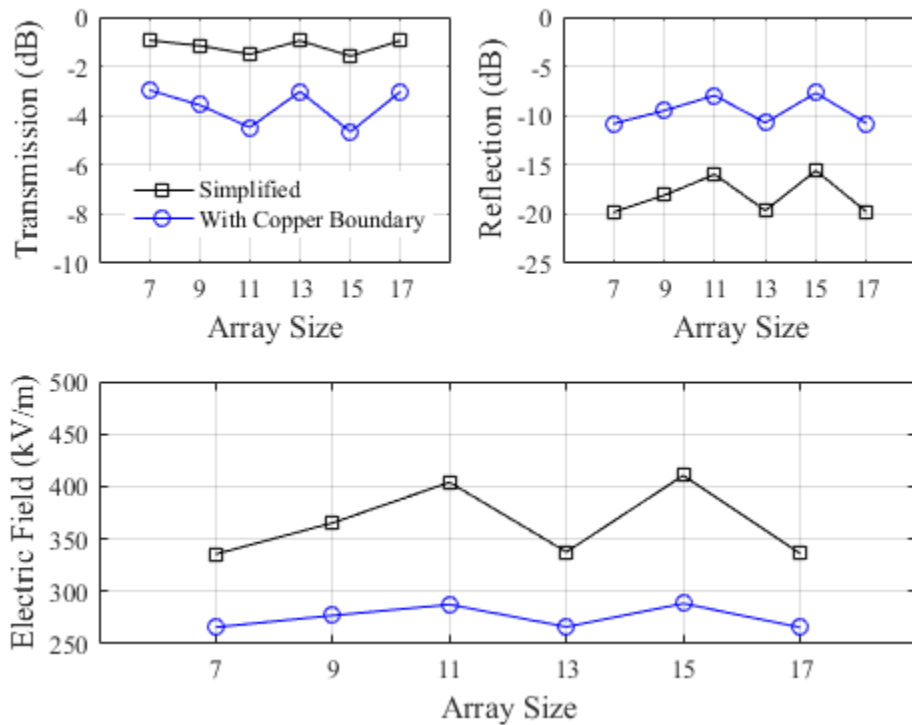
Figure 64 Performance parameters of the 43 GHz PhC device using a simplified model (black squares) and model using copper boundaries (blue circles) for a 1 W input.

Of note from the data shown in Figure 64 is the loss of performance that comes with the use of copper boundaries as compared to the perfectly conducting boundaries. With an array size of 7, the transmission coefficient drops from 80% to 50% and the reflection coefficient increases from 1% to 8%. Additionally, the electric field within the cavity drops from 335 kV/m to 266 kV/m, a 20% reduction. This is a significant performance loss that will only worsen at higher and higher frequencies. However, these losses could potentially be mitigated with further investigation into alternate device boundaries, i.e. high permittivity dielectrics or layers of dielectric materials.

6.1.4   Cavity Height

It was shown for the 8.5 GHz that the dielectric rod length and cavity height has an effect on the transmission and reflection coefficients, and as well as the electric field strength within the cavity. To determine the effect for the 43 GHz device, the cavity height was varied from 2.845 mm (1X waveguide height) to a height of 6.828 mm (2.4X waveguide height) within HFSS. For all cavity heights, the input and output waveguide ports had a constant size and were centered vertically. The conducting copper boundaries from the previous section are also included in the HFSS model. The resulting transmission and reflection coefficients at the resonant frequency is shown in the top of Figure 65. At the lowest cavity height, a transmission coefficient of -2.96 dB is found increases slowly until it peaks at -2.01 dB at a cavity height of 5.405 mm (1.9X waveguide height). Starting at a cavity height of 5.69 mm (2X waveguide height) the transmission coefficient

begins to drop more rapidly, reaching a value of -13 dB at the highest cavity height

tested. The reflection coefficient follows a similar trend in inverse.
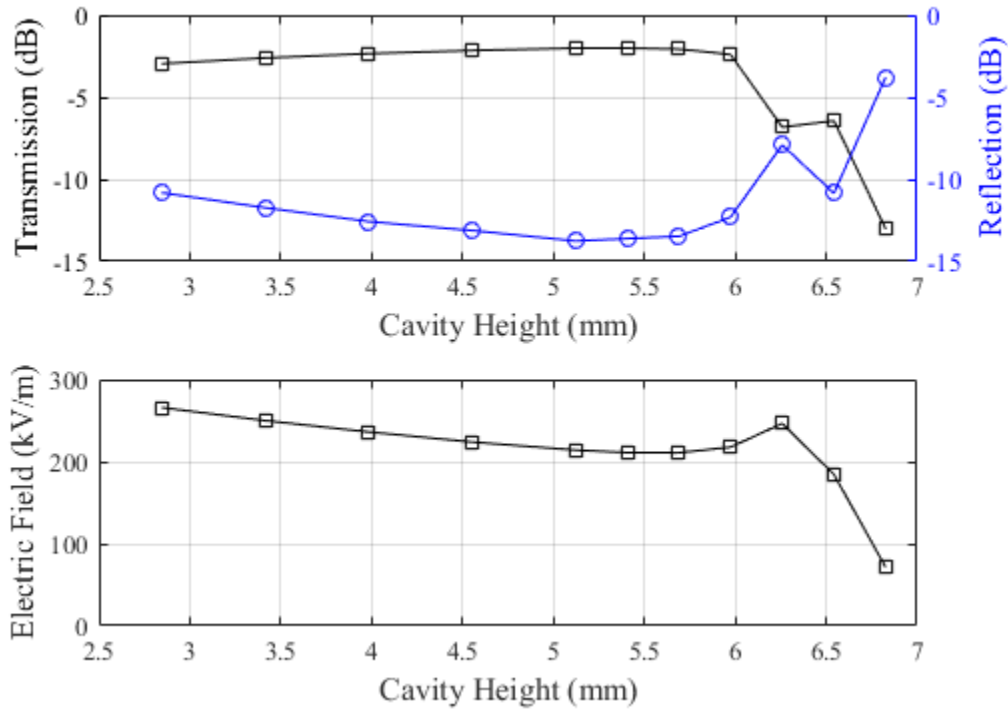
Figure 65 (Top) Transmission and reflection coefficients at the resonant frequency as a function of cavity height. (Bottom) Electric field amplitude within the central cavity for a 1 W input.

As has been stated multiple times, the electric field intensity within the central cavity is the predominate performance metric for plasma ignition. Shown in Figure 65 (bottom) is the electric field amplitude within the central vacancy. The maximum electric field is achieved at the lowest cavity height and decreases with increasing cavity height. At a cavity height of 2.845 mm (1X waveguide height), the electric field reaches 266 kV/m for an input power of 1 W. Not anticipated is the electric field intensity beginning to increase after reaching a local minimum of 210.8 kV/m at a height of 5.69 mm (2X waveguide height). A new local maximum

of 246.5 kV/m occurs at a cavity height of 6.259 mm (2.2 X waveguide height), at which point the electric field drops sharply with increasing cavity height.

For the initial device, a cavity height of 2.845 mm (1X waveguide height) is chosen as it has the highest electric field potential and is the most simplistic design to construct. Additionally, the transmission and reflection coefficients are acceptable for experiments. Experimentation with larger cavity heights may be accomplished in the future.

6.1.5   Final Design

The final design of the 43 GHz PhC device includes the previously discussed design parameters as well as additional modifications for construction. An exploded view of the final design is shown in Figure 66. As with the 8.5 GHz device, the addition of a perforated plate is needed to keep in place the dielectric rods. In lieu of a second perforated plate at the bottom, counterbore holes are drilled into the bottom casing for rod placement. A copper plate is added at the top of the device to secure the dielectric rods in place. Copper walls with threaded holes (screw holes not shown in figure) are placed at the input and output to attach waveguides for power transport.
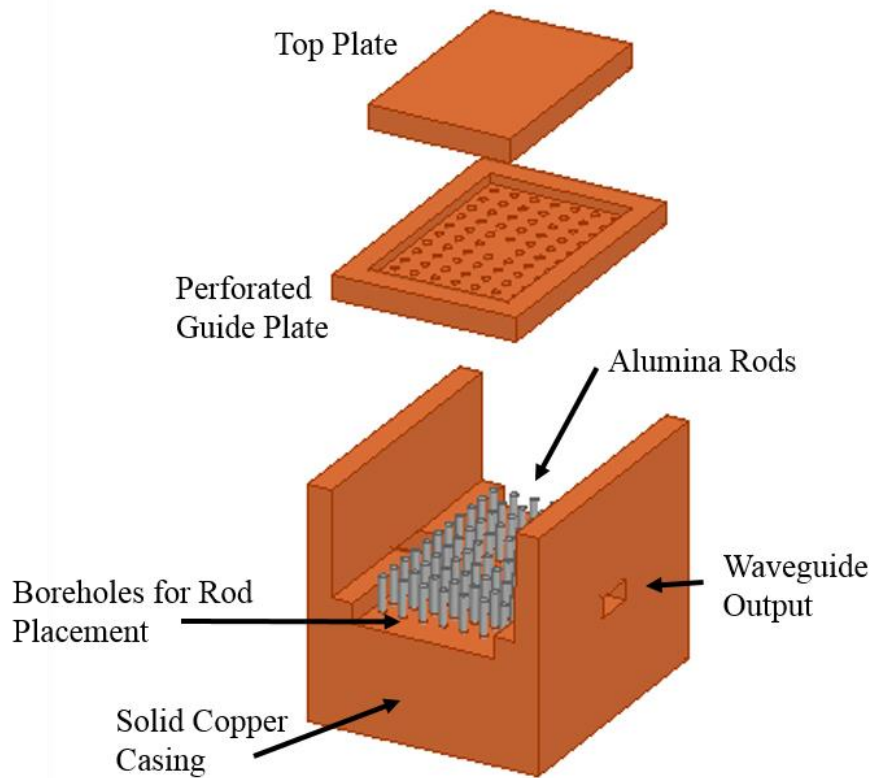
Figure 66 Final design of the 43 GHz PhC device including the main device casing, a perforated guide plate, and top plate. Partially exploded view for clarity.

As before, the addition of the perforated guide plate and counterbored holes in the casing adds additional length to the dielectric rods, which will alter the performance parameters of the device. Keeping a cavity height of 2.845 mm, the dielectric rods were increased in length to 6.604 mm (0.26 inches), which is a significant increase. Such a large increase in length is needed to make sure that the rods were sunk deep enough into the casing and guide plate to be mechanically stable. To verify the performance of this change, the device was again simulated using HFSS and the results are shown in Figure 67. The transmission (top, black) and reflection (bottom, black) coefficients are -2.2 dB (60.3%) and -13.1 dB (4.9%)

at the resonant frequency and are comparable to the 2.845 mm cavity height case

shown in blue. There was however a small shift in the resonant frequency, from

42.65 GHz for the case of both rod and cavity having a height of 2.845 mm (blue),

to 42.86 GHz. This 200 MHz shift (0.5%) is relatively small and is caused by the

addition of the extra dielectric material as well as meshing differences in the

simulation.
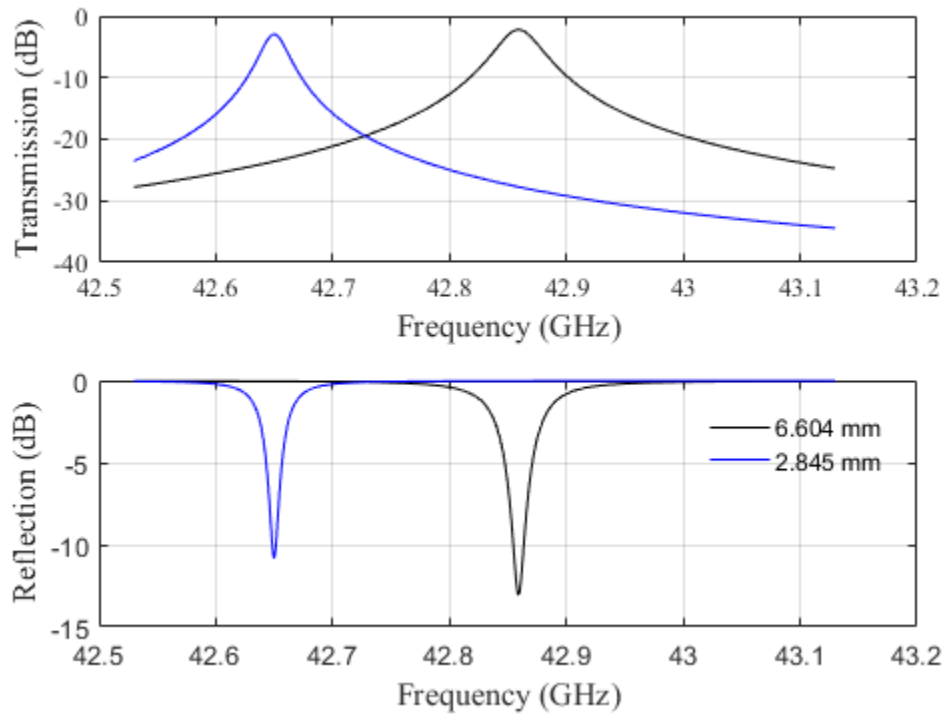
Figure 67 Simulated transmission (top) and reflection (bottom) coefficients for the finalized 43 GHz PhC design using 6.604 mm dielectric rods (black) and for the more simplified model using 2.845 mm dielectric rods (blue).

In addition to the shift in resonant frequency, the electric field is also altered

and is shown in Figure 68. The longer dielectric rods alters the electric field pattern

in and around the dielectric rods adjacent to the central vacancy. This alteration

leads to a decrease in the electric field in the center of the cavity from 266 kV/m

(2.845 mm, bottom) to 210 kV/m (6.604 mm, top) for a 1 Watt input, a 21%
decrease. While this is a relatively large decrease in electric field amplitude, the
longer dielectric rods are necessary for mechanical stability. Even with the
decrease, an electric field amplitude of 210 kV/m for a 1 Watt input is sufficiently
high to enable gas breakdown.
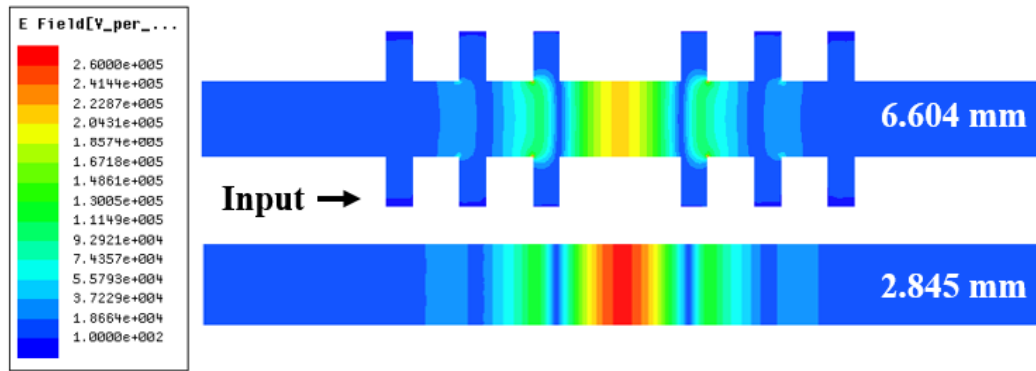
*Figure 68 Simulated electric field amplitude as viewed from the side for dielectric rod length of 6.604 mm (top)
and 2.845 mm (bottom) for an input power of 1 Watt.*

The fully constructed device is shown in Figure 69. The device consist of
three copper components and 76 alumina rods. The largest component is
manufactured from a solid block of copper with a two-tiered channel for the cavity
(side view showing the two tiers is shown in the top of Figure 69). At the bottom
of the channel, counterbored holes hold the dielectric rods in place. The second tier
serves to hold the perforated guide plate in place, which serves to hold the top of
the dielectric rods in place. On the other side of the copper block, waveguide ports
are milled and guide holes and threaded through-holes are added based on the UG-
383/U flange pattern (flange used for WR-22 waveguide) and is shown in the

middle of Figure 69. The bottom of Figure 69 shows the top view of the device with the cover plate removed and shows the dielectric rod pattern.
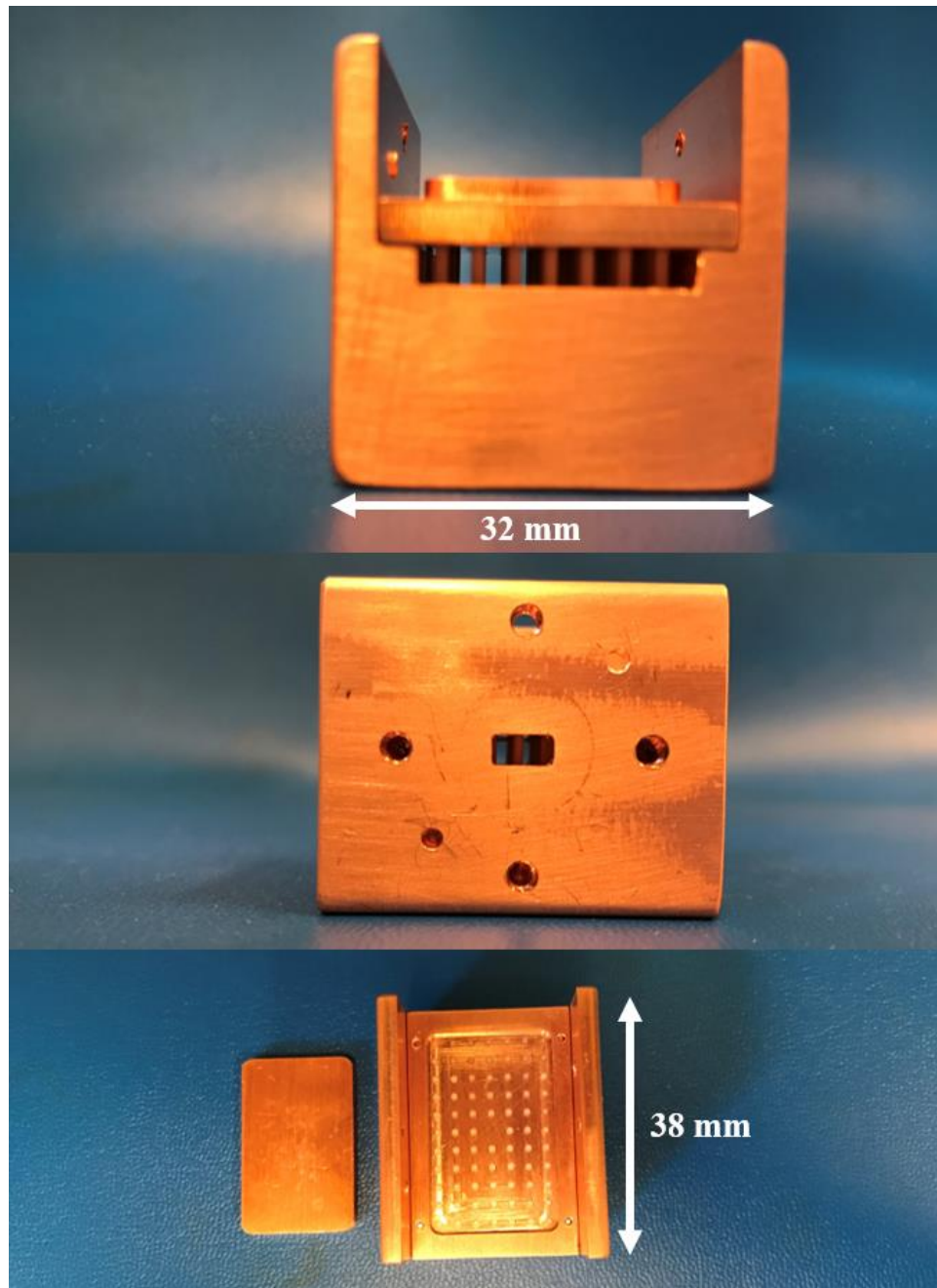
Figure 69 Photos of the constructed 43 GHz PhC device showing the side (top), input (middle), and top (bottom).

6.2   Experimental Setup

The experimental setup for the 43 GHz device is similar to the 8.5 GHz experimental setup as discussed in section 5.2, but with modifications due to the higher frequency and the need for rectangular waveguide instead of coaxial cables. The experimental setup for the 43 GHz PhC device is illustrated in Figure 70. The PhC device is placed in a vacuum chamber and pumped to a base pressure of 10 mTorr and backfilled to the desired pressure with argon. Pressure is measured using a Grancille-Phillips 475 Convectron controller and gauge which was factory calibrated for use with argon. Millimeter wave power is delivered via WR-22 rectangular waveguide which is attached to the input port of the device. A custom vacuum flange with mica window (60 µm thick) was fabricated to transition to the air side of the vacuum chamber. On the air side of the chamber, millimeter wave power was generated using a Keysight N5183A signal generator and a Millitech AMC-22 4X active multiplier to feed a Millitech AMP-22-40060 power amplifier. Output power of the amplifier is adjusted using a variable attenuator between the 4X multiplier and the amplifier. A Millitech CL4-22 dual coupler at the output of the amplifier samples the forward and reflected power from the PhC using Keysight N8487A power sensors and an E8487A power meter. For time transient measurements, the amplifier was gated by 1 ms pulses with a 50% duty cycle.
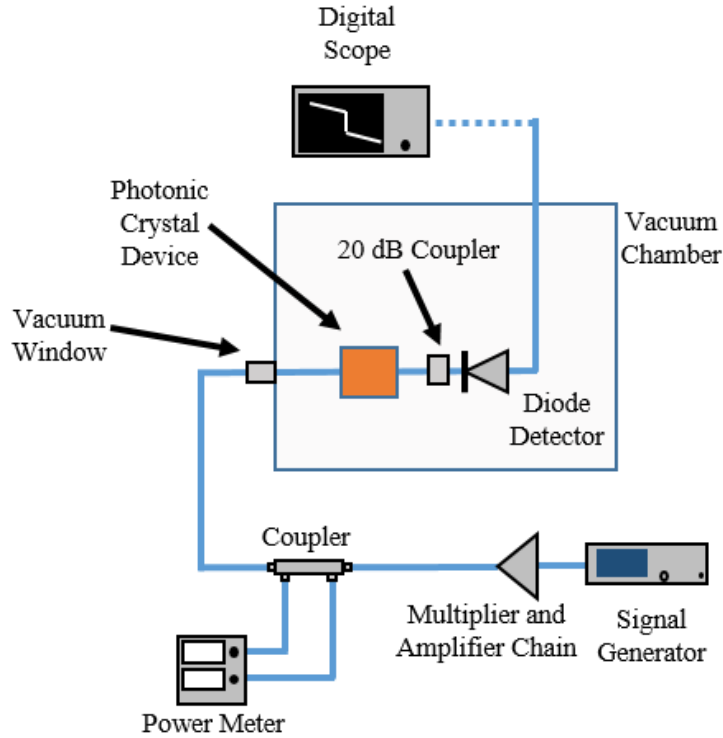
Figure 70 Experimental setup for determining the transmission loss and plasma formation time of the 43 GHz PhC device.

To measure the device output, the output port of the PhC device is connected to a 20 dB coupler and Sage Millimeter SFD-333503-22SF-N1 diode detector. The 20 dB coupler serves as protection for the diode detector by reducing the power to acceptable levels. The SMA output of the diode detector is fed through a SMA vacuum feedthrough and connected to a digital oscilloscope for voltage measurement. The diode detector was loaded at the oscilloscope in one of two ways depending on the measurement type. For steady-state measurements, the diode detector connected to the internal 1 MΩ load of the oscilloscope. For time transient measurements, a 50 Ω feedthrough load was inserted between the diode detector and oscilloscope in improve the transient response time of the diode detector. As

before, all system losses were measured and incorporated into final measurement values. In addition to system losses, two calibration curves for the diode detector were performed to convert measured voltage into power, one using 50Ω feedthrough load and one using the 1 MΩ internal load.

6.3 Experimental Results

In this section I report the steady-state and transient behavior of the 43 GHz PhC device. All experiments were conducted using argon gas. Due to the limited amplifier power available at 43 GHz, all experiments were conducted using less than 3 Watts of input power. Consequently, a more limited set of experiments were feasible. For instance, power needed for gas breakdown versus pressure was not able to be performed as breakdown only occurs at ~ 40 Torr of argon given the limited input power available. Also, I was not able to explore the effect that input power has on the plasma properties. However, experiments conducted at 8.5 GHz should be sufficient to understand the relevant behavior. For all experiments at pressures other than 40 Torr, the plasma is first ignited at 40 Torr before the desired gas pressure is set. Using this method, a plasma could be maintained for argon gas pressures of 30 Torr to near atmospheric pressure (750 Torr).

To verify operation of the device, and to determine the resonant frequency, a measurement of the transmission coefficient was performed first. Shown in Figure 71 is the simulated transmission coefficient using HFSS (blue) and the experimental (black) transmission coefficient of the 43 GHz PhC device. The simulated results show transmission of -2.2 dB at the resonant frequency of 42.86

GHz. Experimental results show transmission of -2.5 dB at a resonance frequency of 43.53 GHz, which constitutes a resonant frequency shift of 1.6 % and loss of 0.3 dB from the simulated results. This is in very good agreement with the differences attributed to differences in permittivity, dielectric loss, and dimensional tolerances.
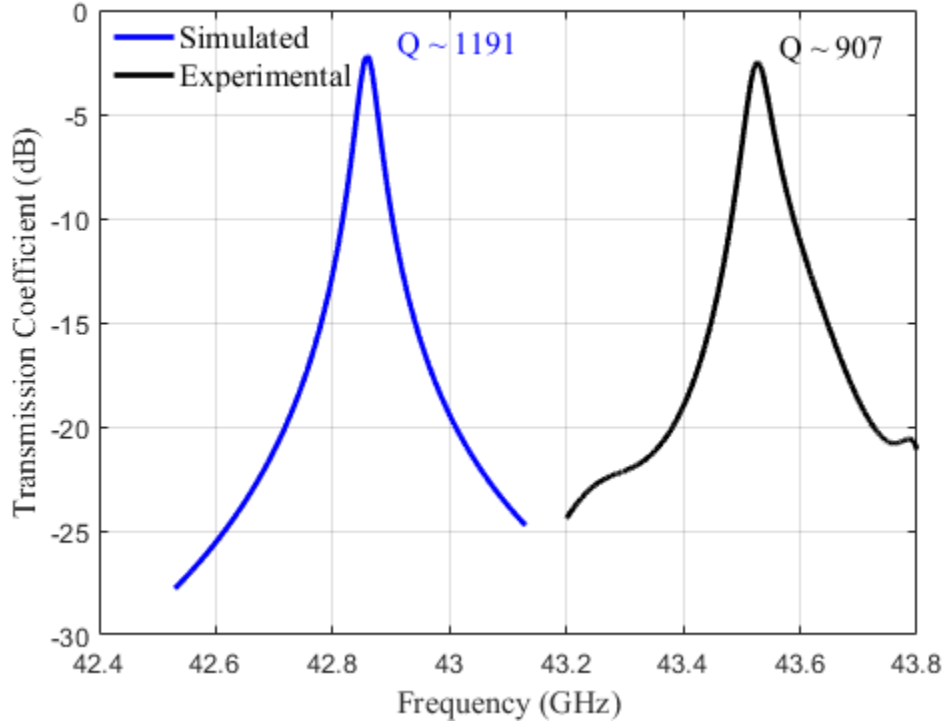
Figure 71 Transmission coefficient (S21) of the 43 GHz PhC device without plasma. Simulation using HFSS (blue) and experimental (black).

Transmission performance of the 43 GHz PhC device is greatly improved from the 8.5 GHz device (see Figure 41). This is primarily due to the choice in input and output methods. The E-field probe used for the 8.5 GHz device is not well optimized and thus using the waveguide is much preferred.

Plasma operation is verified by applying millimeter wave power at the resonant frequency to the PhC device. Figure 72 shows the side view of the PhC

118

device prior to gas breakdown (top) and with a steady-state plasma. When sufficient power is applied at the resonant frequency, a plasma forms in the free space cavity formed by the point defect in the lattice. The plasma forms completely within the free space cavity and is not in contact with the dielectric lattice.
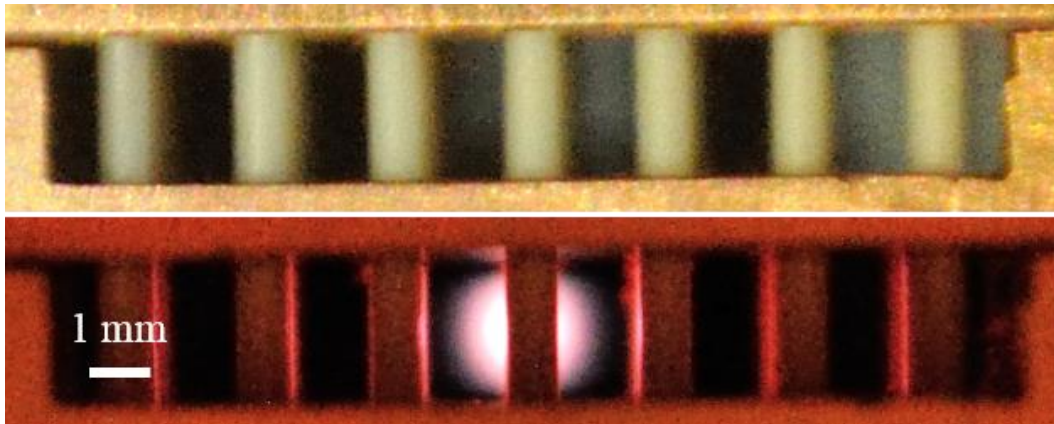
Figure 72 (Top) Side view of PhC device prior to gas breakdown. (Bottom) Side view of PhC device with 40 Torr argon plasma with 1 W of input power. The plasma image is partially obscured due the presence of dielectric rods.

6.3.1 Effect of Gas Pressure on Transmission Through Plasma

As was shown with the 8.5 GHz device, the presence of a plasma greatly affects the transmission of energy through the device. Shown in Figure 73 is the transmission coefficient at the resonant frequency for pressures ranging from 30 to 750 Torr. For this experiment, the steady-state output power of the PhC device was measured and compared to the measured input power. Input power was maintained at 1.5 Watts to ensure that any change in transmission properties where due to the change in pressure. The dashed line of Figure 73 represents the device transmission prior to a plasma present, and shows that the transmission is ~ -2.5 dB and is not dependent on gas pressure. The solid black line represents data taken in the

presence of a plasma using a 1.5 Watt input. Transmission through the plasma

varies between -23 dB at 30 Torr and -42 dB at 625 Torr.
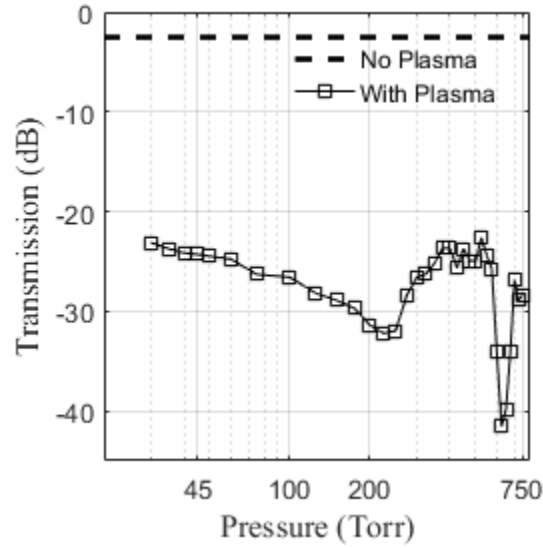
Figure 73 Steady-state transmission coefficient through the 43 GHz PhC device as a function of pressure without the presence of plasma (dashed) and with a plasma present (solid squares). Data taken in argon using 1.5 Watts of input power.

Re-configurability of the transmission properties of the device is achieved

by adjusting the complex permittivity of the plasma element within the central

defect. This is achieved by adjusting the gas pressure, which results in a change in

electron density, plasma frequency, electron collision frequency, and conductivity.

Combined, these properties modify the transmission coefficient of the photonic

crystal. However, these properties do not all change linearly. The right side of

Figure 74 shows values of the collision frequency (v_m), conductivity (σ), and

electron density (n_e) as they vary with pressure. The collision frequency was taken

from Ref. [11] and changes linearly with pressure, the electron density was

calculated using the method from section 5.4 and will also be discussed later in

120

section 6.3.3. Using these quantities, the plasma conductivity was calculated (see Chapter 0) and plotted versus pressure. The conductivity and electron density increases rapidly with pressure until 200 Torr, resulting in a decrease in the quality factor of the cavity and a decrease in transmission and is shown in Figure 74 (left, shaded blue). Between 200 and 550 Torr, the electron density beings to saturate, however, the collision frequency continues to increase linearly, resulting in a decrease in conductivity. This results in an increase in quality factor and an increase in transmission, as shown in Figure 74 (left, shaded tan).
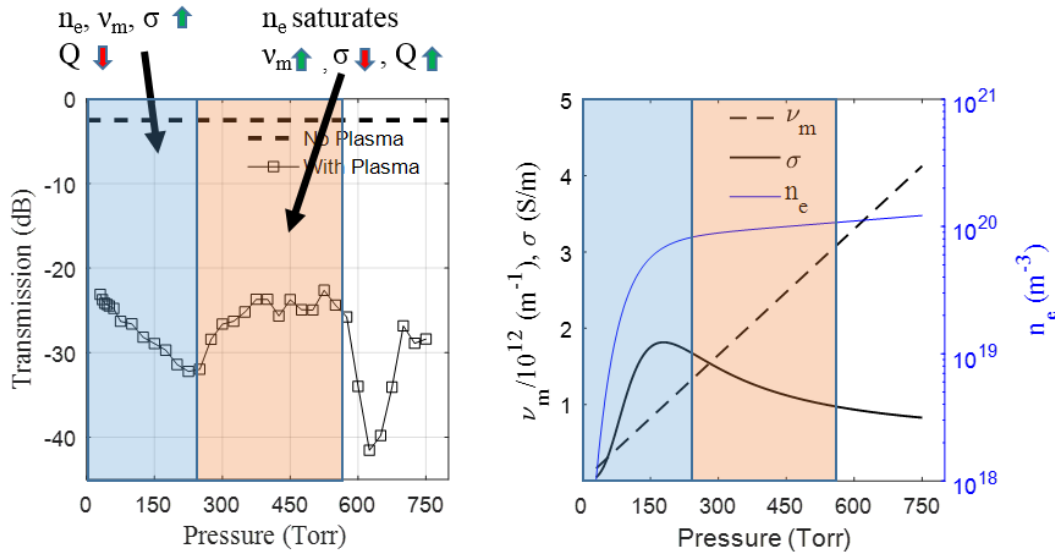
Figure 74 (Left) Steady-state transmission versus pressure for the 43 GHz PhC, with annotation. (Right) Normalized values of collision frequency (ν_m), conductivity (σ), and electron density (n_e) as they vary with pressure.

At 625 Torr, a significant and sudden decrease in transmission occurs, to ~ -42 dB. From observations, the plasma light intensity is not noticeably brighter than the light intensity at the surrounding pressures. Typically, plasma light intensity correlates well with electron density. This suggest that a sudden increase in electron density is not the cause of the loss of transmission. We speculate that

121

the parameters and physical size of the plasma act to simulate the missing dielectric rod in the cavity, thus creating a defect-free photonic crystal. However, this is not yet well understood and further investigation is still needed.

6.3.2   Transient Response

As was discussed in section 5.3.7, the transient response of the PhC is measured indirectly by observing the time evolution of the output power. Millimeter wave power is applied to the amplifier, where the output is gated by using an arbitrary waveform generator to achieve a pulsed (2 ms period, 50% Duty Cycle) input into the PhC. The pulsed excitation allowed for triggering of the oscilloscope and for collection of multiple cycles for signal averaging. The output power is measured using a diode detector and oscilloscope. Voltage from the oscilloscope is then converted into power by using the appropriate calibration curve for the diode detector.

Figure 75 plots the time evolution of the output power of the PhC device for various conditions. For the no plasma case and starting with the onset of input power at t=0, the output power increases for ~4 µs before reaching a steady-state output power condition. This response time is primarily the amplifier turn on time for a gated output. In the cases with plasma ignition (30, 45, 750 Torr lines) and again starting with the onset of input power at t = 0, the rise in output power is interrupted by the plasma ignition. The time required from t = 0 to plasma ignition is dependent of gas pressure and is known as the statistical delay time [93]. After

ignition, plasma begins to fill the crystal defect and a rapid loss in output power is observed, ultimately leading to a low output power steady-state condition.
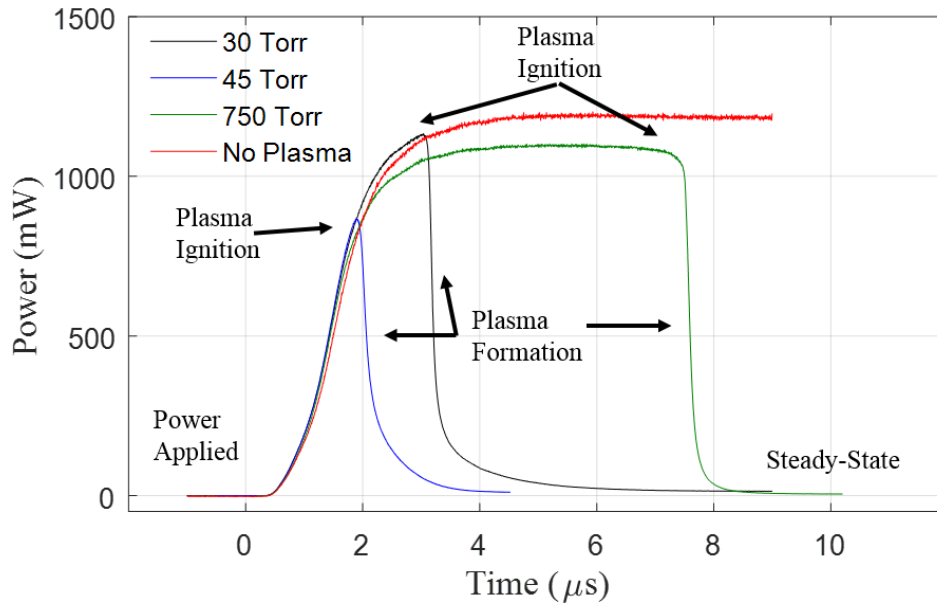
Figure 75 Transient output power for the 43 GHz PhC for a pulsed 2 W input for various plasma conditions.

The time from the onset of breakdown to a steady-state condition is called the plasma formation time, and it is an important parameter in understating the dynamic nature of the PhC device. Formation time is calculated by measuring the time required for the output power to drop from 90% to 10% of the peak output value. The measured plasma formation time for pressures ranging from 30 to 750 Torr is shown in Figure 76. The plasma formation time ranges from 790 ns at 45 Torr and decreases rapidly with increasing pressure to 180 ns at 400 Torr. Due to the limited power available at 43 GHz, the effects of input power on the plasma formation time at this frequency was not conducted. However, it is reasonable to

assume that the formation times would decrease with increasing power as they do at 8.5 GHz (see Figure 52).
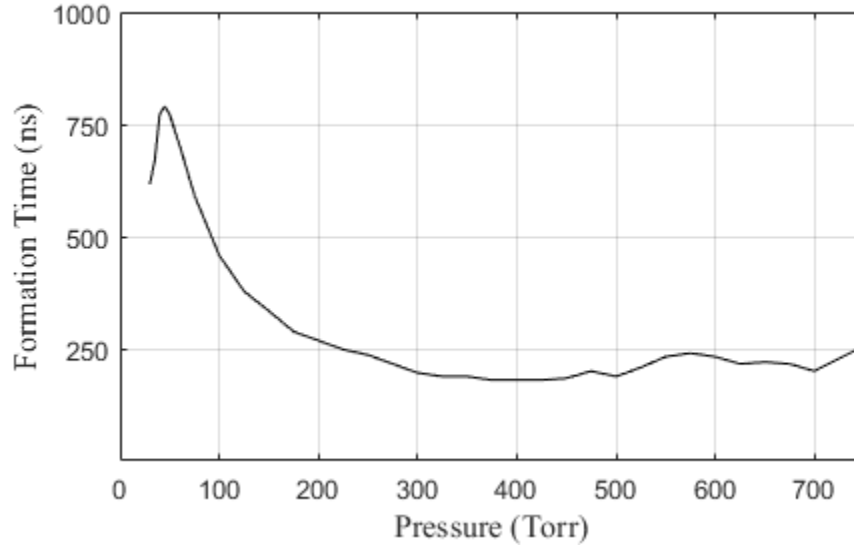
Figure 76 Plasma formation time for the 43 GHz PhC for argon gas pressures for a 2 W input and for gas pressures of 30 to 750 Torr.

6.3.3   Electron Density Measurements

Using transmission data shown in Figure 73, photographs of steady state plasma operation as shown in Figure 77, and the method outlined in section 5.4, the average electron density for the 43 GHz PhC device can be calculated and is shown in Figure 78. At 30 Torr, the average electron density is calculated to be on the order 10^{18} m^{-3} and rapidly increases with pressure until it begins to saturate at 200 Torr to a value of $\sim 10^{20}$ m^{-3}. At pressures greater than 400 Torr, the calculations show a factor of ten increase in density, however, these calculations are based on the transmission coefficient data from Figure 73 and discussed in section 6.3.1. It is suspected that additional factors besides the electron density of the plasma are

affecting the transmission coefficient, and as such, the calculated electron density

values in this pressure region are of low confidence.
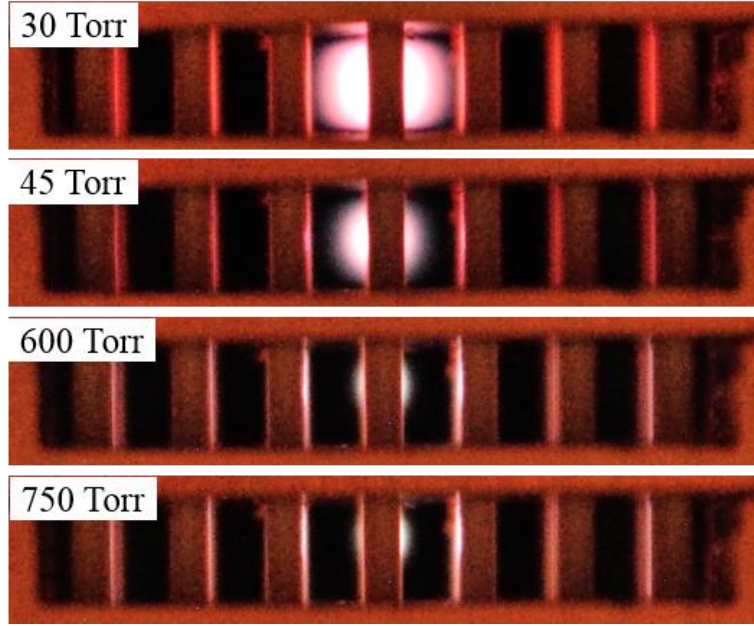
Figure 77 Photographs of steady-state plasma within the central cavity of the PhC at 30, 45, 600, and 750 Torr of argon using an input power of 1.5 W at the resonant frequency.
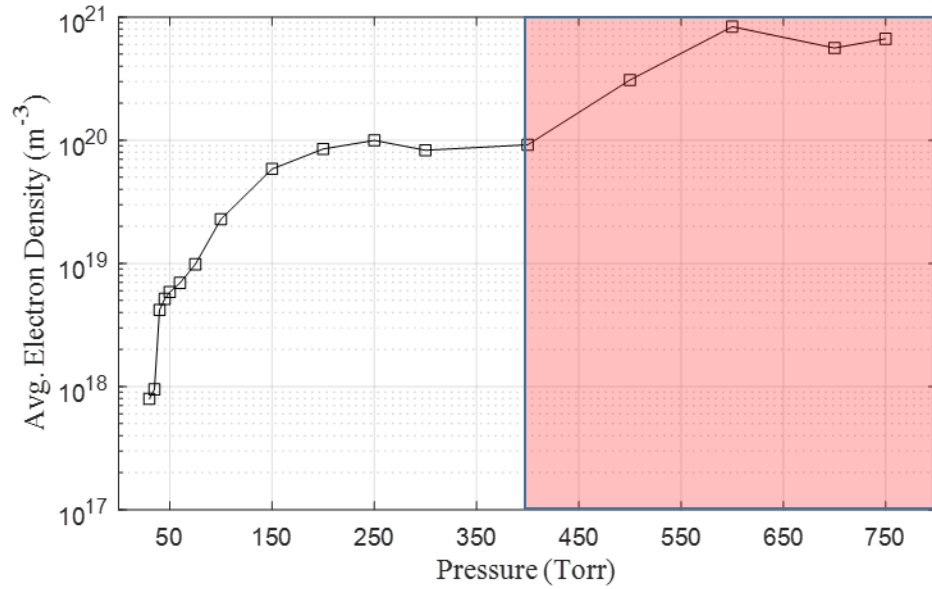
Figure 78 Average electron density (n_e) for pressure between 30 and 750 Torr of argon and input power of 1.5 Watts. Red shaded area indicates values with low confidence.

6.4   Summary

The experimental results of the 43 GHz device show a stark increase in the electron density and plasma formation time as compared to the 8.5 GHz case. There are two main differences between the two devices that could cause this difference in performance. First, the increased frequency of the 43 GHz device plays a role in the electron density, however, experiments and modeling of argon microplasmas created by split ring resonators suggest that at frequencies greater than 4 GHz this effect is minimal [98]. A more significant effect comes from the decrease in cavity height at 43 GHz. The smaller height leads to an increase in the electric field prior to plasma formation. This increase in electric field increases the acceleration of electrons, speeding up the avalanche process and decreasing the plasma formation time. Additionally, the smaller volume of the plasma due to the decreased cavity height gives a higher power density within the plasma, increasing the electron density as compared to the larger cavity of the 8.5 GHz device.

7   Discussion and Conclusion

Integrated plasma elements within photonic crystals have been recently been investigated as a means to control the propagation properties. To date, this research has been focused on plasma elements that require external power sources, such as DC discharge tubes. For the first time, this work has demonstrated a reconfigurable photonic crystal device that self-initiates a plasma element in direct response to the incoming wave. After ignition, the plasma element modifies the transmission properties of the device by redirecting energy away from the output. In their current configuration, the devices shown here respond as power limiters. However, many other photonic crystal configurations exist and should be explored.

Both devices shown here (8.5 GHz and 43 GHz) are of similar design, only differing by size (related to frequency) and input method, coaxial E-probe for the 8.5 GHz device and waveguide for the 43 GHz device. Both devices can self-initiate a plasma at the relatively low input power of 1.0 to 1.5 Watts. However, due to the much smaller cavity height of the 43 GHz device, a greater electric field generated within the central cavity. The reduced cavity height also allows for greater power density within the plasma for the same amount of input power. This leads to a greater electron density for the same gas pressure and input power. For instance, the 8.5 GHz device at 50 Torr and 1 W of input power has an average electron density of $n_e \approx 2 \cdot 10^{16}\ m^{-3}$, the 43 GHz device for the same power and pressure has an average electron density of $n_e \approx 4 \cdot 10^{18}\ m^{-3}$, a 200-fold increase. The increased power density of the 43 GHz device also allows the device to be operated at up to atmospheric pressure. Higher operating pressures allow for increased

127

electron density. Average electron densities for the 43 GHz device reach 10^{20} m^{-3} and higher for argon gas pressures of 250 Torr and greater.

The transmission properties of the photonic crystal are directly impacted by the electron density of the plasma within the cavity. For an input power of 1 Watt, the 8.5 GHz device lowers transmission of the incoming wave by ~ 10 dB (at both 10 and 50 Torr), with most of the power being reflected back towards the source. In contrast, the 43 GHz device lowers transmission by ~ 20 dB at the same power and pressure. This is a direct result of the increased electron density of the 43 GHz device. Transmission is also reduced for increased input powers. At 8.5 GHz, the transmission is further reduced by up to 20 dB for an input power of 6 W. This was not able to be tested at 43 GHz due to the lack of available amplifier power, however a similar result is expected.

Another important aspect of plasma performance is the formation time of the plasma. At 8.5 GHz, and ~ 2 Watts of input power, formation times vary from as low as 200 *ns* at 5 Torr up to 3.5 *μs* at 40 Torr. However, these times are decreased significantly with increasing power, down to as low as 100 ns at 5 Torr and 1.5 *μs* at 40 Torr for a 9 Watt input. Formation times at 43 GHz for a 1.5 Watt input range from 750 *ns* at 45 Torr to as low as 200 *ns* at 400 Torr. Again, additional power levels could not be examined due to available amplifier power at 43 GHz.

Research into reconfigurable photonic crystals using plasma elements is in its infancy. The work presented here is a good first step to understanding what self-initiated plasmas have to offer in this area of research. However, additional work

needs to be completed before a future role can be understood. Specifically, direct electron density measurements, via stark broadening, should be performed to verify that the estimation performed comparing transmission measurements to simulations are accurate. However, due to the placement of the dielectric rods, there is no clear view of the plasma for spectrographic measurements. To get a clear view of the plasma, a view port can be placed on the top of the device. A copper mesh will need to be placed within the viewport as not to alter the electromagnetic fields within the cavity. A depiction of this configuration can be seen in Figure 79. These measurements will go a long way to not only verifying the validity of the method presented in Section 5.4, but also in gaining further understanding of the high-pressure transmission measurements conducted at 43 GHz.
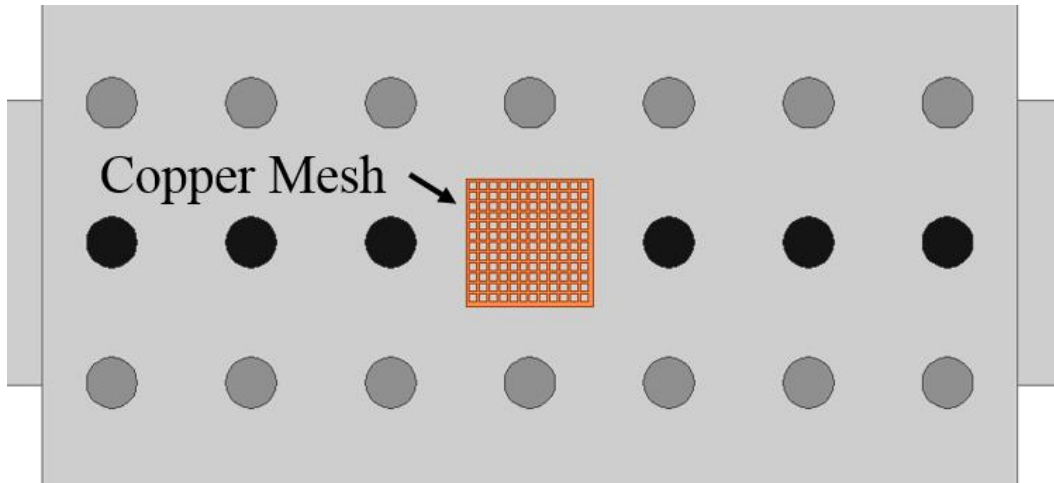
Figure 79 Top view of the PhC device showing placement of plasma viewport with copper mesh.

Of additional interest for future work is in higher frequency devices. Higher frequency experiments are desired to gain understanding of the role that frequency and cavity height play in the plasma parameters. With ever increasing interest in

129

devices in the terahertz regime, integrated plasma elements with photonic crystals

could help to make major advancements in this area.

8 References

[1]   J. Kitagawa, M. Kodama, S. Koya, Y. Nishifuji, D. Armand and Y. Kadoya, "THz wave propagation in two-dimensional metallic photonic crystal with mechanically tunable photonic-bands," *Optics Express,* vol. 20, no. 16, p. 17271, 30 7 2012.

[2]   H. Chong and R. DeLaRue, "Tuning of Photonic Crystal Waveguide Microcavity by Thermooptic Effect," *IEEE Photonics Technology Letters,* vol. 16, no. 6, pp. 1528-1530, 6 2004.

[3]   D. Yang, H. Tian and Y. Ji, "Nanoscale photonic crystal sensor arrays on monolithic substrates using side-coupled resonant cavity arrays," *Optics Express,* vol. 19, no. 21, p. 20023, 10 10 2011.

[4]   B. Wang and M. A. Cappelli, "A tunable microwave plasma photonic crystal filter," *Applied Physics Letters,* vol. 107, no. 17, 2015.

[5]   B. Wang and M. A. Cappelli, "A plasma photonic crystal bandgap device," *Applied Physics Letters,* vol. 108, no. 16, p. 161101, 2016.

[6]   B. Wang and M. A. Cappelli, "Waveguiding and bending modes in a plasma photonic crystal bandgap device," *AIP Advances,* vol. 6, no. 6, 2016.

[7]   J. Lo, J. Sokoloff, T. Callegari and J. P. Boeuf, "Reconfigurable electromagnetic band gap device using plasma as a localized tunable defect," *Applied Physics Letters,* vol. 96, no. 25, p. 251501, 2010.

[8]   O. Sakai, T. Sakaguchi and K. Tachibana, "Verification of a plasma photonic crystal for microwaves of millimeter wavelength range using two-dimensional array of columnar microplasmas," *Applied Physics Letters,* vol. 87, no. 24, p. 241505, 12 12 2005.

[9]   O. Sakai, T. Sakaguchi, Y. Ito and K. Tachibana, "Interaction and control of millimetre-waves with microplasma arrays," *Plasma Physics and Controlled Fusion,* vol. 47, no. 12B, pp. B617-B627, 1 12 2005.

[10]   T. Sakaguchi, O. Sakai and K. Tachibana, "Photonic bands in two-dimensional microplasma arrays. II. Band gaps observed in

millimeter and subterahertz ranges," *Journal of Applied Physics,* vol. 101, no. 7, 2007.

[11]   J. Gregório, S. Parsons and J. Hopwood, "Reconfigurable photonic crystal using self-initiated gas breakdown," *Plasma Sources Science and Technology,* vol. 26, no. 2, 2017.

[12]   J. D. Joannopoulos, S. G. Johnson, J. N. Winn and R. D. Meade, Photonic crystals: molding the flow of light, Princeton university press, 2011.

[13]   E. Yablonovitch, "Inhibited Spontaneous Emission in Solid-State Physics and Electronics," *Phys. Rev. Lett.,* vol. 58, no. 20, pp. 2059-2062, 5 1987.

[14]   S. John, "Strong localization of photons in certain disordered dielectric superlattices," *Phys. Rev. Lett.,* vol. 58, no. 23, pp. 2486-2489, 6 1987.

[15]   C. M. Soukoulis, "The history and a review of the modelling and fabrication of photonic crystals," *Nanotechnology,* vol. 13, no. 3, p. 335, 1 6 2002.

[16]   S. Assefa, G. S. Petrich, L. A. Kolodziejski, M. K. Mondol and H. I. Smith, "Fabrication of photonic crystal waveguides composed of a square lattice of dielectric rods," *Journal of Vacuum Science & Technology B: Microelectronics and Nanometer Structures,* vol. 22, no. 6, p. 3363, 2004.

[17]   K. Ho, C. Chan, C. Soukoulis, R. Biswas and M. Sigalas, "Photonic band gaps in three dimensions: New layer-by-layer periodic structures," *Solid State Communications,* vol. 89, no. 5, pp. 413-416, 2 1994.

[18]   D. A. Grishina, C. A. M. Harteveld, L. A. Woldering and W. L. Vos, "Method for making a single-step etch mask for 3D monolithic nanostructures," *Nanotechnology,* vol. 26, no. 50, p. 505302, 18 12 2015.

[19]   T. Tajiri, S. Takahashi, Y. Ota, J. Tatebayashi, S. Iwamoto and Y. Arakawa, "Demonstration of a three-dimensional photonic crystal nanocavity in a ⟨110⟩-layered diamond structure," *Applied Physics Letters,* vol. 107, no. 7, p. 071102, 17 8 2015.

[20]	S. Iwamoto, S. Takahashi, T. Tajiri and Y. Arakawa, "Semiconductor Three-Dimensional Photonic Crystals with Novel Layer-by-Layer Structures," *Photonics,* vol. 3, no. 2, p. 34, 20 5 2016.

[21]	E. Yablonovitch, T. J. Gmitter and K. M. Leung, "Photonic band structure: The face-centered-cubic case employing nonspherical atoms," *Physical Review Letters,* vol. 67, no. 17, pp. 2295-2298, 1991.

[22]	A. Chelnokov, K. Wang, S. Rowson, P. Garoche and J.-M. Lourtioz, "Near-infrared Yablonovite-like photonic crystals by focused-ion-beam etching of macroporous silicon," *Applied Physics Letters,* vol. 77, no. 19, pp. 2943-2945, 6 11 2000.

[23]	C. Cuisin, A. Chelnokov, D. Decanini, D. Peyrade, Y. Chen and J. Lourtioz, "Sub-micrometre dielectric and metallic yablonovite structures fabricated from resist templates," *Optical and Quantum Electronics,* vol. 34, no. 1/3, pp. 13-26, 2002.

[24]	G. J. Schneider, E. D. Wetzel, J. A. Murakowski and D. W. Prather, "Fabrication of three-dimensional Yablonovite photonic crystals by multiple-exposure UV interference lithography," 2005.

[25]	I. I. Shishkin, K. B. Samusev, M. V. Rybin, M. F. Limonov, Y. S. Kivshar', A. Gaidukeviciute, R. V. Kiyan and B. N. Chichkov, "Inverted yablonovite fabricated by the direct laser writing method and its photonic structure," *JETP Letters,* vol. 95, no. 9, pp. 457-461, 14 7 2012.

[26]	I. I. Shishkin, K. B. Samusev, M. V. Rybin, M. F. Limonov, Y. S. Kivshar, A. Gaidukeviciute, R. V. Kiyan and B. N. Chichkov, "Inverted Yablonovite-like 3D photonic crystals fabricated by laser nanolithography," 2012.

[27]	Z. Hayran, H. Kurt and K. Staliunas, "Light localization in chirped woodpile photonic crystals," *International Conference on Transparent Optical Networks,* Vols. 2016-Augus, pp. 13-15, 2016.

[28]	C. Marichy, N. Muller, L. S. Froufe-Pérez and F. Scheffold, "High-quality photonic crystals with a nearly complete band gap obtained by direct inversion of woodpile templates with titanium dioxide," *Nature Publishing Group,* no. February, pp. 1-8, 2015.

[29]	J. G. Fleming and S.-Y. Lin, "Three-dimensional photonic crystal with a stop band from 1.35 to 1.95 µm," *Optics Letters,* vol. 24, no. 1, p. 49, 1999.

[30]   S. Noda, K. Tomoda, N. Yamamoto and A. Chutinan, "Full Three-Dimensional Photonic Bandgap Crystals at Near-Infrared Wavelengths," *Science,* vol. 289, no. 5479, 2000.

[31]   A. Blanco and C. Lopez, "Silicon Onion-Layer Nanostructures Arranged in Three Dimensions," *Advanced Materials,* vol. 18, no. 12, pp. 1593-1597, 19 6 2006.

[32]   A. Blanco, H. Miguez, F. Meseguer, C. Lopez, F. Lopez-Tejeira and J. Sanchez-Dehesa, "Photonic band gap properties of CdS-in-opal systems," *Applied Physics Letters,* vol. 78, no. 21, pp. 3181-3183, 21 5 2001.

[33]   A. Blanco, P. D. Garcia, D. Golmayo, B. H. Juarez and C. Lopez, "Opals for Photonic Band-Gap Applications," *IEEE Journal of Selected Topics in Quantum Electronics,* vol. 12, no. 6, pp. 1143-1150, 11 2006.

[34]   S. John, A. Blanco, E. Chomski, S. Grabtchak, M. Ibisate, S. W. Leonard, C. Lopez, F. Meseguer, H. Miguez, J. P. Mondia, G. A. Ozin, O. Toader and H. M. van Driel, "Large-scale synthesis of a silicon photonic crystal with a complete three-dimensional bandgap near 1.5 micrometres," *Nature,* vol. 405, no. 6785, pp. 437-440, 25 5 2000.

[35]   M. Qi, E. Lidorikis, P. T. Rakich, S. G. Johnson, J. D. Joannopoulos, E. P. Ippen and H. I. Smith, "A three-dimensional optical photonic crystal with designed point defects," *Nature,* vol. 429, no. 6991, pp. 538-542, 3 6 2004.

[36]   S. V. Kesapragada, P. Victor, O. Nalamasu, D. Gall, E. Schubert and R. Welser, "Nanospring Pressure Sensors Grown by Glancing Angle Deposition," *Nano Letters,* vol. 6, no. 4, pp. 854-857, 21 4 2006.

[37]   N. Liu, H. Guo, L. Fu, S. Kaiser, H. Schweizer and H. Giessen, "Three-dimensional photonic metamaterials at optical frequencies," *Nature Materials,* vol. 7, no. 1, pp. 31-37, 2 1 2008.

[38]   J. Bravo-Abad, J. D. Joannopoulos and M. Soljačić, "Enabling single-mode behavior over large areas with photonic Dirac cones.," *Proceedings of the National Academy of Sciences of the United States of America,* vol. 109, no. 25, pp. 9761-5, 19 6 2012.

[39]   B. Q. Lv, H. M. Weng, B. B. Fu, X. P. Wang, H. Miao, J. Ma, P. Richard, X. C. Huang, L. X. Zhao, G. F. Chen, Z. Fang, X. Dai, T.

Qian and H. Ding, "Experimental discovery of Weyl semimetal TaAs," 16 2 2015.

[40]   C.-C. Cheng and A. Scherer, "Fabrication of photonic band-gap crystals," *Journal of Vacuum Science & Technology B: Microelectronics and Nanometer Structures Processing, Measurement, and Phenomena,* vol. 13, no. 6, pp. 2696-2700, 1995.

[41]   C. C. Cheng, A. Scherer, R.-C. Tyan, Y. Fainman, G. Witzgall and E. Yablonovitch, "New fabrication techniques for high quality photonic crystals," *Journal of Vacuum Science & Technology B: Microelectronics and Nanometer Structures Processing, Measurement, and Phenomena,* vol. 15, no. 6, pp. 2764-2767, 1997.

[42]   a. J. Turberfield, "Fabrication of photonic crystals for the visible spectrum by holographic lithography," *Nature,* vol. 404, no. March, pp. 53-56, 2000.

[43]   G. von Freymann, V. Kitaev, B. V. Lotsch and G. A. Ozin, "Bottom-up assembly of photonic crystals," *Chem. Soc. Rev.,* vol. 42, no. 7, pp. 2528-2554, 2013.

[44]   D. Jackson John, *Classical electrodynamics,* John Wiley & Sons, Inc., New York, NY,, 1999.

[45]   D. J. Griffiths, *Introduction to electrodynamics,* AAPT, 2005.

[46]   R. Shankar, Principles of quantum mechanics, Springer Science & Business Media, 2012.

[47]   R. L. Liboff, Introductory quantum mechanics, Addison-Wesley, 2003.

[48]   J. J. Sakurai and J. J. Napolitano, Modern quantum mechanics, Pearson Higher Ed, 2014.

[49]   J. D. Joannopoulos, P. R. Villeneuve and S. Fan, "Photonic crystals: putting a new twist on light," *Nature,* vol. 386, no. 6621, pp. 143-149, 13 3 1997.

[50]   L. Brillouin, Wave propagation in periodic structures: electric filters and crystal lattices, Courier Corporation, 2003.

[51]   F. Bloch, "Über die Quantenmechanik der Electronen in Kristallgittern," *Zeitschrift für Physik A Hadrons and Nuclei,* vol. 52, no. 7, pp. 555-600, 1929.

[52]   C. Kittel and W. Zachariasen, Introduction to Solid State Physics, Wiley, New York, 1996.

[53]   S. Fan, J. D. Joannopoulos, J. N. Winn, A. Devenyi, J. C. Chen and R. D. Meade, "Guided and defect modes in periodic dielectric waveguides," *Journal of the Optical Society of America B,* vol. 12, no. 7, p. 1267, 1 7 1995.

[54]   R. K. Hoffmann, Handbook of Microwave Integrated Circuits, vol. 1, 1987, p. 527.

[55]   E. Hecht and A. Zajac, "Optics addison-wesley," *Reading, Mass,* vol. 19872, pp. 350-351, 1974.

[56]   A. Casas Bedoya, P. Domachuk, C. Grillet, C. Monat, E. C. M?gi, E. Li and B. J. Eggleton, "Photonic crystal waveguide created by selective infiltration," 2012.

[57]   M. Charlton, M. Zoorob, G. Parker, M. Netti, J. Baumberg, S. Cox and H. Kemhadjian, "Experimental investigation of photonic crystal waveguide devices and line-defect waveguide bends," *Materials Science and Engineering: B,* vol. 74, no. 1-3, pp. 17-24, 5 2000.

[58]   R. Biswas, C. Christensen, J. Muehlmeier, G. Tuttle and K.-M. Ho, "Waveguide circuits in three-dimensional photonic crystals," *Photonics and Nanostructures - Fundamentals and Applications,* vol. 6, no. 2, pp. 134-141, 11 2008.

[59]   H. SAMI SÖZÜER and H. DUYGU ŞENGÜN, "PHOTONIC CRYSTAL ASSISTED 90° WAVEGUIDE BEND," *International Journal of Modern Physics B,* vol. 25, no. 16, pp. 2167-2182, 30 6 2011.

[60]   Q. Chen and D. W. Allsopp, "One-dimensional coupled cavities photonic crystal filters with tapered Bragg mirrors," *Optics Communications,* vol. 281, no. 23, pp. 5771-5774, 12 2008.

[61]   Y. Lu, H. Liu, Q. Sun, N. Huang and Z. Wang, "Terahertz narrow-band filter based on rectangle photonic crystal," *Journal of Modern Optics,* vol. 63, no. 3, pp. 224-230, 4 2 2016.

[62]   P. B. Deotare, L. C. Kogos, I. Bulu and M. Loncar, "Photonic Crystal Nanobeam Cavities for Tunable Filter and Router Applications," *IEEE Journal of Selected Topics in Quantum Electronics,* vol. 19, no. 2, pp. 3600210-3600210, 3 2013.

[63]   W.-Y. Chiu, T.-W. Huang, Y.-H. Wu, Y.-J. Chan, C.-H. Hou, H. T. Chien and C.-C. Chen, "A photonic crystal ring resonator formed by SOI nano-rods.," *Optics express,* 2007.

[64]   S. Olyaee and A. Mohebzadeh-Bahabady, "Designing a novel photonic crystal nano-ring resonator for biosensor application," *Optical and Quantum Electronics,* vol. 47, no. 7, pp. 1881-1888, 1 7 2015.

[65]   Z. Qiang, R. Soref and W. Zhou, "Photonic Crystal Ring Resonators: Characteristics and Applications," *Journal of Nanoscience and Nanotechnology,* vol. 10, no. 3, pp. 1495-1507, 1 3 2010.

[66]   F.-l. Hsiao and C. Lee, "Computational Study of Photonic Crystals Nano-Ring Resonator for Biochemical Sensing," *IEEE Sensors Journal,* vol. 10, no. 7, pp. 1185-1191, 7 2010.

[67]   Y. Zhang, X. Qiu, C. Zeng, D. Li, G. Gao, Y. Wang, J. Yu and J. Xia, "Slow-Light Dispersion in One-Dimensional Photonic Crystal Racetrack Ring Resonator," *IEEE Photonics Technology Letters,* vol. 27, no. 10, pp. 1120-1123, 15 5 2015.

[68]   Y. Xu, C. Caer, D. Gao, E. Cassan and X. Zhang, *High efficiency asymmetric directional coupler for slow light slot photonic crystal waveguides,* 2014.

[69]   E. Cassan and A. Lupu, "Compact and Highly Spectral Selective Asymmetric Co-Directional Coupler Using Slow Light Photonic Crystal Waveguide," *IEEE Photonics Technology Letters,* vol. 24, no. 13, pp. 1121-1123, 7 2012.

[70]   C.-Y. Liu, "Efficient omnidirectional couplers achieved by anisotropic photonic crystal waveguides," *Physics Letters A,* vol. 373, no. 34, pp. 3061-3066, 8 2009.

[71]   J. Zimmermann, M. Kamp, A. Forchel and R. März, "Photonic crystal waveguide directional couplers as wavelength selective optical filters," *Optics Communications,* vol. 230, no. 4-6, pp. 387-392, 2 2004.

[72]   H. Saini, "Photonic crystal based rat race coupler for optical applications," *Optik - International Journal for Light and Electron Optics,* vol. 124, no. 17, pp. 3146-3148, 9 2013.

[73]   C.-Y. Liu, "Fabrication and optical characteristics of silicon-based two-dimensional wavelength division multiplexing splitter with

photonic crystal directional waveguide couplers," *Physics Letters A,* vol. 375, no. 28-29, pp. 2754-2758, 7 2011.

[74]   S. Parsons, J. Gregório and J. Hopwood, "Microwave plasma formation within a 2D photonic crystal," *Plasma Sources Science and Technology,* vol. 26, no. 5, p. 55002, 2017.

[75]   W. Park and J.-B. Lee, "Mechanically tunable photonic crystal structure," *Applied Physics Letters,* vol. 85, no. 21, pp. 4845-4847, 22 11 2004.

[76]   T. D. Drysdale, I. S. Gregory, C. Baker, E. H. Linfield, W. R. Tribe and D. R. S. Cumming, "Transmittance of a tunable filter at terahertz frequencies," *Applied Physics Letters,* vol. 85, no. 22, pp. 5173-5175, 29 11 2004.

[77]   K. Yoshino, Y. Shimoda, Y. Kawagishi, K. Nakayama and M. Ozaki, "Temperature tuning of the stop band in transmission spectra of liquid-crystal infiltrated synthetic opal as tunable photonic crystal," *Applied Physics Letters,* vol. 75, no. 7, pp. 932-934, 1999.

[78]   S. W. Leonard, J. P. Mondia, H. M. van Driel, O. Toader, S. John, K. Busch, A. Birner, U. G?sele and V. Lehmann, "Tunable two-dimensional photonic crystals using liquid crystal infiltration," *Physical Review B,* vol. 61, no. 4, pp. R2389-R2392, 15 1 2000.

[79]   W. S. Fegadolli, N. Pavarelli, P. O'Brien, S. Njoroge, V. R. Almeida and A. Scherer, "Thermally controllable silicon photonic crystal nanobeam cavity without surface cladding for sensing applications," *ACS Photonics,* vol. 2, no. 4, pp. 470-474, 2015.

[80]   Y. Fang, S. Y. Leo, Y. Ni, L. Yu, P. Qi, B. Wang, V. Basile, C. Taylor and P. Jiang, "Optically Bistable Macroporous Photonic Crystals Enabled by Thermoresponsive Shape Memory Polymers," *Advanced Optical Materials,* vol. 3, no. 11, pp. 1509-1516, 2015.

[81]   D. Erickson, T. Rockwood, T. Emery, A. Scherer and D. Psaltis, "Nanofluidic tuning of photonic crystal circuits," *Optics Letters,* vol. 31, no. 1, p. 59, 1 1 2006.

[82]   R. C. Fletcher, "Impulse Breakdown in the 10-9-Sec. Range of Air at Atmospheric Pressure," *Physical Review,* vol. 76, no. 10, pp. 1501-1511, 1942.

[83]   L. G. Christophorou and L. A. Pinnaduwage, "Basic Physics of Gaseous Dielectrics," *IEEE Transactions on Electrical Insulation,* vol. 25, no. 1, pp. 55-74, 1990.

[84]   P. Drude, "Zur Elektronentheorie der Metalle," *Annalen der Physik,* vol. 306, no. 3, pp. 566-613, 1900.

[85]   D. M. Pozar, Microwave Engineering, 1997.

[86]   J. Gregório, A. R. Hoskinson and J. Hopwood, "Modeling of microplasmas from GHz to THz," *Journal of Applied Physics,* vol. 118, no. 8, 2015.

[87]   H. HOJO and A. MASE, "Dispersion Relation of Electromagnetic Waves in One-Dimensional Plasma Photonic Crystals," *Journal of Plasma and Fusion Research,* vol. 80, no. 2, pp. 89-90, 2004.

[88]   H. HOJO, N. UCHIDA, K. HATTORI and A. MASE, "Beaming of Millimeter Waves from Plasma Photonic Crystal Waveguides," *Plasma and Fusion Research,* vol. 1, pp. 021-021, 2006.

[89]   S. Varault, B. Gabard, J. Sokoloff and S. Bolioli, "Plasma-based localized defect for switchable coupling applications," *Applied Physics Letters,* vol. 98, no. 13, p. 134103, 28 3 2011.

[90]   S. Johnson and J. Joannopoulos, "Block-iterative frequency-domain methods for Maxwell's equations in a planewave basis," *Optics Express,* vol. 8, no. 3, p. 173, 29 1 2001.

[91]   J. Gregório, S. Parsons and J. Hopwood, "Microwave harmonic generation and nonlinearity in microplasmas," *Plasma Sources Science and Technology,* vol. 25, no. 3, p. 035018, 2016.

[92]   A. Semnani, S. Macheret and D. Peroulis, "Plasma-Based Tunable High Frequency Power Limiter," *Bulletin of the American Physical Society,* 2016.

[93]   A. M. Cook, J. S. Hummelt, M. A. Shapiro and R. J. Temkin, "Measurements of electron avalanche formation time in W-band microwave air breakdown," *Physics of Plasmas (1994-present),* vol. 18, no. 8, p. 80707, 2011.

[94]   M. A. Lieberman and A. J. Lichtenberg, "Plasma Density Measurement by Cavity Perturbation in High Density Plasma," *Physics of Fluids,* vol. 12, pp. 2109-2116, 1969.

[95]   H. R. Griem, A. C. Kolb and K. Y. Shen, "Stark broadening of hydrogen lines in a plasma," *Physical Review,* vol. 116, no. 1, p. 4, 1959.

[96]   O. B. Minayeva and J. Hopwood, "Langmuir probe diagnostics of a microfabricated inductively coupled plasma on a chip," *Journal of applied physics,* vol. 94, no. 5, pp. 2821-2828, 2003.

[97]   M. Rycroft, Gas discharge physics, vol. 55, Springer Berlin, 1993, p. 1487.

[98]   A. R. Hoskinson, J. Gregório, S. Parsons and J. Hopwood, "Electron confinement and heating in microwave-sustained argon microplasmas," *Journal of Applied Physics,* vol. 117, no. 16, 2015.